Light Harvesting in Fiber Array Organic Solar Cells

Marina Mariano Juste

Supervised by Prof. Jordi Martorell

Al meu avi

Agraïments

Durant aquests últims anys he tingut la sort de poder dedicar-me a la recerca, i aquesta està sent una de les experiències més gratificants tant a nivell personal com a nivell professional.

Per aquest motiu estaré sempre agraïda amb l'oportunitat que em va oferir, ja fa set anys, el Prof. Jordi Martorell per poder fer unes estades d'estiu en el seu grup de recerca aquí a l'ICFO. Des de que vaig tenir el primer contacte amb el grup el 2007, he conegut moltes persones que han vingut i marxat. De totes elles sempre he intentat aprendre el màxim. Des d'aquell juliol del 2007, la primera persona que recordo va ser el meu supervisor en Philip, i també la gent del grup com en Sergio, en Marc, en Xavi (el físic), l'Albert i en Luis. Després vaig marxar per acabar la meva llicenciatura i col·laborar amb el departament d'Òptica de la universitat, on vaig conèixer el Jordi Andilla, qui em va ensenyar a escriure una bona llibreta de laboratori i no una acumulació de gargots intel·ligibles. Mes tard, vaig tornar a l'ICFO per fer el master i començar el doctorat en el grup d'en Jordi Martorell, que aleshores es deia NPC (Nanophotonic Crystals) però després va a passar a ser ONP (Organic Nanostructured Photovoltaics).

Llavors vaig retrobar a les persones que havia conegut feia un parell d'estius i en vaig conèixer de noves, com en Roberto Macovez que em va supervisar la tesi del master. D'en Roberto admiraré sempre la seva gran capacitat d'escriure articles. Per aquella època van començar a fer el doctorat amb mi, en Rafa i la Can, dues persones que recordo amb gran estima.

En aquests agraïments no podrien faltar els meus dos companys de despaxt, en Marc Maymó i en Xavi Elias. Sou molt grans!!! M'ha encantat compartir cadascun dels moments que hem passat junts. Vosaltres m'heu ensenyat molt, tant de la recerca com de la vida i es clar, m'heu ajudat a perfeccionar el meu castellà. Teniu guanyat un raconet dins del meu cor; sempre hi sereu. El temps passa, el Marc va marxar i va venir la Paola, una gran noia també. He gaudit treballant colze amb colze amb ella i també passant grans moments fora de la oficina. Moltes gràcies per ser com ets Pao!

Pel grup han passat un munt de persones que no oblidaré mai, com la Luat, el Francisco, el David, la Camila i l'Alberto (gràcies pels teus consells a l'hora del cafè). I els que encara segueixen en ell com en Quan, la Silvia, el Pablo, l'Elias i el Miguel (he disfrutat amb cascuna de les discussions científiques que hem tingut davant la pissarra). També vull recordar tota la gent amb qui he tingut el plaer de col·laborar, com el Prof. Gregory de Brusel·les i el Prof. Kim i el seu estudiant Guillermo de la UPC. Han sigut set anys, Marc, Mario, Pelayo, Luis M., Armand, Alberto, Naeimeh, Fede, Parisa, Mónica... A tots els ICFOnians amb qui he compartit moments, gràcies.

No només tinc paraules d'agraïment pels científics, aquí a l'ICFO també he tingut el suport d'un munt de persones de direcció. Començant pel Xavi Menino i el seu equip del taller mecànic, que sense la seva ajuda gran part de la recerca aquí a l'ICFO no seria possible. Passant pels tècnics de la sala blanca, el Luis Enrique i el Javi Perez a qui admiro per la seva gran responsabilitat. Al Santi i la Magda de compres, que fan les coses fàcils. A la Mª José, la Mónica i la Merçè per la seva paciència que un cop per setmana (com a mínim) havien de fer-me la targeta per entrar. A les supernoies de recursos humans, la Manuela, la Cristina, la Meri i la Laia, heu d'ensenyar al món com fer bona burocràcia, sou super eficients.

Per acabar no em puc oblidar de donar les gràcies als meus amics, tant els de la uni com els de Terrassa. En especial a l'Anna, una gran científica i millor persona, de la que he après cada dia i segueixo aprenent. A la meva família agraeixo que estiguin sempre al meu costat, tant en els bons moments com en els dolents; a la meva tieta Glòria i la pizza-peli dels dissabtes, al meu pare Miquel i a la meva mare Dolors per fer-me tal com soc, i a la meva parella, en Néstor, per abraçar-me quan ho he necessitat. A tots vosaltres us estaré eternament agraïda per acompanyar-me en aquest viatge, gaudint sempre de la vostra companyia.

Abstract

Considering that the most abundant renewable energy source is the Sun, photovoltaic technology possesses one of the highest potentials to provide environmental benign and sustainable energy worldwide. Currently, most of commercial available modules are fabricated from crystalline silicon because of its high efficiency. To lower fabrication costs and increase the functionality of the solar modules, several thin film technologies are under development. Among them, organic photovoltaics has created large expectations provided it possesses some intrinsic advantages, such as lightweight, flexibility or semi-transparency.

However, the low charge mobility in the majority of the organic semiconductor materials prevents the use of active layers thicker than a few hundred nanometers. This leads to a limited light harvesting capacity and, consequently, a limited conversion efficiency. Different optical approaches have been considered to enhance the absorption of organic solar cells and increase their efficiency. In this thesis, we propose a novel configuration based on the use of fiber arrays to effectively trap light and efficiently couple it into the active layer to enhance absorption.

The thesis work is presented in five chapters. After an introductory chapter, in chapter 2 light absorption of an organic solar cell deposited on the

backside of a fiber array is studied theoretically. A strong enhancement in light harvesting is predicted using such configuration. For small diameter fibers the enhancements originated from light coupling to some low quality whispering gallery modes, while for large diameter fibers light seemed to be effectively trapped inside the fiber structure.

In chapter 3 and 4, we consider the dip-coating procedure, a fabrication technique that can be applied to deposit from a precursor solution, layers on a substrate irrespective of its shape. Its viability is demonstrated by applying it to different device architectures. The deposition on such non-flat substrates of the rest of the layers forming an organic solar cell is also examined. For instance, several relevant changes that had to be introduced to the ITO sputtering to obtain transparent electrodes with an optimal quality, both, optically and electrically, are discussed.

Once the layer deposition is optimized to fulfill the electrical and optical requirements of organic solar cells, in chapter 5, we experimentally demonstrate that an enhanced light absorption can be achieved from such organic solar cells when deposited on fiber arrays. Optical fibers of 80 μm in diameter were used to fabricate the arrays to be used as the cell substrate. Such substrates were coated with an organic solar cell of evaporated small molecules. The implemented fiber array configuration is seen to be an effective light trapping method. Indeed, the photogenerated current from such devices is shown to increase by a 26%, which is a considerable percentage when compared to the majority of the optical approaches that were considered in the past to enhance absorption in organic cells.

Resum

Si considerem que la font d'energia renovable més a abundant és el Sol, la tecnologia fotovoltaica posseeix un dels potencials més alts per poder produir l'energia mundial de forma sostenible i benigne amb el medi ambient. Actualment la majoria dels mòduls comercials estan fabricats de silici cristal·lí ja que aquest material té una gran eficiència. Per tal de rebaixar els costos de producció i incrementar la funcionalitat d'aquest panells solars, diverses tecnologies de capa prima s'estan desenvolupant. Entre elles, la tecnologia fotovoltaica amb materials orgànics ha creat grans expectatives gràcies a les seves propietats intrínseques, com per exemple la seva lleugeresa, flexibilitat o bé semi transparència.

Per altra banda, la baixa mobilitat de les càrregues en la majoria dels semiconductors orgànics impedeix l'ús de capes actives no molt més gruixudes que uns pocs nanòmetres. Això provoca que tinguin una capacitat de col·lecció lumínica limitada i com a conseqüència, la eficiència de conversió energètica també ho és. S'han considerat diferents estratègies òptiques per tal de millorar l'absorció en les cel·les solars orgàniques i incrementar la seva eficiència. En aquesta tesi proposem una configuració innovadora basada en l'ús d'una matriu de fibres, les quals atrapen i acoblen la llum en la capa activa per millorar l'absorció d'aquesta.

La present tesi consta de cinc capítols. Després d'un capítol introductori, en el capítol 2 s'estudia teòricament l'absorció de llum d'una cel·la solar orgànica dipositada en la part posterior de la matriu de fibres. Per diàmetres de fibra

petits, les millores són degudes a l'acoblament d'uns modes recirculants de llum de baixa qualitat. Mentre que per diàmetres grans, la llum sembla estar atrapada de forma efectiva dins de l'estructura formada per les fibres.

En els capítols 3 i 4 hem considerat el recobriment per immersió, aquesta tècnica de fabricació pot ser aplicada per dipositar capes des d'una solució precursora a un substrat, independentment de la seva forma. La validesa de la tècnica es demostra quan s'aplica a diferents arquitectures de cel·la. El dipòsit en aquestes estructures no planes de la resta de les capes que formen la cel·la solar orgànica també s'ha investigat. Per exemple, es discuteixen varis canvis rellevants, els quals s'han tingut que introduir per la polvorització catòdica del ITO, per tal d'obtenir elèctrodes transparents amb unes qualitats òptiques i elèctriques òptimes.

Un cop el dipòsit de les diferents capes s'ha optimitzat per complir els requeriments òptics i elèctrics de les cel·les solars orgàniques, en el capítol 5 demostrem experimentalment que una millora de l'absorció de la llum es pot aconseguir en les cel·les solars orgàniques quan estan dipositades en la matriu de fibres. S'han utilitzat fibres òptiques de 80 μm de diàmetre per fabricar la matriu, la qual servirà de substrat de la cel·la. La configuració de matriu de fibres implementada s'ha comprovat que és un mètode efectiu per atrapar la llum. De fet, la corrent fotogenerada per aquest dispositiu s'incrementa un 26%, aquest és un percentatge considerable quan es compara amb la majoria d'estratègies òptiques explorades en el passat per augmentar l'absorció en cel·les solars orgàniques.

Academic Production

JOURNAL ARTICLES

- *Light coupling into the whispering gallery modes of a fiber array solar cell for mechanically fixed sun tracking.* M. Mariano, F.J. Rodríguez, P. Romero-Gomez, G. Kozyreff and J. Martorell, **Sci. Rep.** (2014) 4,4959.

- *Enhanced stability in semi-transparent PTB7/PC71BM photovoltaic cells* P. Romero-Gomez, R. Betancur, A. Martinez-Otero, X. Elias, M. Mariano and J. Martorell. Submitted.

- *Fabrication of transparent organic photovoltaic modules by laser ablation.* M. Mariano, P. Mantilla, A. Martínez-Otero, D. C. Urbanek and J. Martorell. In progress.

- *Molecular conformation in organic films from quantum chemistry ab initio calculations and second harmonic spectroscopy.* R. Macovez, N. Lopez, M. Mariano, M. Maymo and J. Martorell, **J. Phys. Chem. C** (2012), 116, 26784.

- *Large Optical-Frequency Shift of Molecular Radiation via Coherent Coupling to an Off-Resonance Plasmon.* R. Macovez, M. Mariano. S. Finizio, G. Kozyreff and J. Martorell, **Phys. Rev. Lett.** (2011) 107, 073902.

- *Measurement of the dispersion of air and of refractive index anomalies by wavelength-dependent nonlinear interferometry.* R. Macovez, M. Mariano. S. Finizio and J. Martorell**. Opt. Express** (2009)17, 13881.

BOOK CHAPTER

- *One-dimensional photonc crystals for light management in organic solar cells* M. Mariano, P. Mantilla-Perez, P. Romero-Gómez, A. Martínez-Otero, X. Elias, R. Betancur and J. Martorell. Ed. Springer 2014

PATENTS

- J. Martorell, M. Mariano, P. Romero-Gómez. US Patent Application 14/157,138

Table of Contents

1 | Introduction

A change in the global climate is becoming more apparent as the increase in the global temperature, the change in precipitation, the decrease in the artic ice, or changes in snowing patterns have established records in recent years. Since 1910 the average global surface temperature recordings show a clear upward trend, very different than the pattern of averaged registered temperatures from the preindustrial period (cf. Figure 1.1).
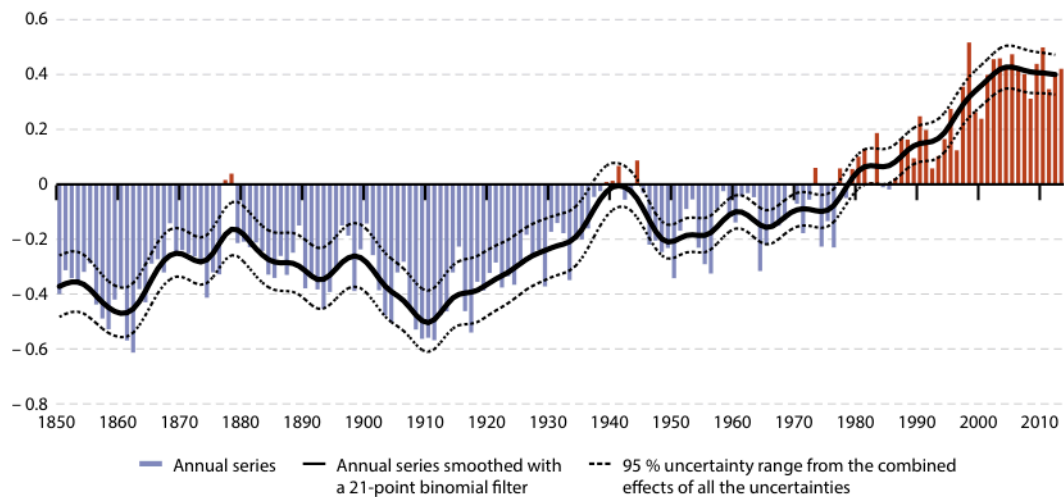

Figure 1.1. Temperature deviations in ⁰C compared to 1961-1990 average[1].

The impact of the climate change may be quite different in different regions of the world. For instance, in southern Europe problems of water availability arise as more frequent droughts occur, whereas in northern Europe a larger exposure to coastal and river floods seem to happen more often[2]. To

positively contribute in the slowing down of such warming process, the European Commission has set a list of three major objectives to be accomplished within the Europe 2020 horizon strategy: a 20 % reduction of green house emissions relative to the emissions from 1990, increasing up to 20% the share of renewable energy in the total energy consumption, and move towards a 20% increase in energy efficiency[1].

On the other hand, the Intergovernmental Panel on Climate Change Organization has shown that most of the global green house emissions are dominated by energy production[3]. In fact, as shown in Figure 1.2, close to 78.3% of the global energy consumption comes from fossil fuels. The most pollutant of fossil fuels is coal, and its demand has increased lately in the developing countries. Since the supply of coal is not as limited as oil, an increase of its share in the energy production pie seems inevitable. The goal of a carbon-free economy to brake this circle may be reachable if the percentage of renewable energies used is increased. This may bring for many countries the additional benefit of reducing their dependence on energy imports.
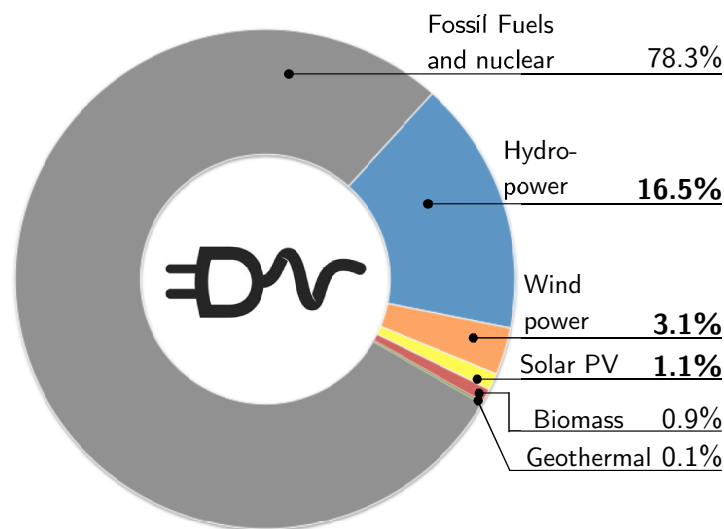
Figure 1.2. Estimated renewable energy share of global final energy consumption of 2012. Source: REN 21[4].

Among all the available renewable energy sources we may single out three major ones: hydropower, wind power, and solar photovoltaics. The former provided 16.5% of the energy consumed on 2012 worldwide. Such source is very reliable and it is one of the most efficient among the renewables. However, one of its major drawbacks is its major environmental impact. Wind power amounts to an energy production of 3.1% globally. This is kind of energy has the advantage of being space-efficient, given that a single turbine can generate enough electricity to feed, for instance, 600 US homes[5]. One of the major drawbacks of this technology is its high dependency on intermittent natural phenomena making energy production quite unpredictable. The latter one, when compared to the other two, is still more costly and less efficient but, on the other hand, solar photovoltaics, is the cleanest form of energy production, has a very low or negligible environmental impact, while it relies on an unlimited source of energy. In fact, if we compare the renewable energy potential of each of the currently available sources, depicted in Figure 1.3, we observe that the solar photovoltaic technology is

the one that possesses the highest. Considering the amount of solar energy that reaches the Earth surface, it is possible to meet existing global energy needs 10000 times over[6]. By covering just 4% of world's desert areas with photovoltaic installations, the world's total primary energy demand could be met. But, before covering our entire desert areas, there are other zones that have an untapped potential to support solar power generation such as buildings, not only roofs but also façades. If such surfaces were covered with solar panels the European Union's goal of a 20% renewable energy share would be much easier to achieve[6].
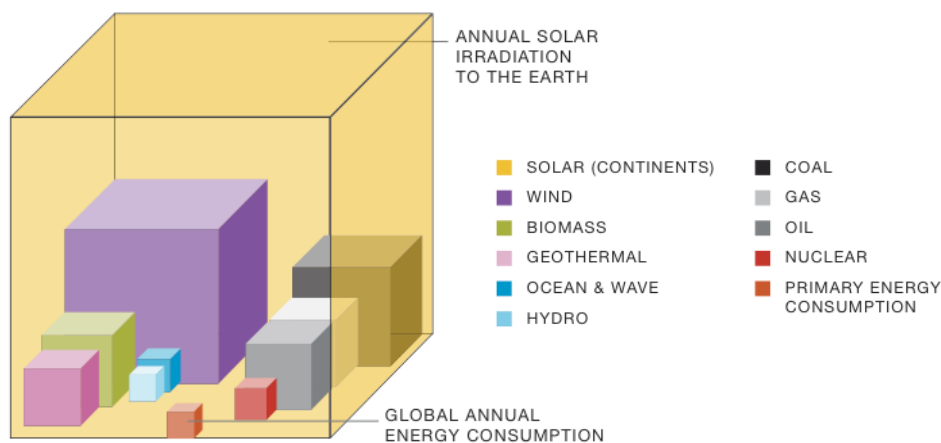
Figure 1.3. Solar irradiation versus established global energy resources. Fossil fuels are expressed with regards to their total reserves and renewable energies to their yearly potential. Source: EPIA[6].

As no other renewable energy source is as abundant as Sunlight, the photovoltaic (PV) technology has emerged as one of the most promising candidates to help meet the current energy demand while supplying clean and sustainable electricity to the world. Since the first invention of the modern

silicon solar cells in 1950, there have been tremendous advances in such field with power conversion efficiencies increasing from 6% to 44%[7]. Although most of the commercially available PV systems are made of crystalline silicon wafers and ribbons, other inorganic semiconductors have been used to develop thin film solar cells in order to reduce the material usage and diminish the manufacturing costs. In spite of the fact that the power conversion efficiency is used as a metric to measure the potential of a technology, in order to have competitive photovoltaic devices, such energy-producing units must be capable of delivering back the energy spent fabricating them in a reasonable time.

Several of the thin film PV technologies being developed may offer a lower fabrication cost provided the amount of material used is dramatically reduced. This is particularly true for the case of the organic solar cell (OSC) technology that is based on an architecture where the thickness of all layers in the cell is sub-micron. Additionally, when compared to their inorganic counterparts, organic electronic materials have lower cost and can be processed at room temperature. The organic PV technology has other advantages, as for instance the intrinsic flexibility of organic compounds, which can be used for a roll-to-roll production. This may increase the manufacturing speed and, eventually, further reduce fabrication costs. Besides a potentially lower cost, organic PV materials can be engineered to tune their electronic and optical properties to fulfill specific applications[8], which are difficult to meet with the standard PV modules. Taking into account that in the last ten years the power conversion efficiency (PCE) of organic PV has increased from 2.5 to 11%, added to a potentially lower production costs and

simpler processing, some statistical studies suggest that organic solar cells could be as competitive as other PV technologies in the coming years[9].

1.1 Working principles of Organic Solar Cells

The photon to charge conversion mechanism in OSC presents some significant differences compared to their inorganic counterparts. There are four fundamental steps involved in such process (cf. Figure 1.4). Firstly, upon the absorption of a photon with higher energy than the optical gap of the active layer, an electron from the highest occupied molecular orbital (HOMO) from the donor undergoes a photoinduced excitation to the lowest unoccupied molecular orbital (LUMO) and forms a coulombically bound electron-hole pair, also called Frenkel exciton. The ratio between the formed excitons to the total incident photons per wavelength is defined as the absorption efficiency (η_A). Secondly, such exciton must diffuse to the interface between the donor and the acceptor to split. As excitons have a binding energy of $0.5 - 2$ eV[10], which is much higher than the thermal energy at room temperature, they need the presence of a second material to split them. Such path should be shorter than 10 nm, which is typically the length excitons can travel before recombining. This length is the so-called diffusion length (L_D). In this step, the efficiency associated is the exciton diffusion efficiency (η_{ED}) and accounts for the amount of excitons that reach the donor-acceptor interface to the excitons generated.

Figure 1.4. Energy levels of an organic solar cell with a scheme of the consecutive steps after the absorption of a photon that leads to collected charges in the electrodes. Donor and acceptor materials, which are sandwiched between the anode and the cathode, form the active layer. The electron blocking layer (EBL) and the hole-blocking layer (HBL) are shown, too.

In the third step, those excitons that arrive at the donor-acceptor interface undergo a charge transfer process at an ultrafast pace[11], which results in separated electrons in the LUMO level of the acceptor and holes in the HOMO level of the donor. The efficiency of such process relates the amount of excitons that dissociate with the ones that arrive at the donor-acceptor interface and it is called efficiency in charge separation (η_{CS}). Once the exciton has been split up, the free charges are then transported to the electrodes through a drift field for its extraction[12]. The efficiency of this last step is called efficiency of charge collection (η_{CC}) and accounts for the number of carriers that arrive at both the cathode and anode considering the split excitons.

Thus, the ratio of collected photogenerated charges at the electrodes to the number of incident photons at a particular wavelength, called external quantum efficiency (EQE), can be written as:

$$EQE(\lambda) = \eta_A(\lambda)\eta_{ED}\eta_{CS}\eta_{CC} \tag{1.1}$$

The amount of collected charges in the electrodes is directly proportional of such efficiency described in Eq. 1.1 and the amount of photons that strike the solar cell, i.e., the photon flux (cf. Figure 1.5). Then the short circuit current density (J_{sc}) is defined as,

$$J_{sc} = q \int EQE(\lambda)\Phi(\lambda)\frac{\lambda}{hc}d\lambda \tag{1.2}$$

where q the charge of the electron, $\Phi(\lambda)$ corresponds to the standard AM1.5G spectral irradiance of the sun, h is the Plank's constant, c is the velocity of light and λ is the wavelength.
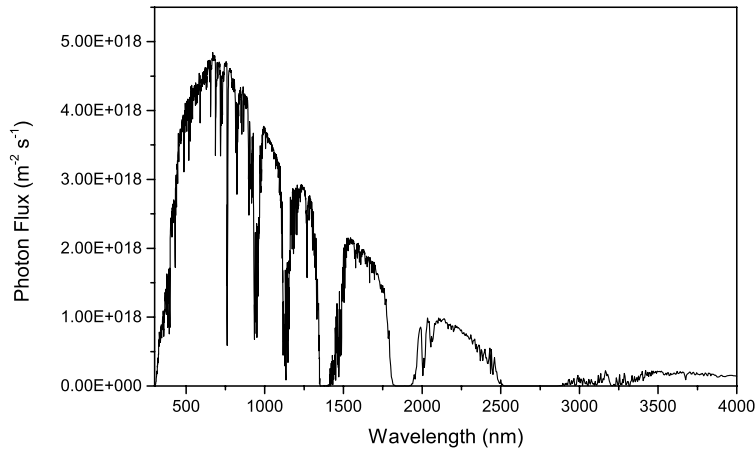
Figure 1.5. Sun photon flux at the surface of the earth corresponding to the standard AM1.5G spectral irradiance.

A widely used equivalent circuit for describing photovoltaic devices is a diode with two parasitic resistances, as shown in Figure 1.6.
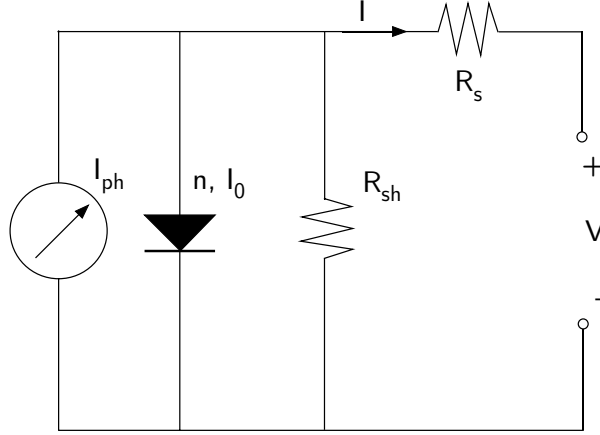
Figure 1.6. One-diode equivalent circuit for solar cells. Such equivalent circuit is composed of two parasitic resistances, a diode and a current source.

And the current obtained in such circuit can be described by the Shockley equation,

$$I - I_0 \left(e^{\left(q \frac{V - IR_s}{n k_B T} \right)} - 1 \right) - \frac{V - IR_s}{R_{sh}} + I_{ph} = 0 \tag{1.3}$$

where I is the current in the circuit, V is the applied external bias, R_s is the serial resistance, R_{sh} is the shunt resistance, n is the ideality factor, k_B is the Boltzmann constant, T is the temperature and I_{ph} is the light induced electrical current.

Such parameters can be extracted from current density vs. voltage curves (JV curves) measured in the devices. A general representation of such curves is shown in Figure 1.7. The J_{sc} is also defined as the current at $V=0$

divided by the effective area of the solar cell. The open circuit voltage (V_{oc}) is the voltage at $I=0$. In OSC such V_{oc} is determined by the difference in the quasi Fermi levels of electrons and holes[13]. Another important parameter that describes the performance in OSC is the so-called Fill Factor (FF) and is defined as,

$$FF(\%) = \frac{P_{max}}{J_{sc}V_{oc}} \cdot 100 \tag{1.4}$$

where P_{max} is the maximum power and correspond to the maximum area of the square in the fourth quadrant (cf. Figure 1.7). Such value may be directly related to the morphology and conductivity of the layers forming the device.

Finally, the power conversion efficiency (PCE) is given by

$$PCE(\%) = \frac{J_{sc}V_{oc}FF}{P_i} \cdot 100 \tag{1.5}$$

where P_i is the incident power of light per unit area, which for AM1.5G illumination corresponds to 100 mW/cm^2 (1 sun).
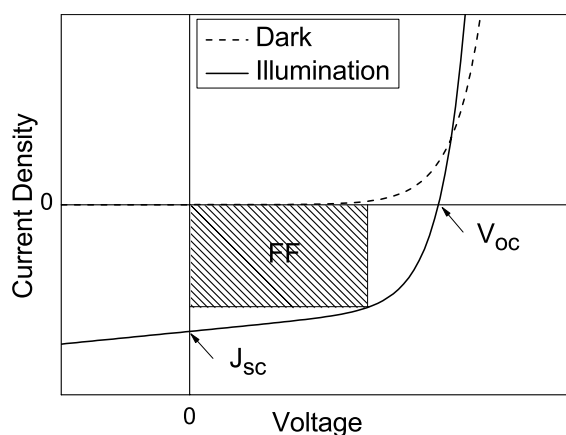
Figure 1.7. Current density vs. voltage curve of an organic solar cell under illumination (solid curve) and dark (dashed). All the photovoltaic parameters for the PCE extraction are represented.

In order to obtain larger PCE in OSC, several relevant developments have been included in the architectures during the past twenty years of research in the field[14]. At the beginning it was thought that for a correct charge extraction two materials, one that donates and another that accepts photogenerated electrons, should be stacked together forming a bilayer structure, shown in Figure 1.8a. But the small interface area, which led to low exciton splitting rate, and the short diffusion length, which prevented the use of thicker layers; both factors were limiting the PCE of such devices. This led to an alternative configuration where donor and acceptor materials are intermixed forming what is known as blend or bulk heterojunction (cf. Figure 1.8b). Since the donor:acceptor blend is macroscopically homogeneous, the contacts have to be selective to extract only one kind of carriers at each side of the active layer. The inclusion of buffer layers between the electrodes and the active layer prevented photogenerated charges from reaching the incorrect

contact. Such layers are known as hole and electron blocking layers, HBL and EBL respectively.

Although such latter configuration enhances the amount of created free charges given that thicker active layers may be used, it has a low efficiency in charge transport collection, thus promoting their recombination. A hybrid bilayer and bulk heterojunction combination has been proposed to take advantage of the previous two configurations[15,16]. As shown in Figure 1.8c, this configuration consists of a mixed donor-acceptor layer sandwiched in between an acceptor and donor layers. All of the above consider a single junction active layer but there are more complex systems, the so-called tandem devices, resulting from using more than one active layer to form double or even triple organic solar cells[17-19].
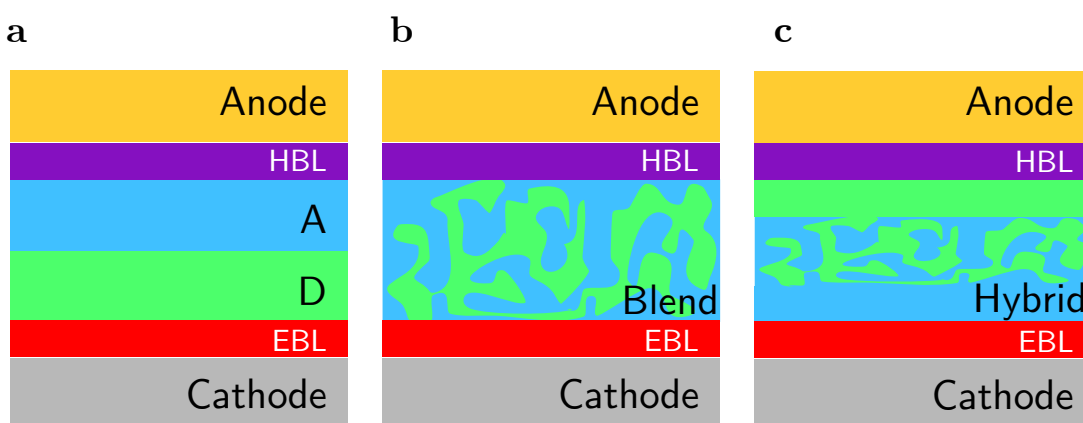
Figure 1.8. Three main architectures of organic solar cells a) Bilayer structure, the active layer is composed of separated donor (D) and acceptor (A) layers. b) Bulk heterojunction, the donor and acceptor are intermixed forming a blend. c) Hybrid bulk heterojunction, having an intermixed zone of blend sandwiched in between separated acceptor and donor layers.

In the majority of such cases the total active layer thickness is close to 100 nm or even less. This makes the active layer of the OSCs a relatively poor light absorber. Such thin layers combined with narrow absorption bands of the active materials lead the field of the OSC towards many different optical designs to enhance light harvesting.

1.2 Optical management of light

As indicated in the previous section the overall thickness of an OSC is about 100 nm. Consequently, it is very important to optimize the thicknesses and position of the absorbing materials to ensure that the electromagnetic field distribution is such that most of the light intensity is concentrated in the active layer. One of the simplest approaches to enhance the absorption in the active layer is replacing the buffer layer in contact with the back reflector for a material with a reduced extinction coefficient. This enhanced the reflectivity of the back electrode which resulted in an increase of the J_{sc}[20].

Light enhancements can be further improved by tuning the thicknesses of the layers to obtain an optimal optical interference. In fact, the relevance in optimizing such optical interferences has been made apparent in studies recently performed on transparent OSC. In such kind of OSC, the back metallic contact is so thin that is no longer a good reflector. As a consequence, part of the light is lost[21]. One-dimensional photonic configurations have been proposed to partially re-harvest such lost photons. Combining the small molecule solar cell with a selective reflectivity near-infrared Bragg reflector,

the PCE of the device was enhanced while permitting a high transmission in the visible range. One-dimensional photonic crystals have also been employed to increase the near-infrared photon harvesting in polymer solar cells[22].

Particularly interesting is the device that combines high performance transparent OSC with a photonic configuration to collect near-ultraviolet and near-infrared photons[23]. Such configuration implemented an ad hoc path for light harvesting and the PCE was recovered to an 80% of its opaque counter part. When optical microcavities were applied in opaque cells, the PCE was enhanced a 20%. Such enhancement was ascribed to the improved photon collection by the resonant microcavity structure[24]. Applying the microcavity design to transparent OSCs, an optimized optical cavity was able to achieve a 90% of the PCE obtained with the opaque cell while maintaining the transparency above 20%[25].

In addition to the 1-D structures, there are other configurations for light trapping that involved texturing in two or three dimensions. When a photonic crystal was embossed in the blend, using an hexagonal array of bulk heterojunctions nanocolumns[26,27] or nanoholes[28], an enhanced photocurrent was observed, providing light scattering by the nanostructure that enhanced light trapping in the device. Such enhancement in the absorption by light scattering is also present if the nanostructure is integrated in one of the buffer layers[29]. Other thin film technologies, such as quantum dot solar cells, applied a light-trapping scheme with a nano-imprinted electrode capable of both diffracting light and collecting the photo-generated carriers[30,31]. Texturing the electrodes was also applied in OSC using a periodic[32] or a random[33] grating.

There, the increase in the photon absorption was by light diffraction when the incident light was reflected back from the back electrode.

Other approaches to increase the effective light path inside the OSC considered the use of plasmonic structures[35]. The presence of metallic nanoparticles in the buffer layer not only increased the degree of light absorption but also enhanced the degree of exciton dissociation[36,37]. Different shapes have been proposed to enhance different parts of the spectra, such as nanocubes[38] or plasmonic oligomers[39]. But the presence of nanostructures is not restricted to the cell buffer layers, they can be also found in the active layer[40] or as a grating in the back electrode[41]. Recent studies showed a plasmonic OSC with a PCE above 8%[42]. This latter configuration used the light scattered by plasmonic nanoparticles to achieve a 20% enhancement in the light absorption.

There are other microstructures with the ability to redirect or even trap light inside the devices. One of the first exploited configurations was the V-shape tandem device with two individual cells combined in a folded geometry[43]. The unabsorbed light from the first cell will be reflected towards and absorbed by the adjacent cell. At small entrance angles, almost all the light can be trapped within the structure and eventually absorbed by the active layers. The extrapolation of such idea of light trapping by multiple reflections but in single cells was applied to a microprism array substrate[44,45]. Other light trapping configurations have been explored with the optical elements separated from the thin film devices, such as a pyramidal rear reflector[46] or an array of microlens[47]. The former induced four passes of light

through the active layer due to the total internal reflection at the original light incidence surface. In the latter, the enhancement was attributed to a combination of two processes. Firstly, a longer optical path length inside the active layer because the curved microlenses surface refracted the incoming light. And secondly, light reflecting off one of the microlens may strike a neighboring one, where the lens curvature results in an incident angle favorable for transmission.

Diminishing the size of such optical elements laid over planar devices down to submicron scale has been explored, too. A configuration of nanospheres on top of a high-index photovoltaic absorber layer from a thin film cell was proposed to couple light into such high-index material and obtain an enhanced light absorption. The authors claimed that the more effective coupling originated from whispering gallery modes (WGM) inside the spheres[48,49]. An alternative approach to improve the absorption using WGM considered a low-quality factor spherical nanoshell structure that facilitated the coupling of light into such resonant modes and substantially enhanced the light path inside the material[50]. Such structures to assess the WGM have been applied experimentally to trap light and enhance the absorption only in silicon thin films[51-53].

1.3 Thesis Outline

In the current thesis we explore the enhancements in the light absorption by an OSC when using non-planar substrates, in particular, fiber arrays. In Chapter 2 we present a theoretical study of such absorption when the OSC is deposited on the backside of such an array of parallel fibers. The model developed indicates that the enhancements in charge collection result from coupling to some low quality WGM for small fiber diameters, and light trapping for larger ones.

To experimentally implement such configuration, a technique suitable for depositing solution-processed layers on any kind of non-planar surface is discussed in Chapter 3. The procedure we consider is the dip-coating technique, which involves substrate immersion in a solution bath containing the material to coat the substrate with. Different OSC architectures are evaluated when using such technique.

When fabricating the entire device, in addition to the dip-coating technique for the active layer, one has to make sure that the deposition of the rest of the different layers forming an OSC is also compatible with particularities of the corrugated substrate used. In Chapter 4 we examine in detail the deposition of an ITO electrode on curve and corrugated surfaces. The aim is to obtain layers with electrical and optical properties very similar to the ones fabricated on standard planar substrates.

In the last chapter, an array of optical fibers of 80 μm in diameter are used for the fabrication of the array and the experimental implementation of

an OSC on a fiber array using small-molecule evaporation as the active layer is presented. In the experimental result reported we show that with this device, large enhancements in light absorption, between 20 and 30% are possible. Such enhancements measured in photogenerated currents were in agreement with the trend predicted by the theory when the fiber diameter is large as discussed in Chapter 2.

2 | Model of Whispering Gallery Mode coupling in organic solar cells

In the current chapter we explore light absorption by the active layer of an organic solar cell in a configuration based on implementing the cell on the backside of an array of parallel silica fibers. We shall see that in such fiber array solar cell (FAOC), when the diameter of the fiber is small, light can be effectively coupled into low quality WG resonant modes for the fibers or be trapped inside the fiber array when the diameter is very large.

We consider coupling at normal incidence but also when the angle for the incident light relative to the normal of the fiber array deviates from such normal incidence up to 90 deg. The light absorption dependence with the diameter of the fibers is considered too. Note that in all the cases studied in this chapter the focus is in the optical enhancement effect provided by the fibers relative to the planar configuration. In accordance the wavelength independent factor to account for losses in the collection of charges relative to the absorbed photons, is taken to be equal to unity everywhere.

2.1 Modeling light absorption by OSC on fiber arrays

To study the performance of the FAOC configuration (cf.Figure 2.1a) we carried out numerical simulations using the finite element method

numerical technique implemented in the commercial software COMSOL Multiphysics®. The electromagnetic wave equations were solved in the two-dimensional area corresponding to the transversal section of a single organic cell fiber, shown in Figure 2.1b. We assumed the fibers to be made of fused silica and in the numerical modeling the optical parameters for such material were used. We consider fiber diameters ranging from 0.5 nm up to 18 μm. In many of the cases considered the layer structure of the cell is simplified to a three layer architecture where the thicknesses for each one of the layers was set to 100 nm, corresponding to the approximate thicknesses for an optimized performance of the equivalent planar cell[54]. For all the layers except for the fused silica one, the refractive indices of all materials in the layers were taken from experimental measurements we performed. For the fused silica the index was taken from the literature. Extremely thin buffer layers that must be included in any experimental realization of the majority of OSC, as explained in Chapter 1, were omitted in our numerical calculations given their negligible effect in the re-distribution of the optical field intensity.

To determine the electromagnetic field distribution, we imposed periodic conditions (Floquet periodicity) on both lateral sides of the single device to simulate the effect of the array. Such periodic boundary conditions are well justified provided the largest fiber diameter considered in this work was 40 times smaller than the transversal coherence of visible sunlight[55]. Multiple absorbing ports were defined in the upper air boundary for each possible diffraction angle of the periodic structure. This avoided non-physical reflections at the upper boundary coming back to the system fiber plus cell. For the same reason, we kept at least one wavelength distance from the upper

boundary to the silica fiber in order to avoid near fields that may not be absorbed by the ports. In-plane (TM) and out-of-plane (TE) polarizations were simulated separately with a power excitation corresponding to one sun. A perfect electric conductor boundary condition was imposed to the lower boundary although its effect may be considered negligible since light is very effectively reflected by the 100 nm back metal contact. For comparison, a planar OSC was also simulated and the same boundary conditions were applied. In the latter case, light was incident from a fused silica glass substrate and the power of the incident wave was corrected by the corresponding Fresnel coefficient for the air-glass refraction.
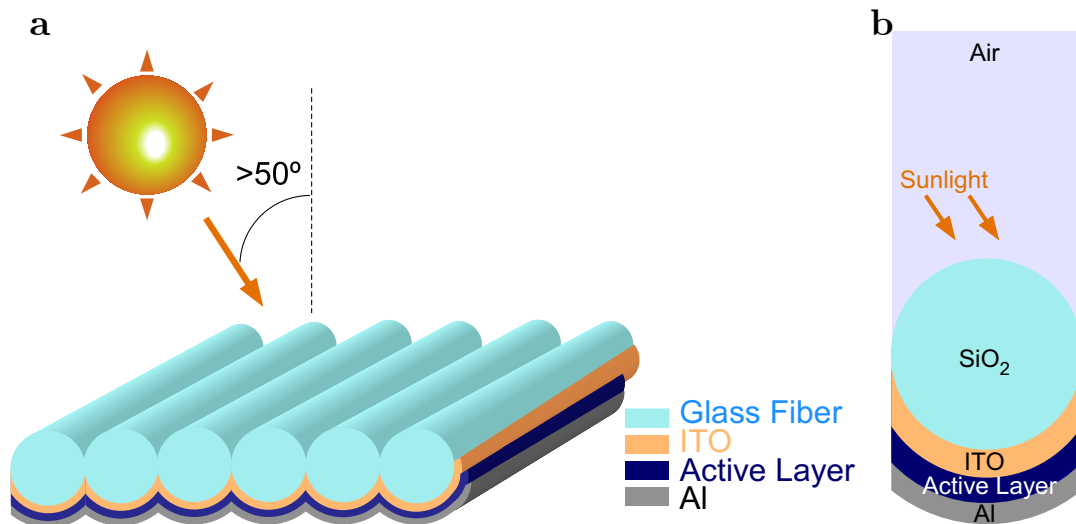

Figure 2.1. Schematic view of the FAOC a) The fiber array is the substrate where the OSC is deposited. The performance of the solar device is studied as a function of the angle of incidence of the Sunlight relative to the normal to the fiber array. b) Enlarged view of the cross section of one silica fiber from the array shown in a).

As shown in Figure 2.1a, where a schematic view of the solar cell device considered is depicted, such device may consist of a number of fibers stuck together forming an array of parallel fibers that serve as the substrate for an OSC device. The different layers of the cell architecture are deposited on the backside of the array relative to the incoming sunlight incident on the front side of the array. A detailed cross section of a single cell fiber from the array is shown in Figure 2.1b. As indicated above for all the numerical studies we present in this chapter, we consider silica as the substrate material.

2.2 EQE and J_{sc} of a FAOC with 1.5 μm diameter fibers

In this section we consider the case when the back side of this substrate is coated with a three layer organic cell composed of a layer of Indium Tin Oxide (ITO) as transparent electrode, an active layer made of a Poly(3-hexylthiophene-2,5-diyl) blended with Indene-C60 Bisadduct (P3HT:ICBA), and an Aluminum (Al) metallic contact. The convolution of the P3HT:ICBA extinction coefficient with the sun photon flux leaves a wavelength window for PV operation ranging from 300 nm to 750 nm. At each wavelength, the total power dissipation over the active layer area is integrated to extract the photon absorption in this layer or, equivalently, the EQE.
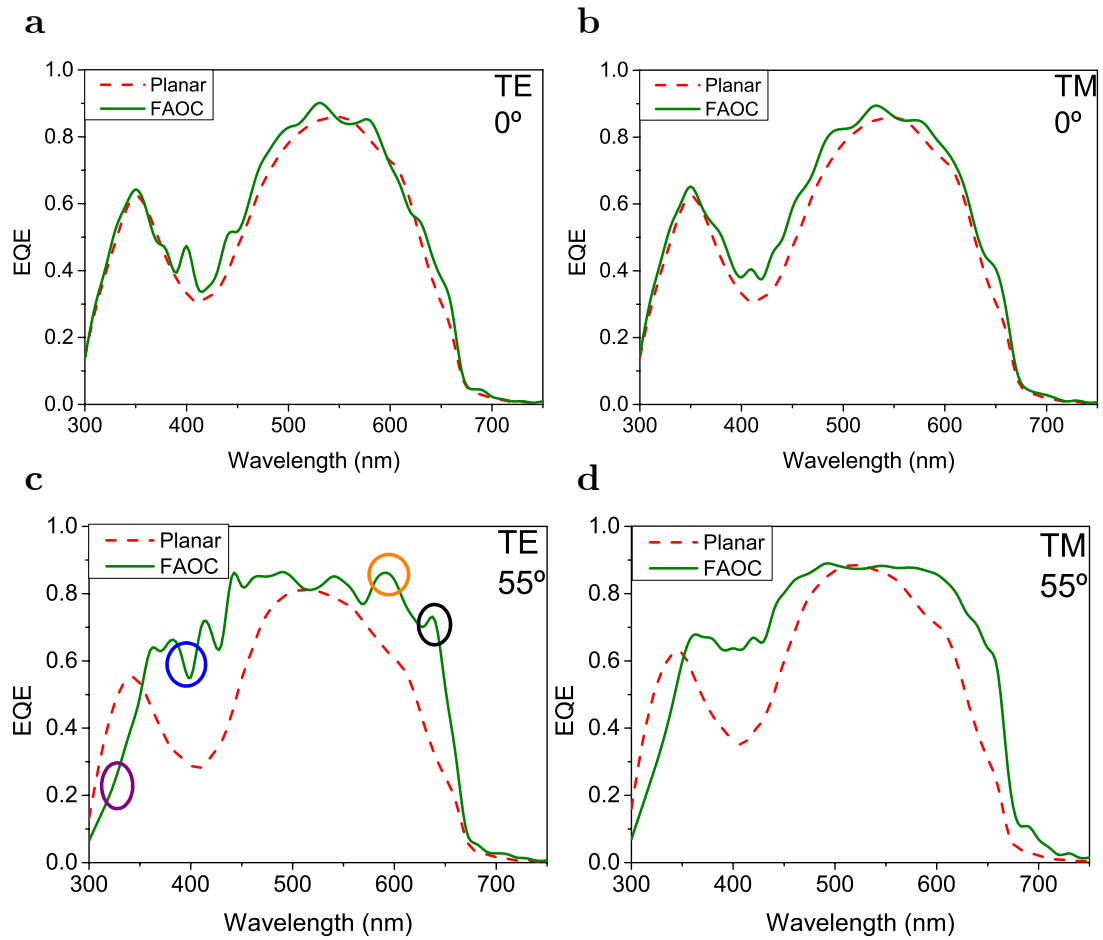
Figure 2.2. External quantum efficiencies of a 1.5 μm diameter fiber FAOC (solid green) and an equivalent planar cell (dashed red). The simulated EQEs are shown at normal incidence (0 deg) for a) TE and b) TM polarizations and at 55 deg for c) TE and d) TM polarizations. Note that at 55 deg incidence the increase in EQE for the fiber array relative to the planar cell is apparent at almost all wavelengths. The TE field intensity distributions at 320 nm (violet circle), 400 nm (blue circle), 600 nm (orange circle), and 640 nm (black circle) are shown in **Figure 2.3**.

The predicted EQEs at normal incidence (0 deg) for the FAOC and planar cells at, both, TE and TM polarizations are shown in Figure 2.2a and 2b, respectively. Although the performance of the FAOC is slightly better

than the planar one, no significantly different features are observed when comparing both EQEs. This is not the case, when the light is incident at 55 deg. In that event, the EQE for the FAOC, shown for the TE and TM polarizations in Figures 2.2c and 2.2d, respectively, is largely improved at almost the entire wavelength range. In the wavelength range spanning from 430 to 600 nm, the EQE is almost saturated to its maximum possible value. The EQE of the planar cell at 400 nm and surrounding wavelengths exhibits very low values reaching a local minimum of 0.25 for the TE polarization and 0.35 for the TM polarization due to the combined effect of a destructive interference and a local minimum of the P3HT:ICBA extinction coefficient (cf. Figure A.2). On the contrary, in the same wavelength region the EQE for the FAOC is always higher than 0.5 for both polarizations.

To better understand what causes the increase in EQE at 55 deg incidence, we numerically computed the spatial electric field norm distribution at 320, 400, 600 and 640 nm, shown in Figure 2.3 for the TE polarization. Such field distribution indicates that for the last three cases photon trapping in the active layer occurs all along the half coated fiber perimeter. Incidence at 55 deg induces a partial excitation of a WGM, which leads to light trapping at the inner boundary of the spherical interface separating the transparent electrode and blend from the metal electrode. The excitation of WGMs is particularly apparent at 640 nm when the extinction coefficient is small. The TE field distribution, shown in Figure 2.3d, exhibits high intensity lobes in a large part of the half perimeter of the cylinder occupied by the ITO

electrode and active layer. Therefore, we may attribute the 2.3 times enhancement observed in the EQE to an increased absorption path for the light within the active layer. At 320 nm coupling to the WGM is aborted by the higher extinction coefficient of ITO at that wavelength. Consequently, as seen in Figure 2.2, no gain in the EQE can be obtained at that wavelength region where absorption is dominated by the ITO extinction coefficient.

a

λ=320nm |E|(V/m)

b

λ=400nm |E|(V/m)

c λ=600nm |E|(V/m)

d λ=640nm |E|(V/m)
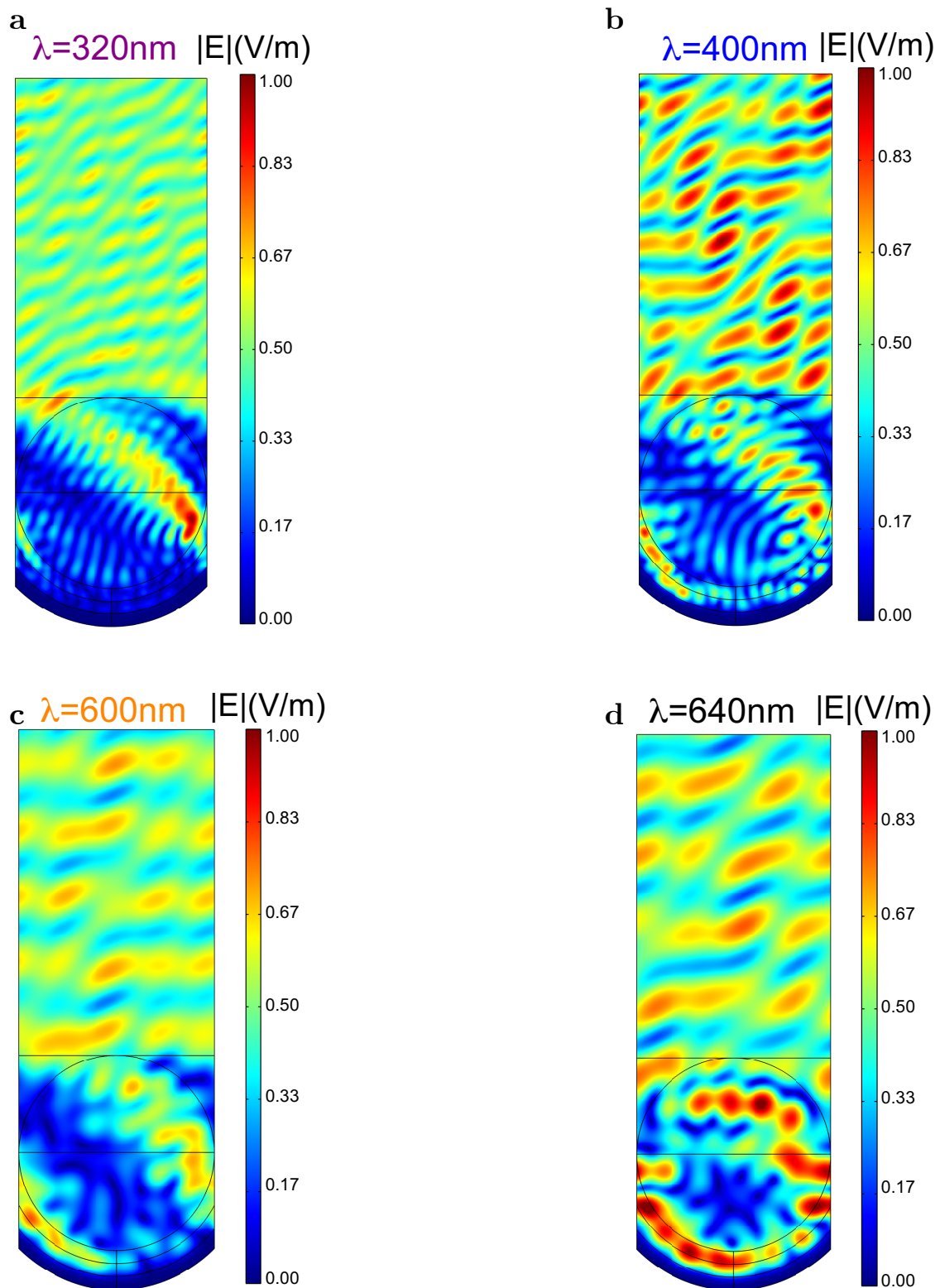
Figure 2.3. Cross section of the spatial distribution TE field norm. Fiber diameter of the FAOC is 1.5 μm, light is incident at 55 deg, and the wavelength tuned at a) 320 nm, b) 400 nm, c) 600 nm and d) 640 nm. All figures are normalized to 1 V/m and the same color coding is used for all of them.

We have also considered the case were the fiber array is finite and limited to a total number of five fibers surrounded by air. In that case the field distribution was computed for fibers of 1.5 μm in diameter surrounded by an air box of 10.5 x 7.5 μm for a light incidence of 55 deg. As shown in Figure 2.4a, for an excitation wavelength of 400nm, similar field distribution lobes as the ones from Figure 2.3b are observed for the inner fibers. In accordance, the EQE of such finite FAOC is similar to the one from the periodic case, as depicted in Figure 2.4b. If we compare the EQE obtained with different air box sizes, we observe that as the box size is reduced the fiber/air box volume ratio increases and consequently the overall EQE resembles more to the periodic FAOC. These results confirm the validity of the periodic boundary conditions applied to model light harvesting in FAOC.

a

b
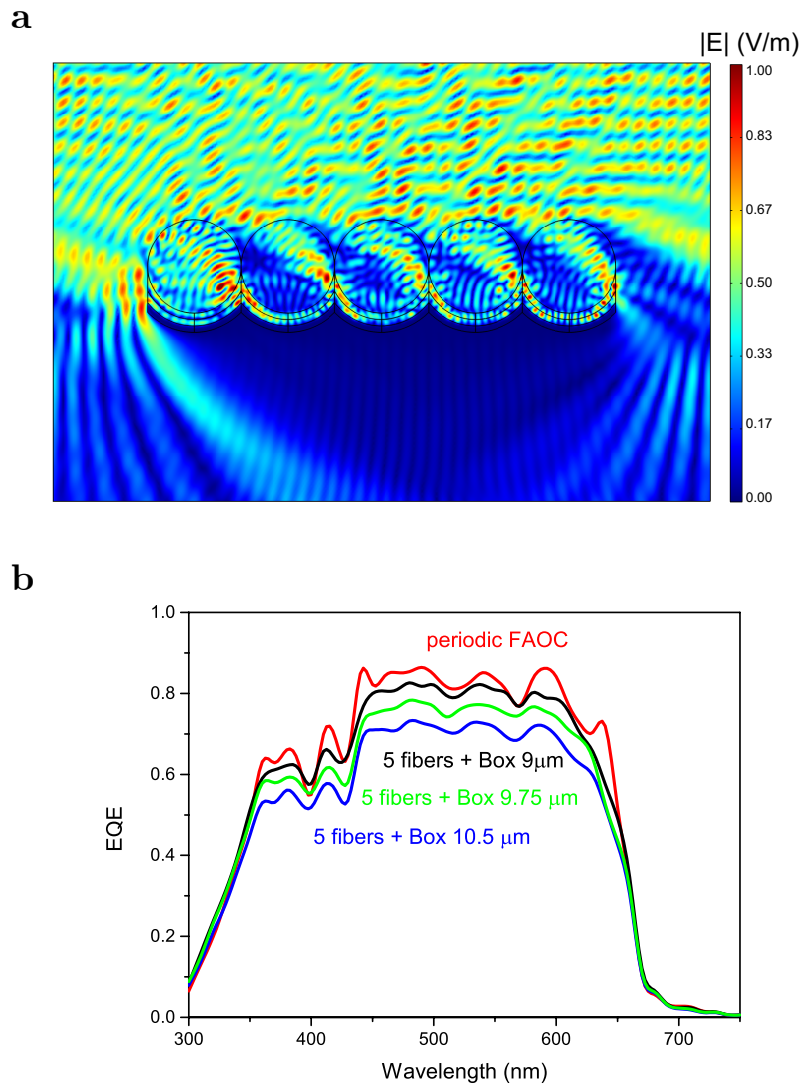
Figure 2.4. Calculations of a finite FAOC composed of 5 fibers surrounded by an air box. a) Electromagnetic field distribution of a finite FAOC containing 5 fibers of 1.5 μm contained in a air box of 10.5 x 7.5 μm, excited with λ =400nm. The lobes of WGMs are observed in the three inner fibers. b) Simulated EQE for three different air box sizes and the EQE of a periodic FAOC (red solid line).

To estimate the short circuit current of the FAOC and compare it to the one from the standard planar OPV, we computed the J_{sc} obtained at each angle of incidence, shown in Figure 2.5a. This current was calculated using

Equation (1.2) from Chapter 1. At normal incidence, the J_{sc} for the FAOC is 6% higher than the planar cell. When the angle of incidence increases the planar cell's J_{sc} stays almost constant up to 40 deg, whereas for the FAOC one increases with angle as the light gets coupled more effectively into the WGM. The J_{sc} exhibits a maximum at 55 deg being 30% larger than the planar. At higher angles, as expected, the J_{sc} for, both, FAOC and planar cells decays rapidly but the one for the FAOC remains always larger.

As the angle of incidence increases, the electrical power generated for both cells would decrease by a $\cos(\theta_i)$ factor accounting for the projected area to a surface normal to the direction of the incident light. As shown in Figure 2.5b, this reduction in electrical power can be partially compensated by the FAOC due to a photocurrent generation that is maximized at 55 deg rather than at normal incidence. For a solar cell placed in a horizontal plane, energy collected from sunrise to sunset would be proportional to two times the area underneath the curves shown in Figure 2.5b. This area is 17% times larger for the FAOC than for the planar case. As shown in Figure 2.5b, the energy collected by the FAOC from 0 to 52 deg would be equivalent to the energy collected by a planar cell maintained, at all times, perpendicular to the sun in that angular range.

a

b
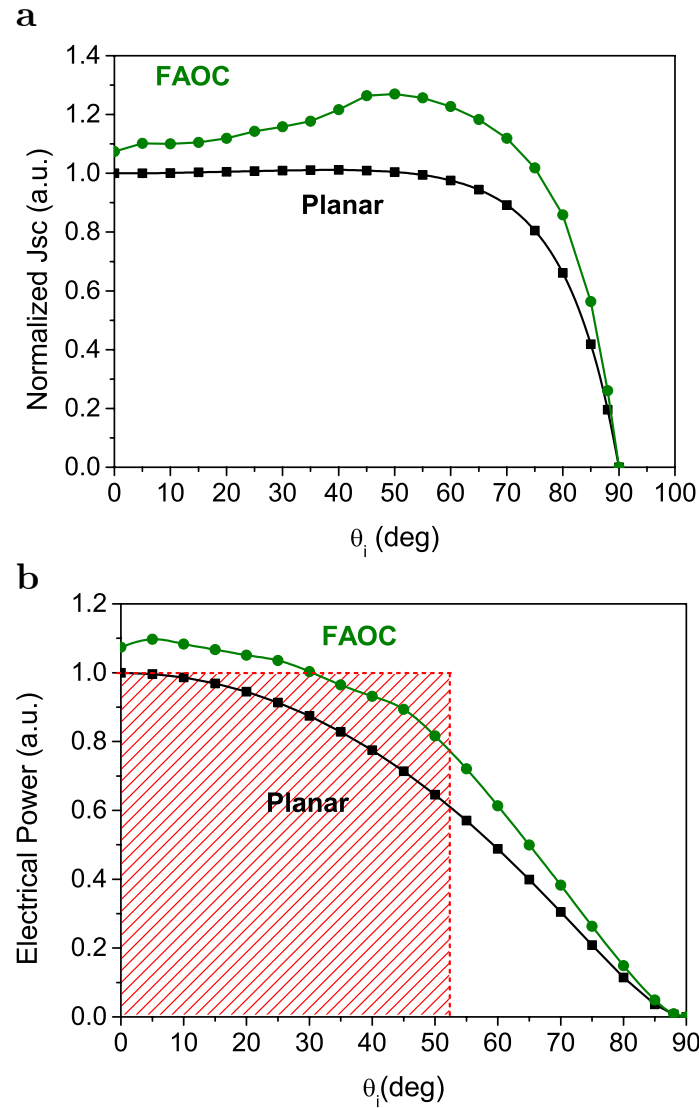
Figure 2.5. Normalized electrical response of FAOC compared to a planar cell. a) Normalized J_{sc} for the planar cell (black squares) and for a 1.5 μm fiber diameter FAOC (green dots) as a function of the sunlight angle of incidence, θ_i. b) Electrical power in arbitrary units as a function of the incidence angle provided by the planar device (black squares) and by the 1.5 μm fiber diameter FAOC (green dots). The area of the red rectangle would be proportional to the energy collected by a planar cell tracking the movement of the sun up to 52 deg. Up to this angle the area under the FAOC curve is the same. Currents and powers are normalized to the response of the planar device at 0 deg. The black and green lines are only a guide for the eye.

We also considered the performance for the FAOC as the separation between adjacent fibers was varied. The J_{sc}, shown in Figure 2.6, varies little as the fiber separation is increased up to 300 nm, while it shows a mildly pronounced drop as adjacent fibers get closer to progressively overlap and eventually causing the final FAOC configuration to resemble a planar device. Such drop in J_{sc} occurs mostly in between -100 and -200 nm.
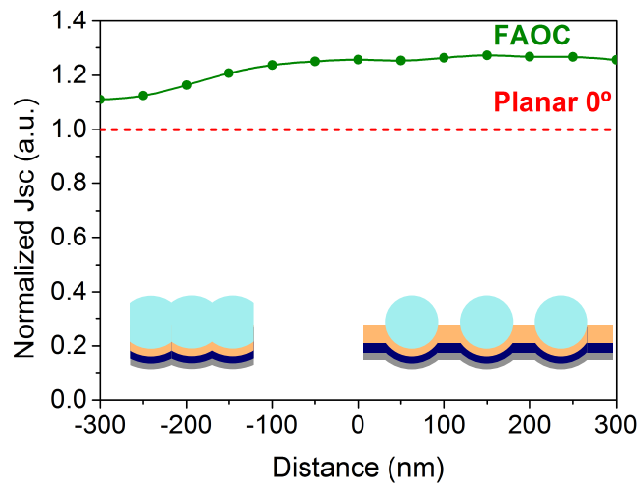
Figure 2.6. Electrical response as a function of fiber separation. Normalized J_{sc} at 55 deg incidence for a 1.5 μm fiber diameter FAOC (green dots) when the separation between two adjacent fibers is varied. A negative separation corresponds to a fiber overlap (left inset), and a positive separation is for the case when adjacent fibers are connected by a planar cell (right inset). The green line is only a guide for the eye.

2.3 Light absorption dependence with fiber diameter

Commercially available fibers, the so-called telecommunication fibers, typically have large diameters when compared to the ones used in the

simulations. Taking into account that regular sizes for such kind of fibers are 125 μm, 80 μm or 50 μm and the wavelength to be coupled in such arrays is between 400nm-700nm, the ratio between fiber size and wavelength would be about 160, whereas for the 1.5 μm this ratio may be slightly larger than 3 at most. Unfortunately, with finite element method numerical technique in COMSOL and a standard computer, one is restricted to study small fiber diameters. A standard desktop computer can not handle the large amount of elements in the mesh needed to study the field distribution when large diameters are considered. In the first part of this section we extend the study of the previous one to consider diameters up to 12 μm. Beyond such diameter the computation capabilities available did not allow us to consider the multiple wavelength studies needed to make predictions for the EQE and J_{sc}. However, it is possible to get a hint on the behavior that one may find at large fiber diameters by numerically computing light absorption at a given small wavelength in order to maximize the fiber size wavelength ratio. In the last part of this section we study cases where the fiber diameter/wavelength ratio approaches 90.

For fiber diameters below 12 μm we studied the J_{sc} dependence with the diameter for light incident at 0, 55 and 60 deg. All the other geometrical parameters in the cell architecture were kept fixed. For normal incidence FAOC systems performed better than the planar ones having a maximum around 1.5 μm. At 55 deg when the diameter is below 500 nm and, light confinement at the perimeter of the fiber close to the back metal contact is ineffective, the J_{sc} for the FAOC is not better than for the planar configuration. As seen in Figure 2.7a, this situation is reversed as the diameter

is increased, and the J_{sc} reaches a maximum at a fiber diameter of 1.75 μm. At such fiber dimensions the EQE, shown in b, is very close to the optimal for a large wavelength interval spanning from 375 to 650 nm. This indicates an optimal coupling to the WGM for such entire wavelength range. As the fiber diameter is increased further, the J_{sc} decreases while the EQE for the FAOC resembles more the one for the planar cell, as shown in Figure 2.7b. This indicates a less effective coupling to the WGM at certain wavelengths when the fiber diameter increases. When the incidence angle is set at 60 deg we observe that the maximum J_{sc}, shown in Figure 2.7a, shifts slightly towards larger fiber diameters. However, the general trend is very similar to the one seen when the angle was set to 55 deg.

a

b
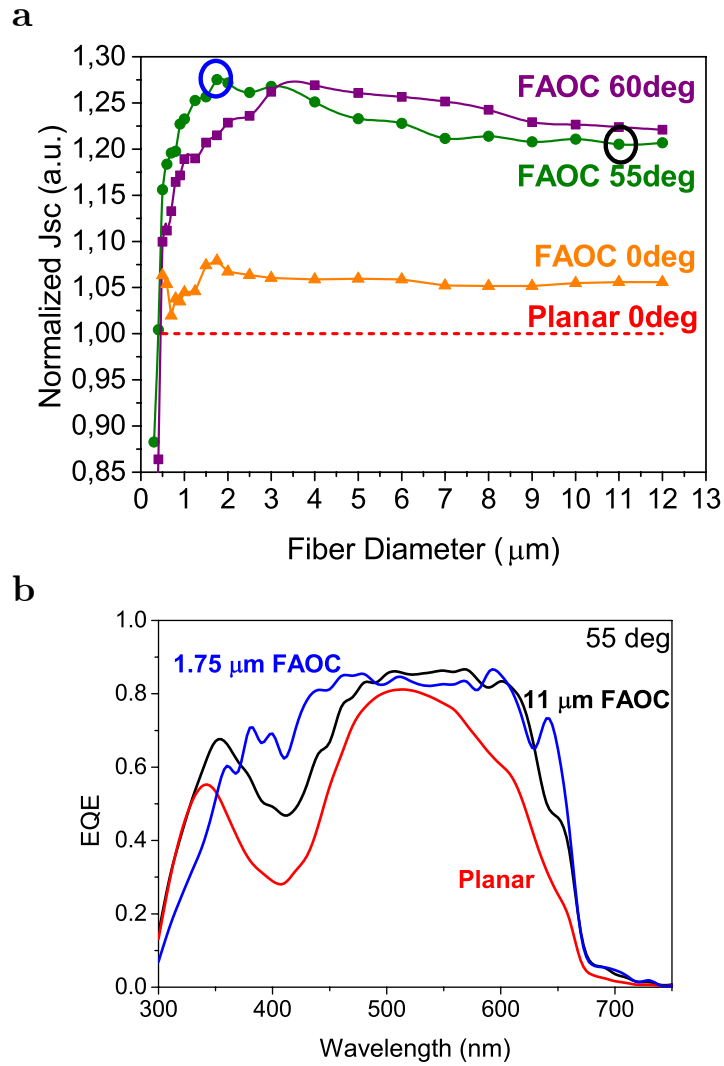
Figure 2.7 Maximum response of the FAOC as function of fiber diameters. a) Normalized J_{sc} at and incidence of 55 deg (circular dots) and 60 deg (square dots) for different fiber diameters of the FAOC. Normalized J_{sc} for the planar cell (red dashed line).. The green and purple lines are only a guide for the eye. The normalization is to the planar cell at 0 deg incidence. b) EQE at an incidence of 55 deg for the FAOC when the fiber diameter is 1.75 μm (blue), when the fiber diameter is 11 μm (black), and for the planar cell (red).

To gain some insight into the cases where the fiber diameter is many times larger than the wavelength, we simulated the absorption of the active layer using two different wavelengths, at 200 nm and 350 nm. We numerically

computed the absorption by the active layer when the fiber diameter was increased from fiber diameters of 1 μm up to 18 μm. To better single out the contribution of the active layer to the light absorption, in this numerical calculation we did not consider any parasite absorption that may originate in the substrate or first transparent electrode. The indexes of refraction (n) and extinction coefficients (k) used for all the layers are given in Table 2.1. Note that for the extinction coefficient we have used a fixed value that corresponds roughly to an average for several of the organic PV materials currently in use. In fact, for the case of 350 nm the values correspond to the actual measured values when the organic used is a bi-layer of DBP/C70 which is the same one considered in the experiments reported in Chapter 5 of the current thesis.

Table 2.1. Summary of the index of refraction n and extinction coefficient k for each layer used in the simulation. The extinction coefficient of the transparent electrode was set to zero because in this zone it has its maximal values and we were only interested in the absorption behavior of the active layer.

Material	Optical Constants @ 200nm		Optical Constants @ 350nm	
Transparent Electrode	n=2.34	k=0	n=2.18	k=0
Active Layer	n=1.7	k=0.5	n=2.19	k=0.50
Metallic Contact	n=0.28	k=3.61	n=0.38	k=4.27

We computed the absorption of the active layer and we observed that it rose as long as the fiber diameter was increased. As observed in the previous calculations when the fiber diameter was small the enhancement was of only 4% but as long as the diameter was increased such enhancement grew above 10%. In the case where the wavelength was set to 350 nm some wiggles

appeared resulting in a slower enhancement increase, whereas for the case of 200 nm, beyond 4 μm diameter it grew, more or less, linearly. The latter calculation is the one that more resembles to a case were standard fibers would be used. The growth in absorption seen in Figure 2.8a is such that, for a 2 μm increase in fiber diameter, the absorption increases by 1%. If we extrapolate such enhancement, one would expect that at 80 μm the enhancement would be about 40%. On the contrary, when we consider incidence at 50 deg we do not observe the same increase. As shown in Figure 2.8c, there is little change in the absorption as the fiber diameter gets larger.

a

b

c
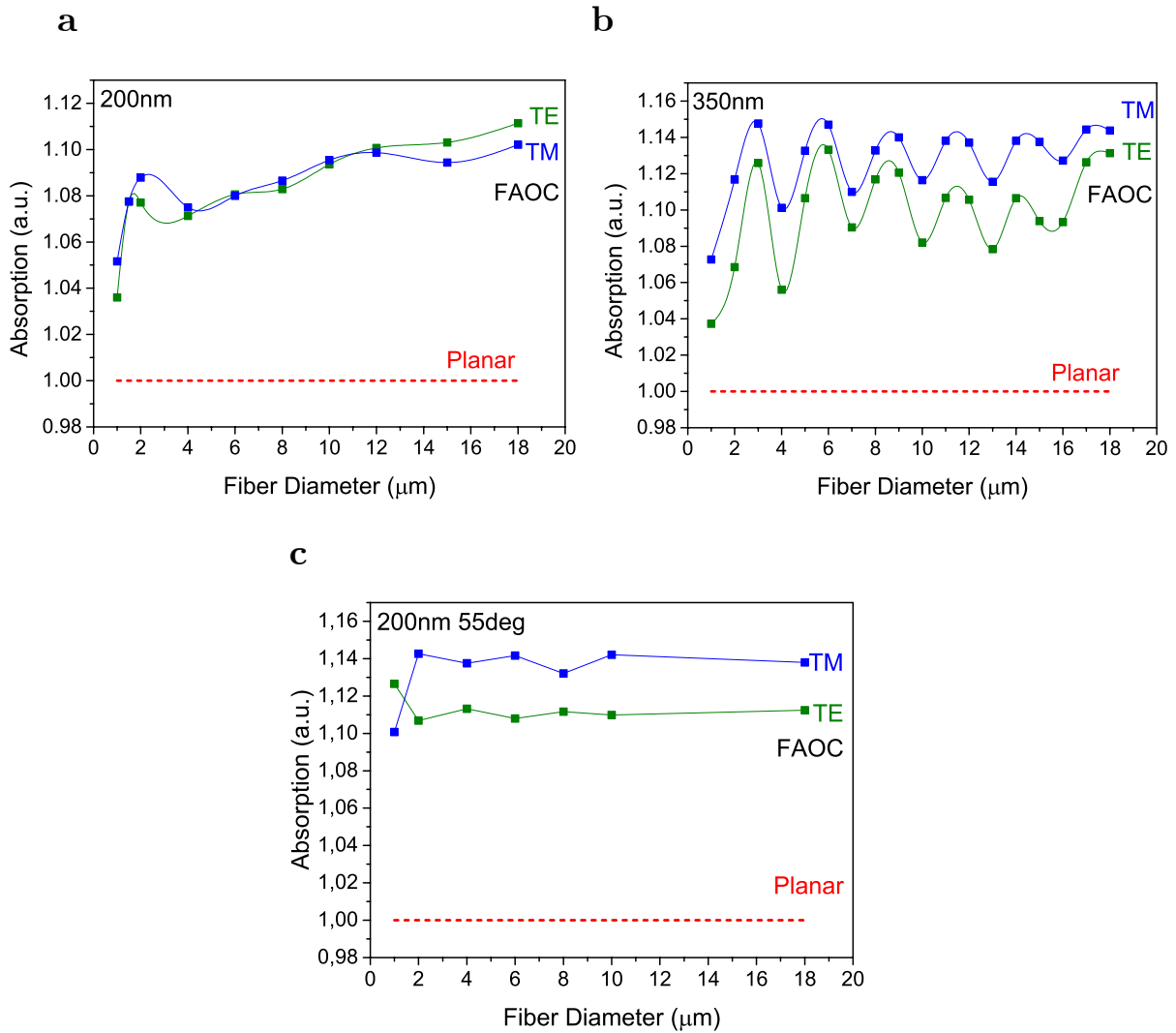
Figure 2.8. Comparison of the absorption of FAOC and the planar predicted with the model for small wavelength and big fiber diameters. a) Absorption of the blend as function of the fiber diameter for a wavelength excitation of 200nm in TE (green squares) and TM (blue squares) polarizations, for comparison the planar response (red dashed line) is also depicted. b) Absorption of the blend as a function of the fiber diameter for a 350nm. c) Comparison of the absorption at 0 deg (square dots) and 55 deg (black dots) of the FAOC as a function of the fiber diameter. The solid lines for the FAOC response are only a guide for the eye.

The spatial distribution of the electric field norm for two different sizes of fibers was also computed but keeping the same excitation wavelength. As we are dealing with microscopic sizes a geometric optics approach implies that

at zero incidence angle the curvature of the fiber should behave as lens focusing the light into the active layer zone. But from cross sections of the field intensity distribution, shown in Figure 2.9, we observed that not only is the light focused into the central part of the active layer, but also some lower intensity lobes along the rest of the active layer zone. Those lobes could be distinguished clearly when the fiber diameter is larger than 4 μm, as well as for the 18 μm fiber diameter (cf. Figure 2.9b).

a

b
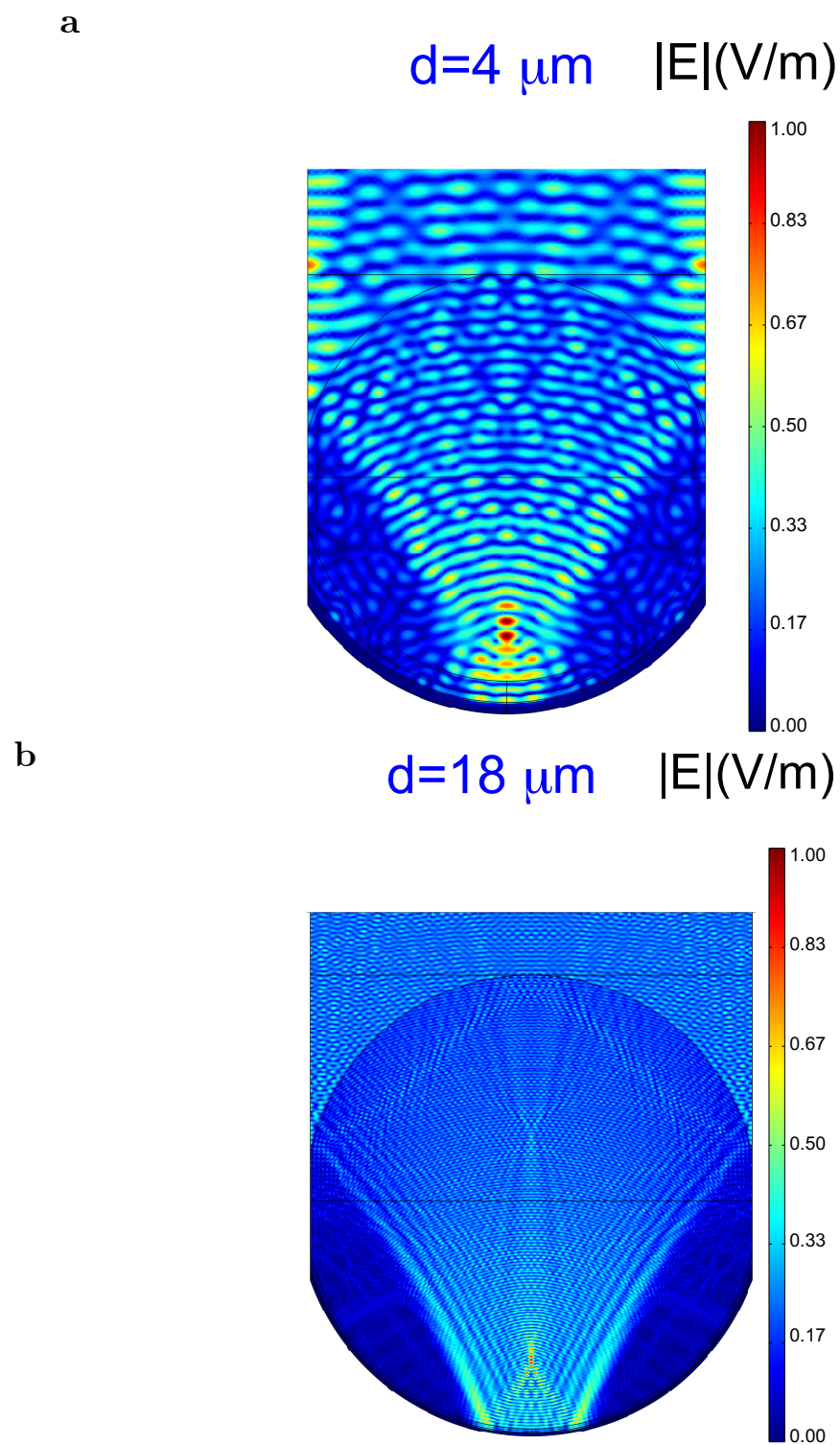
Figure 2.9. Spatial electric field distribution for the TE polarization with an excitation wavelength of 350nm for fiber diameter of 4 μm a) and 18 μm b) and the incidence angle was set to 0deg. Both fibers are normalized to the same color coding.

2.4 Conclusions

The numerical study performed in this chapter leads to the conclusion that light absorption is strongly dependent on the size of the fibers. We may group such behavior under two categories, one where the size of the fiber is relatively small or comparable to several wavelengths, and another where the size of the fiber is many times larger than the wavelength. In the former scenario, light coupling in the WGM provides an explanation to the reported enhancement while, in the latter one, the enhancement seems to be provided by some kind of light trapping in the fiber array itself. This trapping leads to an effective absorption everywhere in an active layer that is approximately 1.5 times larger when compared the active layer of the planar configuration.

For the small diameter fibers we have demonstrated that the incident light is coupled to low-Q WGM of the fiber array. Such coupling is effective for a broad range of wavelengths as required when converting light into electricity from a wideband source like the sun. Our numerical study shows that for small diameter fibers the number of absorbed photons per unit area increases as the sun inclination relative to the cell normal increases from 0 to 55 deg.

This may be significant for several applications. For instance, at a Latitude close to 40 deg the slope of a fixed PV installation on a rooftop is typically 35 deg. At such latitude the Sun would be 55 deg above the horizon line, any kind of standard PV installation integrated on a building façade should be at 55 deg of the optimal orientation. For the FAOC a maximum

efficiency would be obtained at 55 deg, ensuring an optimal light harvesting for vertical installations. On the other hand, for mechanically fixed PV installations the lack of sun tracking leads to a rather inefficient energy harvesting. Indeed, at a Latitude of 40 deg up to 38% more energy could be harvested by maintaining the plane of the PV installation perpendicular to the sun at all times[56]. In the event that the longitudinal axis of the FAOC would be oriented in the meridian direction, the angular increase in power conversion efficiency would provide, over the course of one day, an energy harvesting capacity 17% times larger, equivalent to a "half" tracking of the Sun movement.

For large diameter fibers the numerical calculations indicate that at normal incidence light harvesting increases as the fiber diameter increases. On the contrary, no change seems to be occurring when incidence is at 55 deg. The field intensity maps indicate that a WGM coupling is no longer applicable. At normal incidence the field amplitude appears to be spread over all the perimeter of absorbing material. However, at the time of writing this thesis, the limitations of the computational tools we used did not allow us to draw a clear conclusion on what the mechanism of light trapping an enhanced absorption that may occur for such large fiber diameters is. New mathematical or numerical tools need to be developed to fully elucidate the nature of light trapping and absorption for such configuration.

3 | Dip coating applied to the fabrication of organic solar cells

As it discussed in Chapter 2, OSC may be deposited over non-flat substrates to increase the light harvesting capacity of the cell or to find applications for the photovoltaic technology where flat rigid substrates are not the optimal solution. Many of the procedures used for the deposition of thin layers of organic materials as, for instance, spin-coating, printing, or slot die, may not produce the optimal results when the substrate is non flat. In this chapter we consider the fabrication of organic cells using dip-coating processing. The dip-coating procedure described is based on the immersion of a substrate in a solution of the organic material to be used as active material for the device. The dip-coating is applied to fabricate bilayer, as well as, bulk heterojunction cells. In section 3.2 of the current chapter we compare the performance of such cells relative to similar cells fabricated using the standard spin-coating procedure. To properly benchmark the dip-coating procedure against the spin-coating one, which produces excellent results when the substrate is flat, in this chapter we applied the technique only over standard ITO covered flat glass substrates. In Chapter 3 the viability of the dip-coating procedure to fabricate organic cells will be evaluated when applied to different kinds of non-flat substrates. In section 3.3 we repeated the dip-coating procedure six times using different substrates to monitor any degradation in the cell performance when the solution was reused several times.

3.1 OSC Fabrication by dip-coating

The dip-coating technique for the deposition of thin layers of organic polymers or small organic molecules involves substrate immersion into a solution of the organic material constituting the final material composition for the layer and then withdrawing it at constant velocity from the solution bath. A sketch of this technique is shown in Figure 3.1. A setup formed by a compact motorized translation stage plus the container was mounted inside a glove box. Such motor was connected to a computer to control the velocity, which was set to v= 0. 5 mm/s for all the layers deposited in this chapter. Layers formed from dichlorobenzene (DCB) solvent required additional time inside the glove box to be dried, whereas the ones from dichloromethane (DCM) were already dried when removed from the solution.
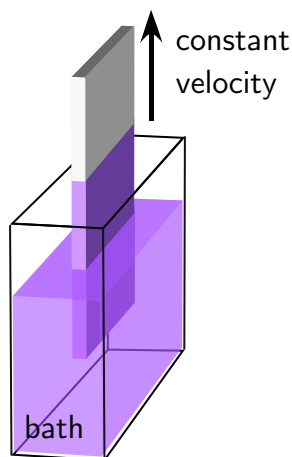
Figure 3.1. Scheme of the dip-coating technique. The layer is formed when the substrate is withdrawn at constant velocity from the bath, which contains a solution of the organic material.

In this chapter we considered OPV cells fabricated using poly-3(hexyl-thiophene) (P3HT) as donor material and [6,6]-phenyl-C61-butyric acid methyl ester (PCBM) as acceptor. To fabricate bilayer cells we used the orthogonal solvent procedure[57] in order to not dissolve the first layer when the second one was deposited on top. For such bilayer cells, P3HT was dissolved in DCB and then deposited by spin or dip coating on top on ITO/Glass substrate where a 5 nm layer of NiO had been previously sputtered. PCBM was dissolved in DCM and then deposited on top of the P3HT layer. The cell was finished with a thin HBL of $LiCoO_2$ sputtered on top of the blend and an Al electrode evaporated on top of the HBL. Similarly bulk heterojunction cells were fabricated with the same electrodes but using a solution with a mixture of P3HT and PCBM in DCB solvent and again spin or dip coated on top of the NiO. The architecture of the bilayer and the bulk heterojunction is shown in Figure 3.2. The main difference between these two architectures is that in the former the donor and acceptor layers are separated leading to a better contact with the electrodes but a poorer interface area. As explained in Chapter 1 of the current thesis, for the bulk heterojunction device the donor and acceptor are intermixed maximizing the contact area between them and promoting the exciton splitting but the proper metallic contacts is not ensured.
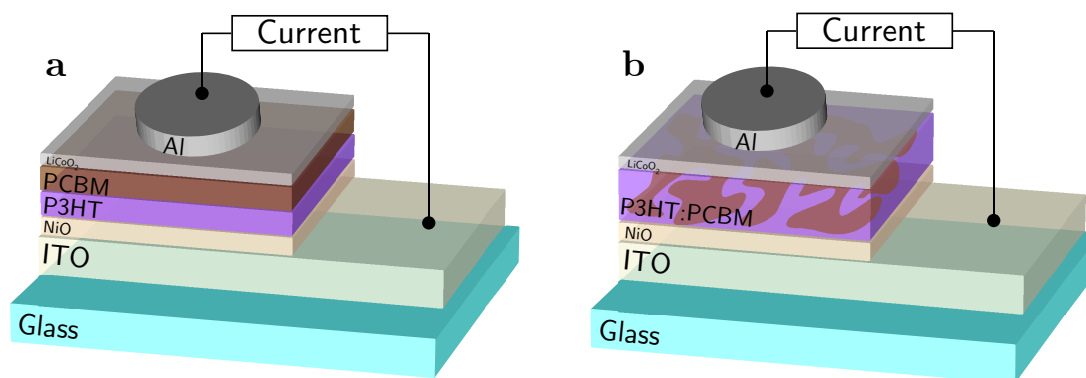
Figure 3.2. Sketch of the two different device architectures fabricated. a) A bilayer device where the donor (P3HT) and the acceptor (PCBM) form two layers deposited separately. b) A bulk heterojunction device where the donor and acceptor are intermixed prior to its deposition.

To characterize the thickness of the dip-coated active layer different glass substrates were immersed in bath solutions of the desired material. By measuring the profile of a scratch made on the sample is possible to obtain an absolute value for the thickness when using an Atomic Force Microscope (AFM) in the taping mode. Using the Beer-Lambert law we could relate the transmission of each layer with its thickness. With this relation the rest of the thicknesses can be directly estimated from light transmission at 550 nm, which corresponds to an absorption maximum of P3HT, through the dip-coated samples. As can be seen in Figure 3.3, we found a linear growth of the thickness versus the solution concentration.
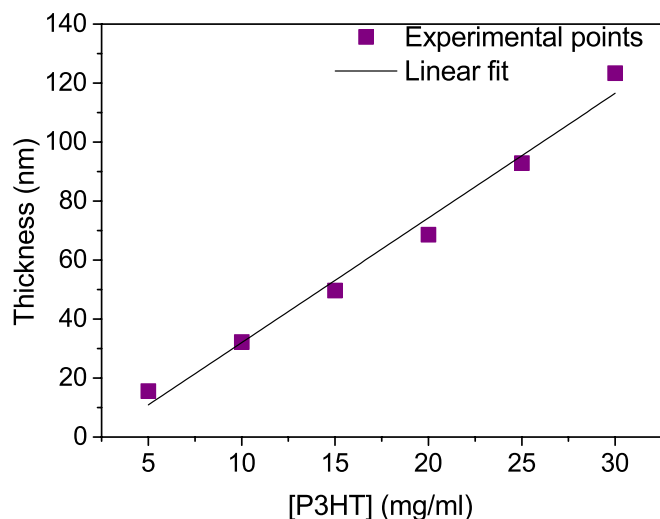
Figure 3.3. Thickness of a P3HT film as a function of the concentration of P3HT dissolved in DCB. The square points correspond to experimentally measured thickness at each concentration and the solid line a linear fit. It can be seen that the solution concentration is linearly correlated with the thickness of the dip-coated film. In the inset of the graph is depicted the dip-coating technique.

3.2 Photovoltaic characterization of devices

For the bilayer device, different thicknesses of donor and acceptor were tested in order to balance their carrier transient times[57]. As seen in Figure 3.3, by increasing the concentration of P3HT one could obtain layers of 50 nm and 70 nm. We tested different devices by combining these P3HT layers with 25nm of PCBM. The results are summarized in Table 3.1. We found that the optimal layer thickness were 50 nm of P3HT and 25nm with PCBM, since the FF is higher leading to a better cell efficiency. Such layer thicknesses are the adequate ones for an optimal combination that maximizes simultaneously light absorption and charge collection and recombination outside the cell. Two

devices with the same thickness of active layer were fabricated one by dip coating and another one by spin coating. The current density of the fabricated devices as a function of applied voltage is shown in Figure 3.4 and their PV device parameters are summarized in Table 3.1. We observe that the performance of these devices is very similar and any difference can be attributed to statistical variations originated from the device preparation procedure.
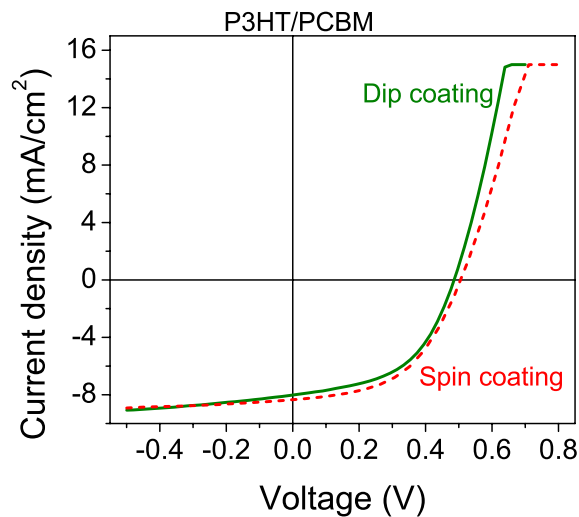
Figure 3.4. Intensity versus voltage curves of two bilayer devices whose active layer has been deposited by dip coating (green solid line) and spin coating (red dashed line), the active layer thicknesses are 50nm P3HT and 25 PCBM for both dip-coated and spin-coated device. Both curves are very similar which means that dip-coating technique is an alternative to the spin coating one.

Table 3.1. Performance details of fabricated bilayer devices under a solar simulator of AM1.5G. Different donor thicknesses were tested to optimize the fabricated devices.

Deposition technique	J_{sc} (mA/cm^2)	V_{oc} (V)	FF (%)	PCE (%)	P3HT Thickness	PCBM Thickness
Dip coating	-6.945	0.518	49.15	1.77	70 nm	25 nm
Dip coating	-8.016	0.486	50.88	1.98	50 nm	25 nm
Spin coating	-8.342	0.505	50.38	2.127	50 nm	25 nm

As mentioned we also tested the dip coating technique for fabricating bulk heterojunction devices. In this case we used a blend concentration of 1:1 in weight, this concentration has been already tested for the fabrication of solar cells processed in ambient air[58]. Again, two devices were fabricated, one using the dip coating and the other using spin coating technique. The current density versus voltage curves are shown in Figure 3.5 and a summary of their device parameters is in Table 3.2. The discrepancy between their values is probably due to electrical contacting differences because as in bilayer devices one substrate contains 8 cells, which are contacted manually. Moreover, a slight improvement for the dip coating devices was found, which may be attributed to the more uniform coating obtained when using this technique. Indeed, the dip coating technique avoids the problem with spinning borders since the entire substrate is wetted in the same way.
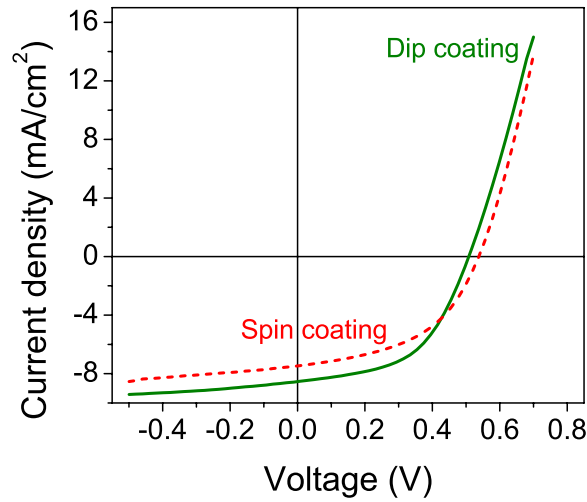
Figure 3.5. Current density vs. Voltage curves of bulk heterojunction devices with the same layer thicknesses, the active layer has been deposited by dip coating (green solid line) and spin coating (red dashed line). It can be observed that the dip-coating performance is slightly better in terms of current density.

Table 3.2. Performance details of bulk heterojunction devices fabricated and tested under AM1.5G simulated illumination.

Deposition technique	J_{sc} (mA/cm^2)	V_{oc} (V)	FF (%)	PCE(%)
Dip coating	-8.537	0.508	51.91	2.25
Spin coating	-7.358	0.535	51.67	2.04

3.3 Reusability of solutions

When applying the dip coating technique one may store the solution once it has been used and then reuse it for subsequent depositions. This would prevent a large waste of material that would be incurred, otherwise, in a continuous fabrication of many different cells. However, such procedure is not

exempt from problems. The active material concentration in the solution may diminish as it is being deposited on the substrates and the walls of the container. Additionally, the immersion of the substrate in the solution may introduce contaminants in such solution that may have a negative effect on the performance of the cells that would be fabricated subsequently. As a first step to test the viability of solution reuse, we considered the deposition of a total of six bulk heterojunction cells using the same solution. The six different substrates were dip-coated one right after the other and then the rest of fabrication steps to obtain the OPV cells were applied simultaneously to the six devices.

The photovoltaic parameters for the six cells are shown in Figure 3.6. Special attention should be given to the V_{oc} and FF which are less sensitive to, for instance, small deviations in the useable area, defined by the intersection of the ITO electrode and the top metal electrode, among the different cells considered. For such two parameters there is no apparent trend in Figure 3.6 that would indicate degradation of a given cell in relation to its number order. One may extract the mean value for each PV parameter and the corresponding percent standard deviation; J_{sc}=-6.363 mA/cm^2 $\pm$ 6.5%, V_{oc}=-0.495 V $\pm$ 3.8%, FF= 48.19 $\pm$ 6.3% and PCE $=$ 1.52 $\pm$ 6.5%. Note that the smallest dispersion is found for the Voc and the FF.
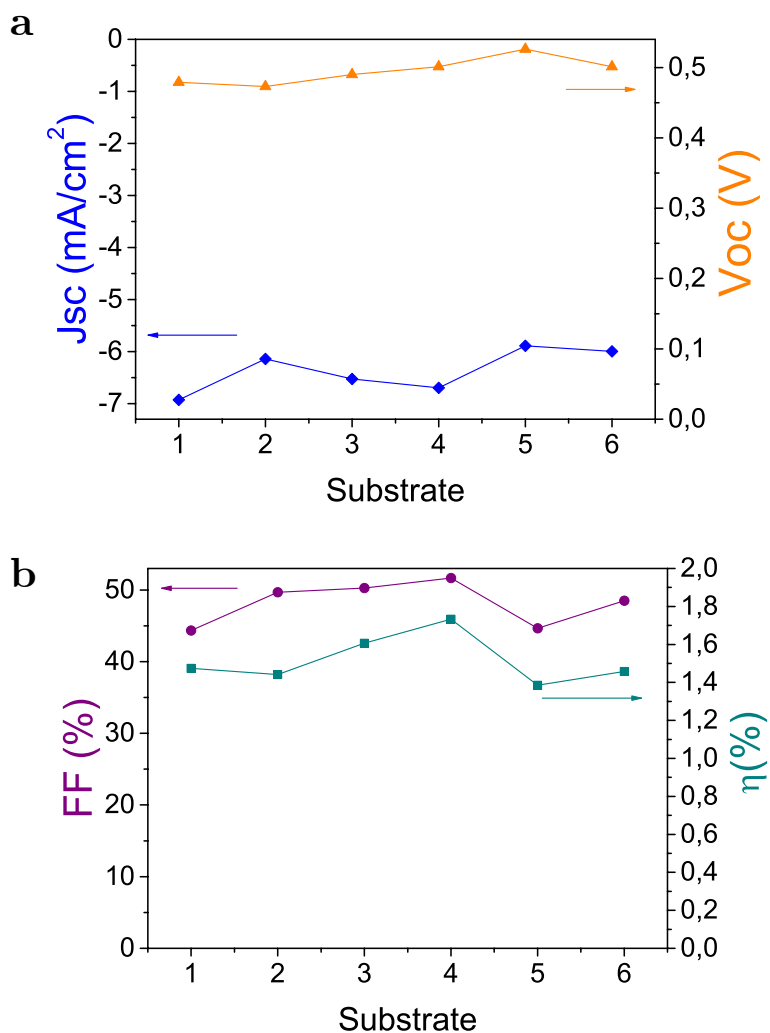
Figure 3.6. Comparison of the electric parameters from six different substrates fabricated from the same blend solution. **a)** Current density in short circuit (blue diamonds, left y axis) and voltage in open circuit (orange triangles, right y axis). **b)** FF (purple circles, left y axis) and solar cell efficiency (green squares, right y axis). The number sequence in the x-axis is in correspondence to the order in the organic blend deposition, in other words, No. 1 corresponds to the first cell deposited while No. 6 corresponds to the last one.

3.4 Conclusions

One technique that has been given little attention for the fabrication of OSC is the dip coating. As opposed to spin coating, such technique offers the possibility to fabricate cells over surfaces that are not necessary flat. Both bilayer and bulk heterojunctions were fabricated using the dipping procedure and performed similarly to the cell fabricated using the traditional spin coating. In this chapter we have demonstrated that the dip-coating technique can be used for depositing the active layer in planar substrates. In the next chapter such technique will be explored for non-flat ones.

Additionally, we have shown that the same solution can be used to fabricate several substrates with the dip-coating technique. We observed no decrease in the photovoltaic performance between the first and the last substrate coated, which opens a way to implement this technique for continuous mode fabrication. Such technique may allow for a large scale fabrication of OSCs.

4 | Fabrication of organic solar cells in non-conventional substrates

In Chapter 2 of the current thesis we performed a theoretical study that demonstrated the advantage of having a micro-structured substrate to obtain an optimal light harvesting. The type of structure we analyzed in detail consisted of an array of glass fibers with an organic cell that is meant to be deposited on one of the sides of such array. The deposition of the cell on such curved surfaces is not straightforward provided it combines different deposition techniques (sputtering, spin-coating and thermal evaporation), which produce excellent results when applied to planar substrates but not necessarily when applied over to micro or nano-structured surfaces. Such issues must be carefully addressed, otherwise, one may succeed in improving the light harvesting but at the cost of degrading the electrical performance of the device.

In Chapter 3 we considered the substitution of spin-coating by dip-coating that, in principle, should be applicable over not flat substrates. However, other issues may arise when we consider the deposition of the rest of the layers in the cell, which are non-solution processed.

In this chapter we will focus on the deposition of the first transparent electrode, which is typically fabricated from an ITO target using sputtering as

the deposition procedure. We will show that, to be able to obtain optimal quality electrodes when the substrate exhibits valleys and peaks as in the fiber arrays studied in Chapter 2, several modifications must be introduced in the standard sputtering procedure to obtain a homogenous ITO layer with a good optical and electrical performance. In a second part of the chapter, we will combine such non-standard ITO sputtering procedure with the active layer dip-coating procedure reported in Chapter 3 and fabricate cells on fiber arrays and on single fibers. The PV performance of the fabricated cells will be carefully analyzed. When needed, alternative routes to the procedures considered in here will be proposed at the end of the current chapter. The end goal is to obtain cells with electrical properties similar to the cells fabricated on planar flat substrates.

4.1 ITO transparent electrode fabrication

Transparent conducting oxides are of the utmost importance for many microelectronic applications, as they can be used as transparent electrical contact electrodes in displays, touch screens and thin film solar cells[59-62]. The most commonly used semiconductor for such coatings is indium tin oxide (ITO) because of its high electrical conductivity and optical transmittance.

Magnetron sputtering is the most used technique for depositing ITO layers and a schematic view of such technique is shown in Figure 4.1. The goal is to obtain stable film properties with exceptionally low resistivity and

high transmittance within the visible spectrum range[63-67]. The sputtering technique involves ejecting material from a target, that is the source material, to be deposited on a substrate located, target and substrate, in a vacuum chamber. An inert gas is introduced at low pressure. A power supply strikes such gas and a plasma is created. Afterwards these ions are accelerated towards the surface of the target, causing the source material to break off from the target in vapor form and condense on all surfaces including the substrate. The kinetic energy of ionized particles of the plasma gas is high; as a consequence the atoms sputtered from the target have also high kinetic energy. One of the relevant characteristics of this technique is the conformal coverage of the substrate by the source material. The film composition can be easily tuned by controlling the sputtering power, the working pressure or the flowing of gases.
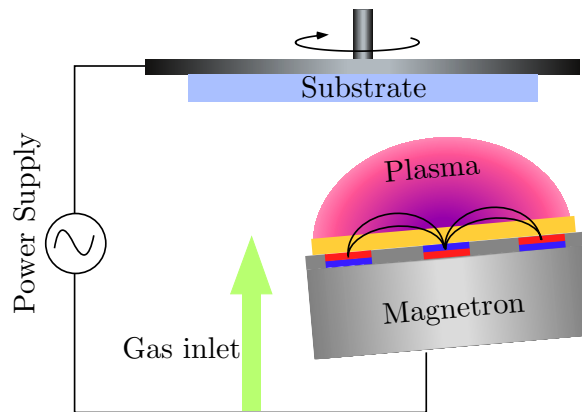
Figure 4.1. Schematic view of the sputtering technique. A gas is introduced in a high vacuum chamber, and a plasma of such gas is created on the magnetron where is positioned the source material. The ions of the gas are accelerated towards the target as they are ejected in all directions. A vapor of material finally reaches the substrate placed in a rotating support. A thin film of the target material is formed on the substrate surface.

4.1.1 ITO sputtering procedure

DC sputtering of ITO layers was performed in a commercial sputtering system (Orion 8, AJA International) equipped with a load-lock. An ITO target (In2O3/SnO2 90/10 wt.%, purity 99.99%, Kurt J. Lesker Company) with a diameter of 5 cm was used as source material. Glass substrates (Eagle Glass, Coresix) were coated with an ITO layer for the transmission and electrical measurements. A substrate cleaning was performed prior to sputtering deposition; such cleaning involved rinsing with methanol, drying in an oven at 120ºC for 5 min and oxygen plasma inside the sputtering chamber for 15 min. During oxygen plasma cleaning the substrate was heated up to 100ºC and such temperature was maintained during the deposition process. The working pressure was 2 mTorr, the target power was set to 70 W and the gas mixture of Ar:O$_2$ was varied. Transmission measurements were performed on the ITO-covered glass substrates using a spectrometer (Lambda950, Perkin Elmer) for the visible wavelength range. The surface resistance was determined from the slope of Intensity-Voltage measurements (Keithley 2420).

4.1.2 Transmission and Resistance of ITO layers on flat substrates

Different substrates were coated with ITO using the same 1.75% in volume mixture of O$_2$:Ar, but different thicknesses to understand its effect on the transmission of the layer. The transmission of the substrates coated with 140 nm and 220 nm of ITO are compared in Figure 4.2a. The sample containing 140 nm of ITO had a maximum 90% transmission at 530 nm. Such transmission slowly decreased to 86% at 800 nm. Whereas the thicker sample,

its transmission had more variations in the same range. Adding more oxygen in the sputtering gas may increase the transmission of the 140 nm ITO layer[64]. We obtained a transmission above 92% when the O_2 concentration was increased from 1.75% to 2% in volume (cf. Figure 4.2b).

The other major aspect to consider when fabricating the ITO electrode is to the resistance of the deposited layer. A summary of the measured resistances and optical transmissions at 530 nm are given in Table 4.1. We observe that thicker layers had lower resistance but less transmission. If more oxygen was added the transmission increased, but the resistance doubled since an increased oxygen content may decrease the carrier density[65].

a

b
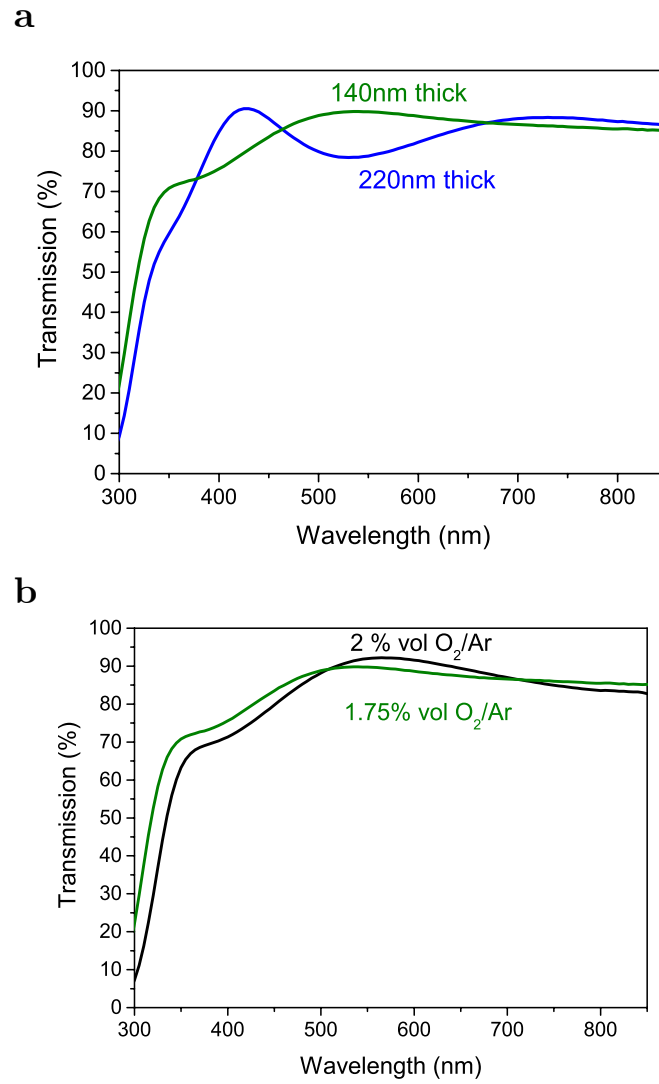
Figure 4.2. Transmission measurements of ITO sputtered layers on planar substrates. a) Comparison of transmission spectra of layers with different thicknesses. ITO transmission measured from a 140 nm thick layer (green line) and from a 220 nm thick layer (blue line).. b) ITO layers fabricated with the same thickness (140nm) but varying the gas inlet composition: 2% vol O_2:Ar (black line) and 1.75% vol O_2:Ar (green line).

Table 4.1. Summary of the electrical and optical properties of the fabricated ITO layers.

Method	Thickness	Gas Mixture (O_2:Ar)	Resistance	Transmission at 530 nm
DC Sputt.	140 nm	1.75% in vol	52 Ω	89.75 %
DC Sputt.	220 nm	1.75% in vol	48 Ω	78.43 %
DC Sputt.	140 nm	2% in vol	110 Ω	91.05 %

As a summary, to fabricate the optimal ITO high transmission and low resistance must be well balanced. In Figure 4.3 the transmission of a 140 nm ITO layer fabricated with a 1.75% in volume gas mixture of O_2:Ar is compared to the absorption of the active PV materials used in this thesis. We observe that for the wavelength range where the active materials absorption is maximum, the variation in the transmission of the ITO is not larger than 2%. The resistance for the ITO layer was kept very low too. Thus, the sputtering conditions for depositing such electrode will be used for fabricating the transparent conducting oxide of our OSC.
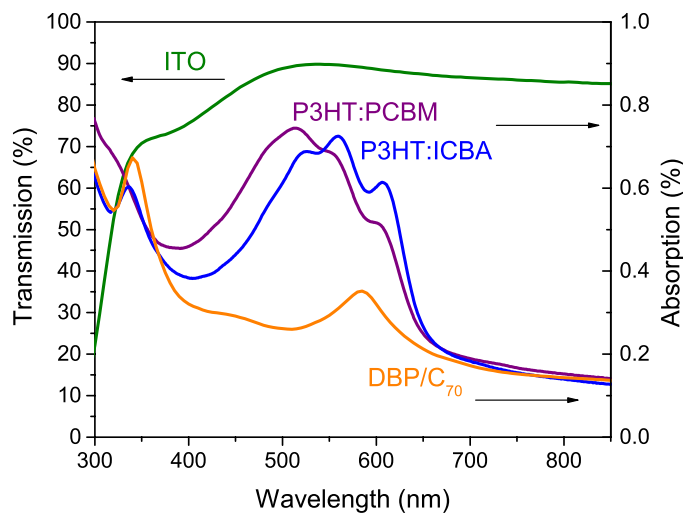
Figure 4.3. Transmission of ITO compared with the absorption of the materials used as active layers in this thesis. Our fabricated 140 nm ITO (green line) with a gas mixture of 1.75% in volume of O_2:Ar.

4.1.3 ITO on deposited non-flat substrates

As it will be shown in Chapter 5, one of the non-flat substrates to be covered by ITO is a microstructure formed with several small-diameter fibers adjacent to each other to form the array of parallel fibers proposed in Chapter 2. If such substrate is placed in the center of the rotating sample holder (cf. Figure 4.4a) the ITO deposition is not homogenous provided the normal to the array is at a constant angle relative to the target orientation. By placing the substrate at an angle and displacing it from the center, as depicted in Figure 4.4b, we achieved a wiggling motion for the substrate normal relative to the target orientation. Such motion lead to an ITO layer homogeneously covering the entire bottom side of the fiber array.
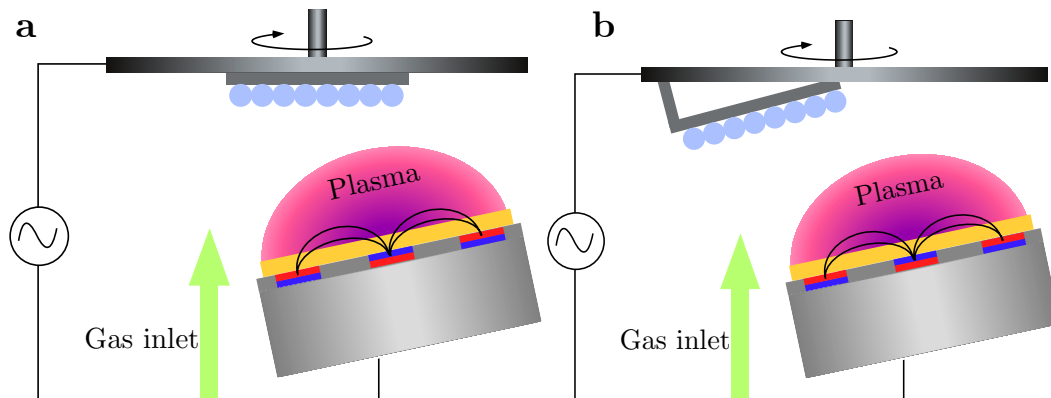
Figure 4.4. Configuration of the fiber arrays for the ITO deposition. a) Deposition in the standard configuration. b) Deposition by specially positioning the substrate to obtain a wiggling motion for the substrate normal. The triangular piece was made of a good heat conductor to preserve a good thermal contact between the substrate and holder.

In the fiber arrays there are two directions to measure the sheet resistance, parallel to fiber direction as in Figure 4.5a and transversal to fiber direction as depicted in Figure 4.5b. The values obtained for sheet resistances of the sputtered ITO layers are summarized in Table 4.2.
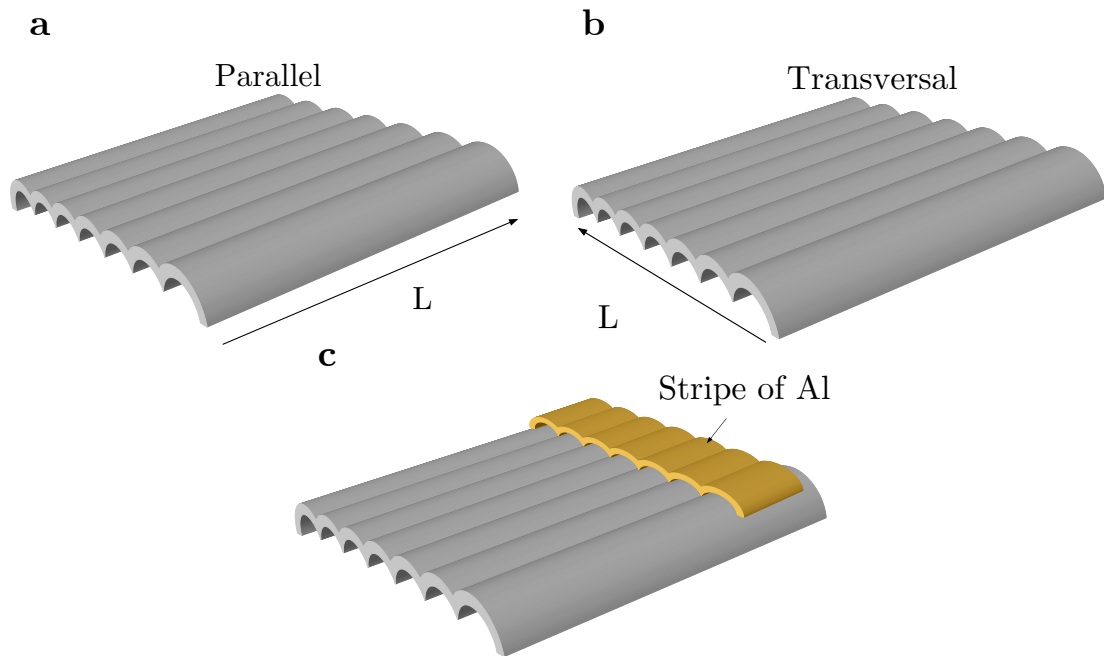
Figure 4.5. Direction for measuring the sheet resistance. a) Current flow aligned parallel with the fiber array, b) Current flow perpendicular to the alignment of fiber arrays. c) Deposited stripe of Al.

The measured R_s in ITO layers deposited with the configuration shown in Figure 4.4a was 350 $\Omega/\square$. On the other hand, when the micro-structured substrates were slightly tilted (cf. Figure 4.4b) the resistance in both directions is diminished. To further enhance the conductivity of such layers, a metallic strip of aluminum (Al) at the end of the fiber array must be deposited. With such strip, the R_s of the deposited ITO in the tilted case was lowered to about half its value. The final sheet resistance of 28 $\Omega/\square$ is of the

same order as the one measured for a planar substrate fabricated using the same sputtering conditions.

Table 4.2. Measured sheet resistance for the ITO films deposited on the back side of fiber arrays.

Method	Direction	L (mm)	R_s ($\Omega/\square$)	R_s after Al ($\Omega/\square$)
Straight	Parallel	5	350	98
	Transversal	1.25	10 952	-
Tilted	Parallel	5	54	28
	Transversal	1.2	245	-

4.2 Active layer deposition

4.2.1 Dip-coating on non-flat substrates

Solution process when applied over nano or micro scale substrates was attempted in in the past but did not lead to uniform layers[68-70]. It was observed that when an OSC was deposited, an excess of polymer accumulated in the valleys, which led to high recombination losses and poor performance in that portion of the cell. While at the crest, one observed polymer depleted regions that caused shunts to the final devices. When considering our fiber array substrates, with the goal to circumvent such difficulties that other researchers found in the past, we proposed and tested different solutions.

a

b

Figure 4.6 Absorption spectra of deposited active layers. a) 220 nm thick blend layer deposited on a glass substrate from a solution containing P3HT:ICBA dissolved in DCB. b) Scattering of a FA without any deposited layer (black line) and absorption spectrum of the same FA covered with a layer of P3HT:ICBA deposited by dip coating from a solution of the blend in DCB (purple line).

To measure the thickness and to be able to characterize the deposited layers on fiber arrays, we measured absorption and used Beer-Lambert law relations to arrive to an expression that relates the thickness of the deposited layers on fiber arrays to the known planar substrate layer thickness:

$$\frac{l_f}{l_g} = \frac{[A^b_f - A_f] + \Omega_f}{[A^b_g - A_g]} \tag{4.1}$$

where l_f is the thickness of the blend on a fiber array, l_g is the thickness of the blend on a glass. A^b_f and A^b_g are the absorptions of the blend when deposited on fiber arrays and glass, respectively. A_f and A_g correspond to the absorptions of a bare fiber array and glass. And Ω_f accounts for the light scattering by the fiber array. A summary of the calculated thicknesses is shown in Table 4.3.

Table 4.3 Thickness relation between P3HT:ICBA deposited on a glass substrate and on a FA.

Sample	Approximate thickness (nm)
Bare P3HT:ICBA on FA	4.75
Heating 60ºC	4.81
Heating 100ºC	5.18
Heating 150ºC	28.57
PTE	2.57
DIO	3.60
Triton	33.49
Chloroform	85.27
Toluene	91.67

One of the first strategies we considered to increase the thickness of the deposited layer on fiber arrays was to rise the temperature of the solution bath. Such approach changes the surface tension of the solution and thicker layers are deposited, as seen in Figure 4.7a. However, the thickest layer obtained was only 30 nm. Unfortunately, the solution bath could not be heated beyond 150º without degrading the blend.

a

b
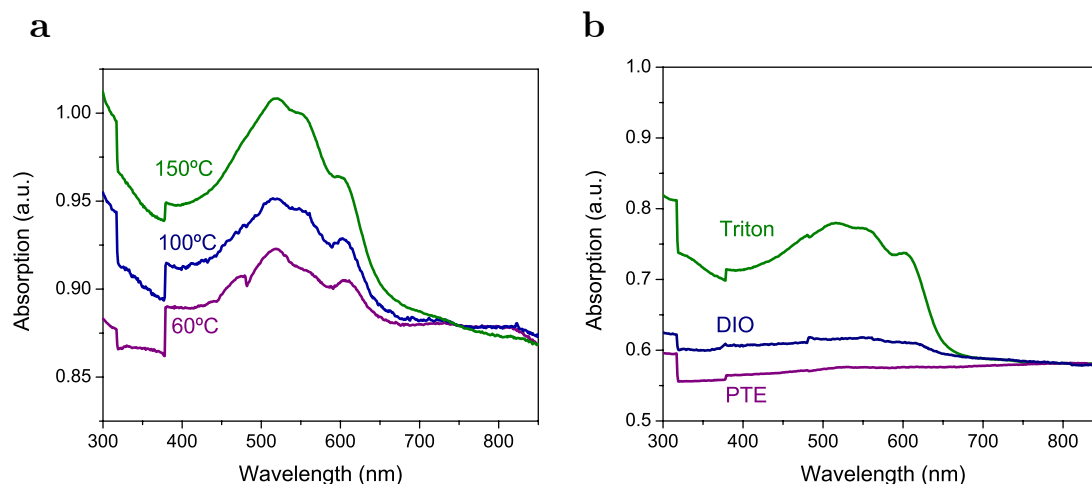
Figure 4.7 Absorption spectra of deposited layers. a) Comparison of layer absorption when the blend solution was heated during the dip coating at 60ºC (purple line), 100ºC (blue line) and 150ºC(green line). b) Absorption of blend layers when adding Triton (green line), PTE (purple line), and DIO (blue line) prior to dip coating.

A second approach to vary the surface tension was to use surfactants and additives. The formers being compounds that lower the surface tension of liquids[71], while the latters being solvents with a higher boiling points than the host solvent that provoke a slower evaporation of it and promote a better packing of molecules[72]. Two commonly used surfactants are Triton and Poly(ethylene glycol)12 tridecyl eter (PTE)[73,74]. A standard additive is diiodooctane (DIO)[75]. The absorption spectra of the layers deposited from solution baths containing such compounds is shown in Figure 4.7b. From the calculations using Eq. 4.1, none of them formed a thick enough layer.

Given that the two approaches above led to small changes in layer thickness, a more drastically route was adopted. Alternative solvents with lower boiling points, such as from solutions using chloroform (CF)[76] and

toluene $(T)^{77}$ were used for preparing the blend. The absorption using such new solvents is shown in Figure 4.8.
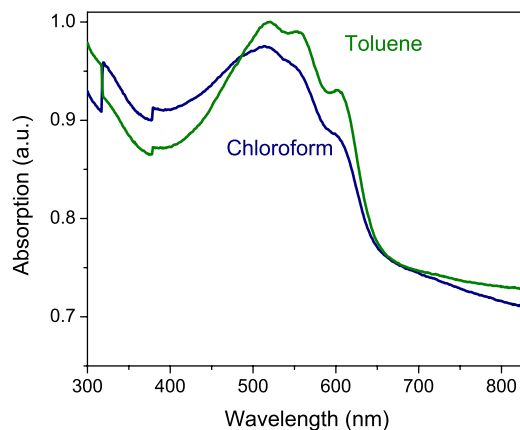
Figure 4.8. Absorption spectra of P3HT:ICBA dissolved in toluene (green line) and in chloroform (blue line).

If toluene was used as a solvent, a layer of 91 nm of blend was obtained. Such layer thickness is very similar to the one measured from our standard planar devices. In accordance, we decided to use such solvent for preparing our active layer for the OSC deposited on fiber arrays.

4.2.2 Fiber array cells fabricated by Dip-coating

Bulk heterojunction organic solar cells were fabricated with the architecture of ITO/NiO/P3HT:ICBA/BCP/Ag. Devices were made both on planar substrates to be used as a reference and on fiber arrays. The measured current density vs. voltage response is shown in Figure 4.9a for the planar and Figure 4.9b for the fiber array; the device parameters are summarized in Table 4.4. Details in the system used for extracting the photo-generated charges are explained in Chapter 5. Planar and FA substrates containing an OSC were prepared with the same layer thicknesses, however, as seen in

Figure 4.8, the performance of OSC on FA was considerably poorer than the ones on planar substrates.

a

Current density (mA/cm2) vs Voltage (V)

Planar OSC
by dip coating

b

Current density (mA/cm^2) vs Voltage (V)
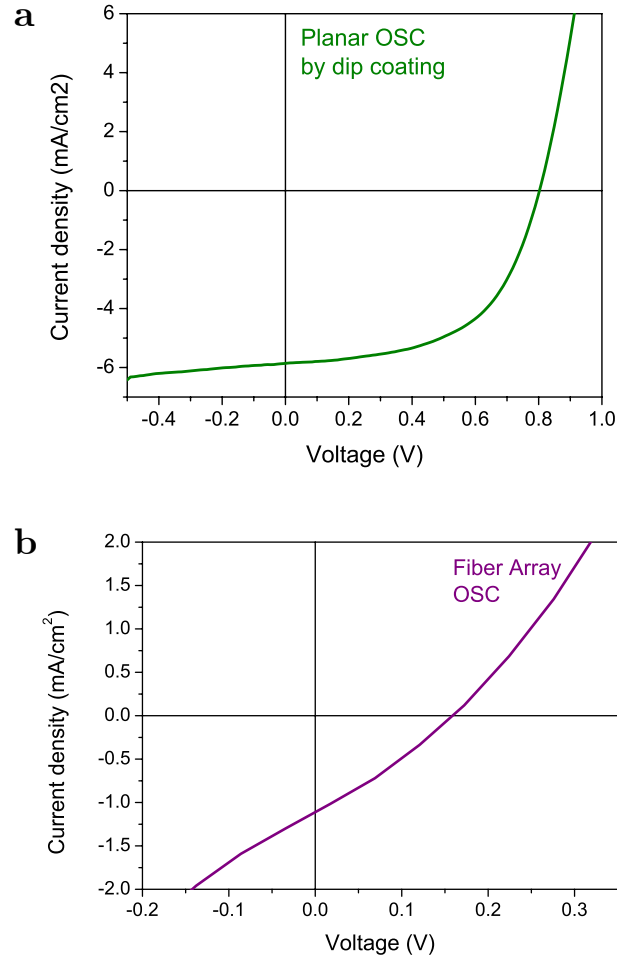
Fiber Array
OSC

Figure 4.9. Current density vs. voltage measurements of dip coated fabricated OSCs under 1 sun of illumination a) on a planar substrate, and b) on the back side of a fiber array.

Table 4.4. PV Performance of the fabricated OSC on planar and FA substrates

Organic Solar Cell	J_{sc} (mA/cm^2)	V_{oc} (V)	FF (%)	PCE (%)
Planar Reference	-5.862	801.820	55.53	2.61
Fiber Array OSC	-1.111	158.875	28.12	0.05

The current density obtained from OSC on the backside of fiber arrays was lower than on planar substrates. In addition, the V_{oc} and FF of OSC fabricated on the fiber array were severely affected. Although the optical transmission measurements indicated that both layers had the same thickness, the homogeneity of the layers on the fiber arrays could not be extracted from such measurements. To extract this information, SEM images of the cross section of the fiber array were obtained.

A SEM image of a fiber array formed by 10 fibers of 125μm is shown in Figure 4.9. Except from the first and the last fiber, the inner ones are aligned in the width of the array with respect to their centers. This fiber array corresponds to the substrate where the OSC whose J-V curve is depicted in Figure 4.9b was deposited. In Figure 4.11 we clearly observe a non-uniform deposition for the active layer. As seen in Figure 4.11a and 4.10b, there is a gradient of active layer thicknesses. In the valley in between two adjacent fibers (cf. Figure 4.11a) there is an accumulation of material, whereas in the slope from the valley to the peak of the fiber the thickness diminishes (cf. Figure 4.11b). Taking into account that the mobility of the charges in organic semiconductors is very low, such broad range of thicknesses from 2.5μm to about 70 nm, has a clear detrimental effect on the photovoltaic performance.
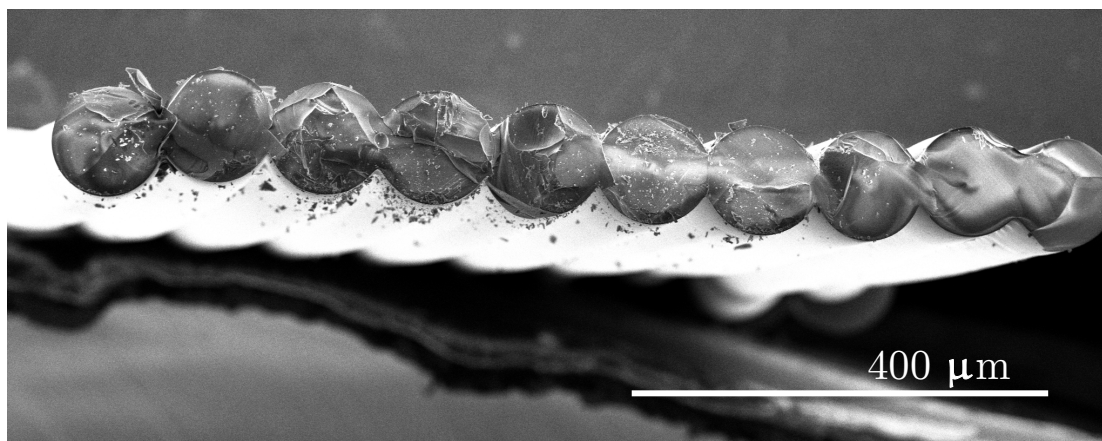
Figure 4.10. SEM image of a fiber array containing 10 fibers of 125 μm.

a

b
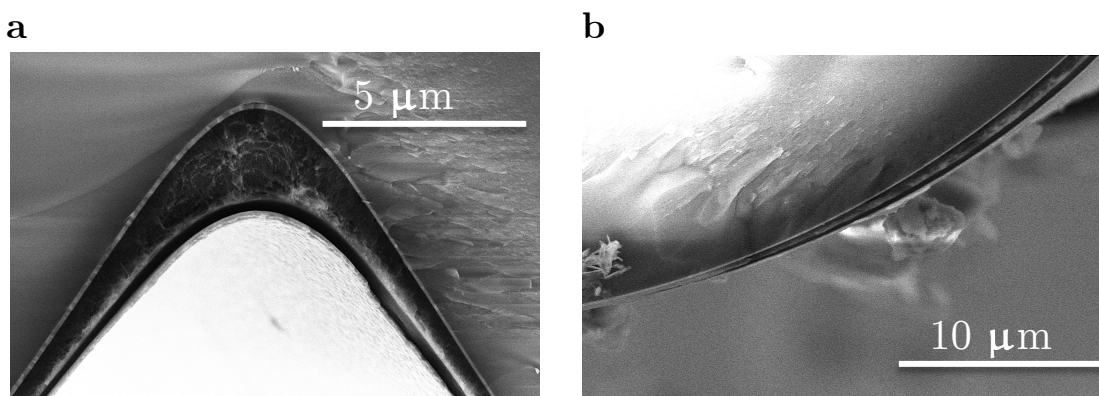
Figure 4.11. SEM images of OSC's cross section deposited on FA a) at the valley where two different fibers meet, and b) at the top of the fiber

4.2.3 Single fiber cells fabricated by Dip-coating

As indicated one of the main advantages of the dip-coating procedure is that it can be used, in principle, for fabricating OSCs on substrates having any kind of shape. In here we report the fabrication of the OSC on a cylindrical substrate. A schematic picture of the fabricated device is shown in Figure 4.12, the architecture of such OSC was ITO/NiO/P3HT:ICBA/LiF/Al.
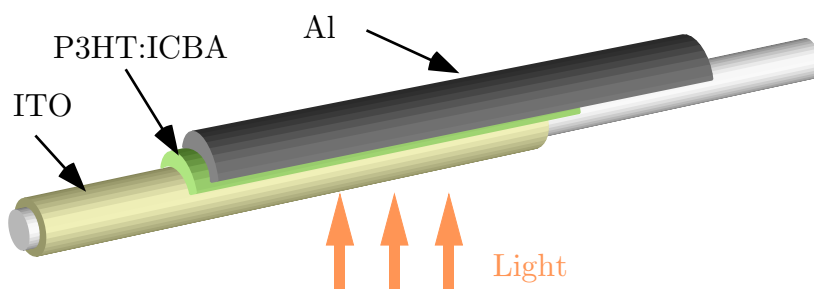
Figure 4.12. Scheme of an organic solar cell deposited on a single fiber. The transparent electrode is ITO, the active layer is P3HT:ICBA and the metallic contact is composed of Al. The effective area of the cell is the intersection of the three materials. The contacts for charge extraction are directly placed on the ITO and Al. For simplicity of the drawing we did not include the buffer layers, although they were present in the final device.

As the cylindrical substrate we used large multimode fused silica fibers 1 mm in diameter. After removing the protective polymer with tetrahydrofuran, ITO and NiO were deposited as explained in section 4.1. The active layer was deposited all around the perimeter of the fiber from a solution bath containing P3HT:ICBA dissolved in dichlorobenzene (DCB). The fiber was removed from the solution at the same velocity used for the planar substrates in the dip-coating procedure discussed in Chapter 3. About 1/3 of the fiber , which was not covered by ITO, was not immersed in the solution. After removal of the fiber from the solution, this later part we covered with a mask. We evaporated LiF and Al on the non-covered part. Because of the nature of the evaporation technique, only the side of the fiber that is visible from the crucible containing the melted Al or LiF was covered with such materials. Subsequently, to increase the crystallinity of the organic blend an annealing at 155ºC during 2 min was applied inside an oven. Finally, a plasma treatment was applied to remove the organic covering the fiber side

opposite to Al electrode to open a window for light transmission. The fabrication procedure is schematically shown in Figure 4.12.

Transparent electrode sputtering   Active layer dip-coating   Metallic electrode evaporation   Plasma etching
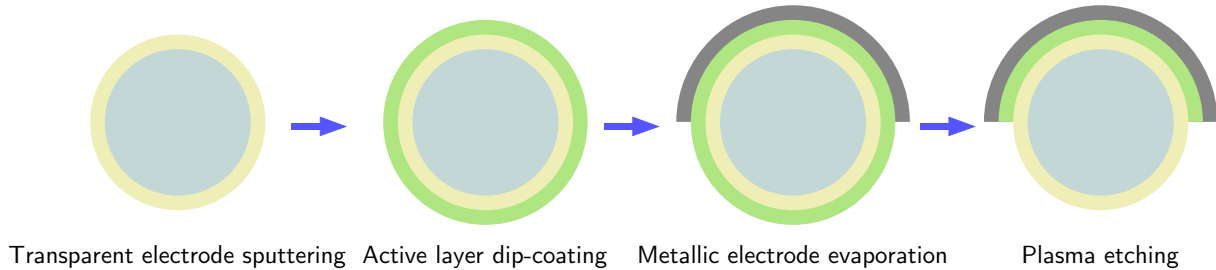
Figure 4.13. Schematic sequence of the OSC fabrication on single fibers.

PV measurements were performed by contacting the opposite ends of the fiber and using a Keithley 2400 to determine the current to voltage behavior of such fiber cell. The performance of the fabricated cylindrical OSC is summarized in Table 4.5 and the measured current density as a function of voltage applied in shown in Figure 4.14.

When we compare the performance of the single fiber cell with an equivalent planar cell (See Table 4.4) we observe a similar V_{oc} and a slight reduction in the FF. This clearly demonstrates the viability of the dip-coating technique when applied to such kind of non-flat substrates. On the contrary, when the substrate exhibits a micro-structuration as in the fiber array substrate considered in section 4.2.2, as explained above, the surface tension leads to an accumulation of the active material in the valleys in between fibers resulting in a highly inhomogeneous active layer, which eventually leads to a very poor electrical PV performance. On the other hand, from a simple geometrical optical analysis it seems quite clear that large fibers would simply

focus the sun light but, provide no significant improvement in the light harvesting capacity.
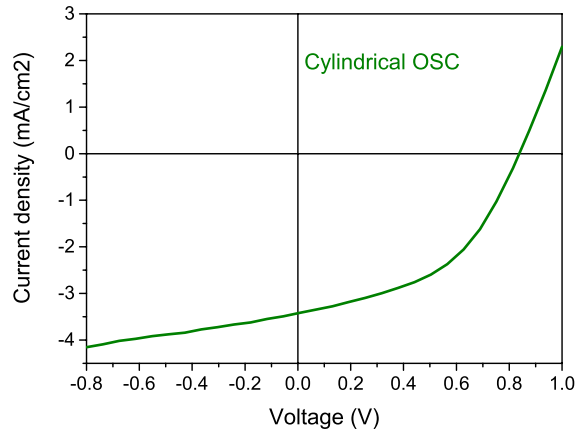
Figure 4.14. Measured current density as a function of voltage applied of an OSC deposited on a cylindrical substrate of 1 mm diameter. The cell architecture was an ITO layer as transparent electrode, a thin layer of NiO as electron blocking layer, P3HT:ICBA as active layer, a hole blocking layer of LiF and a metallic contact of Al.

Table 4.5. PV Performance details of the fabricated cylindrical organic solar cell.

Organic Solar Cell	J_{sc} (mA/cm^2)	V_{oc} (V)	FF (%)	PCE (%)
Cylindrical OSC	-3.426	837.727	46.74	1.34

4.3 Conclusions

Fabrication of organic cells in non-planar substrates requires that the deposition of all layers in the cell architecture is well adapted to the specific geometry of the substrate. In this chapter we introduced some modifications in the sputtering procedure to fabricate ITO electrodes on top of an array of fibers several microns in diameter. The adaptations introduced lead to highly homogenous layers of ITO with an optical transmission and an electrical performance very similar to the ones obtained when ITO is sputtered on a standard planar substrate.

In this chapter we combined the dip-coting procedure reported in Chapter 3 with ITO covered not-planar substrates. We fabricated and tested two different kinds of non-flat substrate cells, one deposited on an array of fibers 80 µm in diameter and another deposited on a single 1 mm diameter fiber. When comparing the performance of such two types of devices we concluded that the dip-coating technique is applicable over non-flat substrates, as long as the substrate does not exhibit any kind of micro-structuration. When the micro-structuration is present we could not obtain devices with a sufficiently good electrical performance. On the other hand, from the results of Chapter 2 an enhanced light harvesting can be achieved when such micro-structuration is present. In accordance, in the following chapter we will apply the ITO deposition procedure reported in here and explore an alternative method for the deposition of the active layer. The goal

is be to combine a micro-structuration to enhance light harvesting with an optimal electrical performance for the PV device.

5 Enhancement of light harvesting in OSC deposited on Fiber Arrays

In Chapter 2 we showed that an optical fiber array provides an excellent control of the light that is absorbed in the active layer leading to an enhancement of the short circuit current for organic cell devices. Such improvement in charge collection was described theoretically as coupling in the low Q WG type modes of the fibers when the fiber diameter was small. The study performed at such small fibers diameters close to 1.5 μm showed that the fiber array can lead to significant increase of the J_{sc} as the angle is increased, achieving as much as a 30% increase relative to the planar configuration at an incidence of 55 deg. When the diameter was taken to be larger than a few microns, numerical results indicated charge collection for light at normal incidence would increase in proportion to the increase in diameter.

In this chapter we will consider an experimental implementation of the type of fiber arrays solar cells that we studied theoretically in Chapter 2. For the fabrication of the fiber array we will use, standard commercially available fibers with a diameter 80 μm. Such size of fiber allows to study experimentally only the large end of the fiber dimensions considered in Chapter 2, but on the other hand, as it will be shown in section 5.2, it allows for the fabrication of macroscopic solar cells on fiber array with electrical properties that deviate little from similar cells fabricated on the standard flat substrate.

In Chapter 4 we explored the dip-coating technique for solution processed active layer applied to micro-structured non flat substrates and found that such technique leads to a rather non uniform coatings strongly affecting the electrical properties of the device[68-70,78,79]. In this chapter the evaporation of small molecules is explored for the deposition of the active layer. One of the most promising materials when using this technique is dibenzotetraphenylperiflanthene (DBP) provided it exhibits a high light absorption coefficient, long exciton diffusion lengths and large HOMO level[80-82].

In the current chapter we demonstrate the viability of fabrication of fiber arrays incorporating organic solar cells (FAOC). The photovoltaic response of the fabricated devices is measured with custom made setups and compared to a similar organic solar cell deposited on a planar substrate. Finally, the short circuit currents extracted from EQE measurements are evaluated as function of the light incidence.

5.1 Fabrication of fiber arrays

Our micro-structured substrates were composed of 80 μm diameter fibers. Such fibers are normally coated with a protection of dual acrylate that must be removed before forming the array. Once this protection is removed

with Tetrahydrofuran (THF), the fibers are sonically cleaned in a bath of acetone and then in methanol for about 10 min. Afterwards 15 fibers were positioned parallel to each other forming an aligned array similar to the one considered in section 4.2.2 of the previous chapter in a custom made setup, shown in Figure 5.1. This setup was composed of two Macor holders that had an aperture to hold exactly fifteen 80 μm fibers. Macor was used provided it can withstand the high temperatures required for the fusion of the fibers. To keep the fibers in place two clamps of Teflon that tighten them from their ends are used given that such soft material can hold the glass fibers without breaking them. A schematic view of such holding system is depicted in Figure 5.2a. These clamps are mounted on two motors that can move simultaneously with a slow velocity of v=0.004 mm/s, to pull out the fibers from their ends. A third motor is used to move a flame to heat the fibers at $1300^{o}C$. This motor provided an oscillatory movement for the flame of 13 mm in amplitude and 32.5 s in period. This setup allows to fuse the fibers while at the same time maintains the correct parallel fiber position for an adequate formation of the desired array. An optical microscopy image of a top view of a section of the final fiber array is shown in Figure 5.2b.
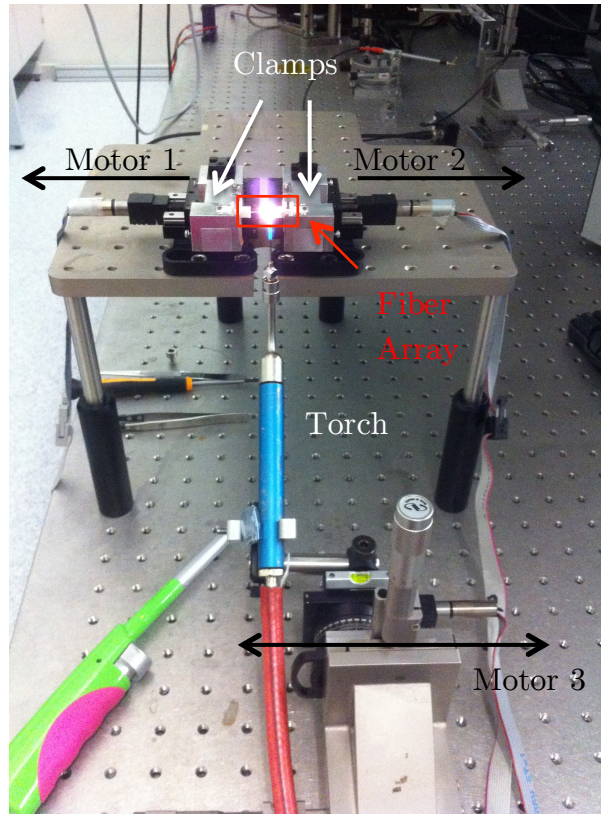
Figure 5.1. Setup for fabricating the fiber arrays. On motor 1 and motor 2 two clamps hold the aligned fibers from their ends. A third motor holds the torch which oscillates along the length of the separation between clamps to uniformly heat the array of fibers and melt them continuously.

Because of the stretching resulting from the heating and motor pulling, the final fiber diameter was reduced during the fusion process. Such final diameter can be determined assuming the fibers are perfect cylinders with a volume equal to

$$V = \pi r^2 h, \tag{5.1}$$

where r is the radius of the fiber and h is the length. If h_f is the final length of the fibers which can be accurately determined by keeping track of the total

displacement of the motors, under the assumption that the glass density does not change during the stretching and heating, we may establish that

$$\pi r^2 h = \pi r_f^2 h_f$$

where r_f is the final fiber diameter

$$r_f = \sqrt{\frac{r^2 h}{h_f}} \tag{5.2}$$

From the initial fiber dimensions we determined that after stretching the fiber diameter is reduced from 80 to 70μm, as can be seen in Figure 5.2b.

We can observe in Figure 5.2b that the fiber diameter is preserved along their length and the fibers are aligned with respect to their centers in the perpendicular direction because the distance between dark zones and bright zones, which correspond to crests and valleys, is the same along the image. Even though, the field of vision of this image is just 2 mm, moving with a micrometer the uniformity in the fiber diameter was preserved for about 5 mm.

a

b

770 μm
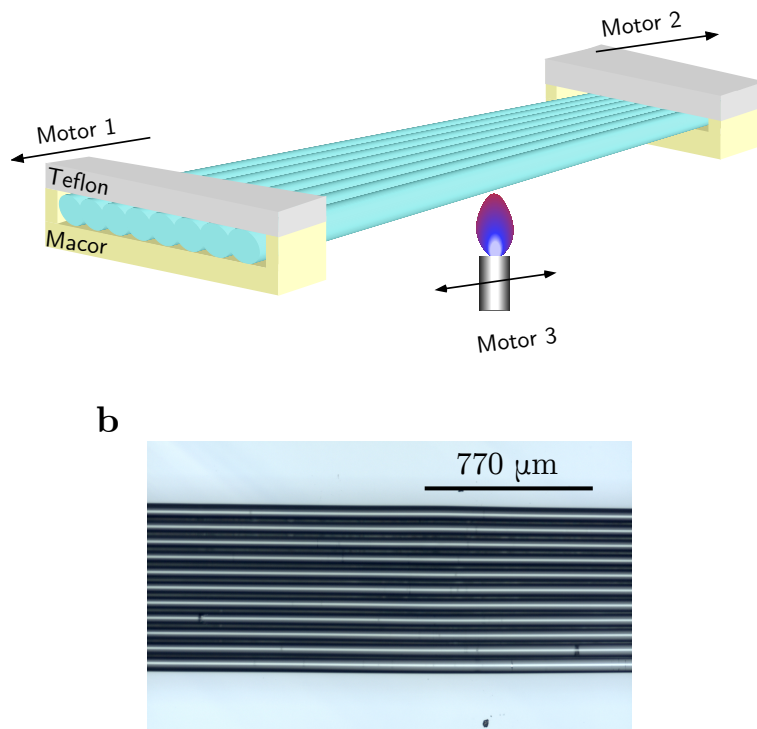
Figure 5.2. Schematics of fiber array substrates. a) Fibers are held from their ends with a clamp composed of two pieces, one made of Macor that supported the fibers and another one of Teflon that tightened them. y. b) Optical microscopy image of a top view of 11 fibers fused together using the setup shown in a) and **Figure 5.1**.

5.2 Organic solar cell deposition

Two different approaches have been proposed for avoiding the non-conformal deposition of the OSC in micro-structured substrates. One is to reduce the overfilling of the valleys by increasing the distance between peaks[69], the other is to change the deposition technique for the active layers to high vacuum deposition of small molecules. In that latter case the thickness of the vacuum deposited layers was seen to be more homogeneus[70].

High vacuum evaporation consists of heating a source material inside a vacuum chamber up to the point where it begins to boil and evaporate. Then, a substrate is placed inside the chamber to be covered with the source material. As this process takes place in vacuum, it allows molecules of the source material to evaporate freely in the chamber, and consequently condensate on the substrate. An illustrative image of such technique is depicted in Figure 5.3. Some of the advantages of this technique are high deposition rates of the films, a high purity, and a reduced surface damage provided the deposited particles have lower energy compared to, for instance, sputtering. However, the most relevant, for the type of configuration we consider in here, is a more directional coverage, which will lead, in principle, to more uniform coverage of crests and valleys.
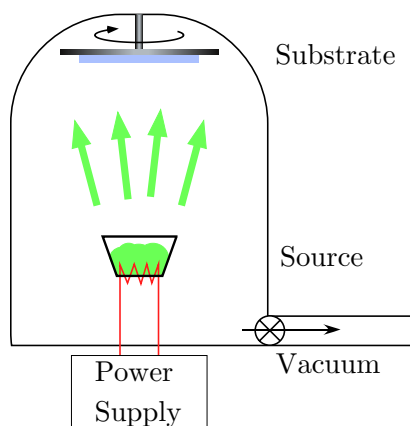
Figure 5.3. Schematics of the evaporation technique. It consists of a vacuum chamber where the source material is heated by Joule effect, i.e., a power supply heats a resistance that melts the source material. Once this material sublimates, it condensates in solid form on the substrate that for a more uniform coverage it may be rotated.

Once the substrates were fabricated and the ITO electrode deposited as explained in Chapter 4, one may begin with the deposition of the organic solar

cells using the evaporation based deposition technique. A schematic picture of the cell architecture used is shown in Figure 5.5a. Bilayer organic solar cells are fabricated on the back side of the fiber array. The transparent electrode was deposited at ICFO while the rest was fabricated at the Center for Research in NanoEngineering (CRNE) at UPC.

First the substrates were cleaned with methanol and dried in the oven at 120ºC for 5 min. Then, an ITO layer was deposited on the backside of the fiber array as explained in Chapter 4, followed by an annealing in the oven at 305ºC for 10 min to reach the desired resistance and transmission. After covering the backside of the fiber array with the transparent conducting oxide, an UVO treatment for 10 minutes was applied prior to transferring the samples to CRNE for depositing the subsequent layers. A small buffer layer of Molybdenum oxide (MoO3) of 8 nm was deposited in an evaporator integrated inside a glove box to be used as electron blocking layer. Then, we deposited the active layer by evaporation of small molecules. The donor material used was dibenzotetraphenylperiflanthene (DBP) and as acceptor material fullerene C_{70} was used. Both layers of 10 nm and 40 nm, respectively, were deposited in a vacuum chamber with base pressure of 10^{-7} mbar while substrate temperature was raised to 60ºC to promote the crystalline growth of DBP. Such temperature heating during the evaporation process enhances exciton diffusion, charge generation and collection efficiency in the donor/acceptor interface[83]. Then, a layer of bathocuproine (BCP) 8 nm thick was deposited as electron blocking layer. Finally, a 100 nm thick layer of Aluminum (Al) was deposited in another vacuum chamber that allowed substrate rotation for a more uniform coverage.

Once the devices were finished, they were transferred to ICFO in a sealed container filled with nitrogen at high pressure to minimize the degradation of the small molecule photovoltaic devices. Before measuring the photovoltaic performance, a mask on the front of the fiber array was deposited to delimit the illumination area during the experiments. Such mask was composed of a 50 nm layer of MoO_3 to prevent any short circuiting among the layers of the photovoltaic devices at the edges, and a 50 nm layer of Al to block light in the outer part of such mask.

A SEM image of the backside of the fiber array with all the layers of the OSC deposited is shown in Figure 5.4a, while in Figure 5.4b a schematics of what layer corresponds to each zone of the SEM image is seen. We also took a SEM image from the top view of the FAOC in order to determine the effective area of illumination for the FAOC, which is shown in Figure 5.4c, such window is represented schematically in Figure 5.4d.

a

b

c

d
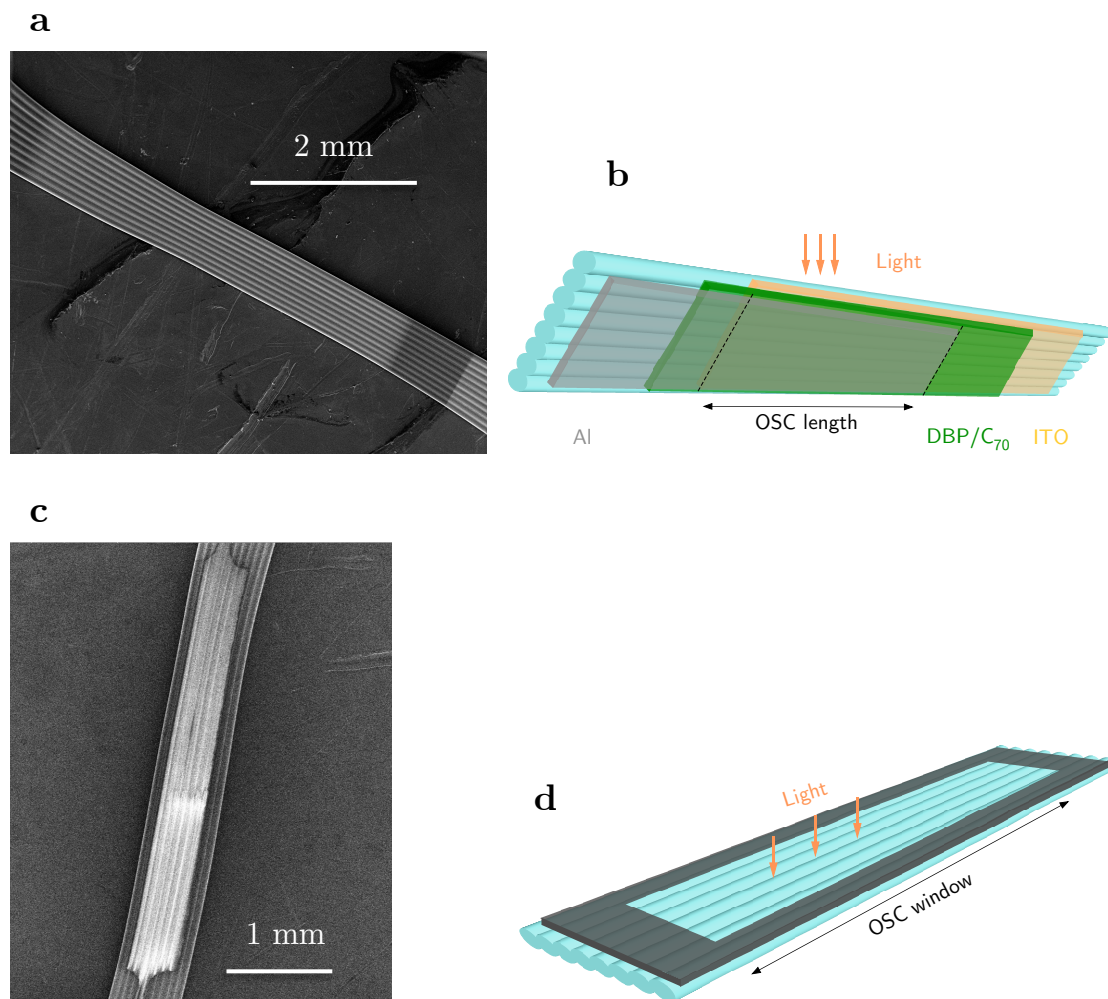
Figure 5.4. Images of the fiber array substrate containing an OSC. a) SEM image of the backside of the fiber array where the three main components of the organic solar cell can be seen. b) Schematic picture of the configuration of the layer deposition on fiber array substrates from their backside c) SEM image of the top view of a FAOC, the brighter zone corresponds to uncoated fibers that would serve as windows for light coupling. d) Window on the top side of the fiber array.

In order to visualize the thicknesses of the deposited layers, the cross section of the fabricated FAOC was imaged with a SEM (cf. Figure 5.5) after

measuring their photovoltaic performance. In Figure 5.5d we observe that with the evaporation technique the thickness and the conformation of the layer were maintained everywhere confirming the uniformity of all layers in the device. In all these images is possible to distinguish a layer of about 140 nm closer to the fiber array, which corresponds to ITO, and a brighter layer that corresponds to the 100 nm of Al layer. In between there is a darker zone corresponding to the active layer as a whole. The bilayer separation could not appreciate in the SEM images. The buffer layers could not be distinguished either because they were extremely thin.

a

Fiber
ITO
MoO$_3$
DBP
C$_{70}$
BCP
Al

b

1 µm

c

1 µm

d

1 µm

e

300 µm
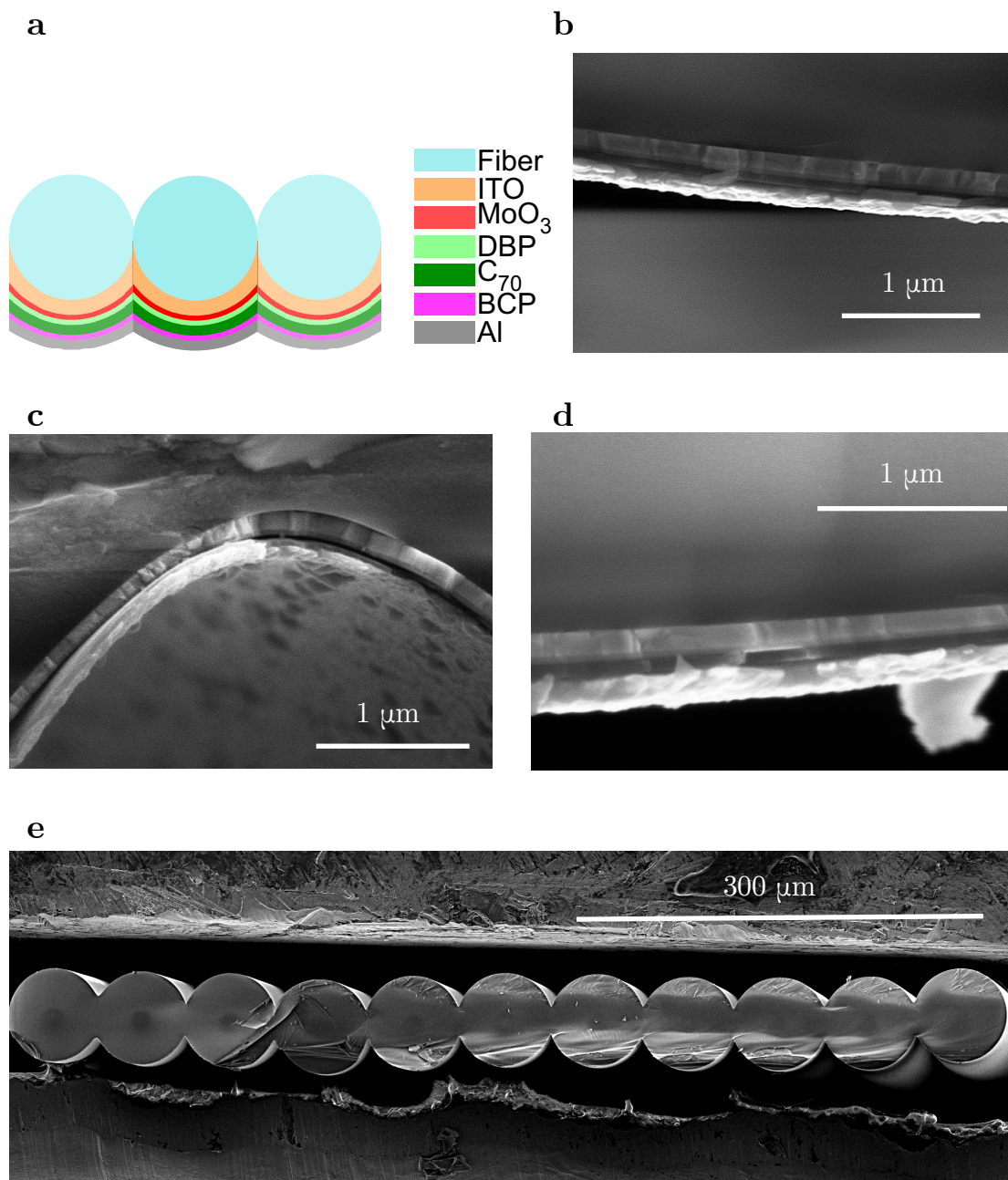
Figure 5.5. SEM images of the cross section of OSC deposited in a fiber array. a) Schematics of the architecture of OSC fabricated on the back side of fiber arrays. ITO was the transparent conducting oxide, MoO3 acts as electron blocking layer, then as active layer was deposited a bilayer composed of DBP as donor and C70 as acceptor, BCP was the hole blocking layer and finally the devices had Al as back contact. b) Zoom in the curvature of one fiber of the array containing an OSC, three zones are distinguishable: ITO, active layer, Al. c) Zone between two adjacent fibers, in here the same three layers are visible as in b) with the same thicknesses. d) Crest of one of the fibers of the array, these same three layers are seen. e) Array of aligned fibers fabricated and coated on its backside with the OSC as shown in a).

5.3 Photovoltaic performance of Fiber Arrays containing Organic Solar Cells

Planar substrates were also fabricated with the procedure described in the previous section. It was found that OSC fabricated with small molecules in the active layer have a large variability in their performance. In accordance, to extract reliable information on the relative performance when comparing different kind of cells a statistical analysis had to be performed.

We measured the JV curves from a single batch 32 planar OSC that we used as reference cells. A histogram of their fill factor is shown in Figure 5.6a, where we observe that the most probable value was in between 50 and 60%. One may assume that cells in between that range may have similar electronic characteristics, irrespective of their optical behavior. If we take the 11 cells which exhibited a FF in between that range and we plot again a histogram of their short circuit current density, we can estimate which would be the most probable J_{sc}, shown in Figure 5.6b for such limited subset of cells. Averaging the J_{sc} of such 6 cells we obtained a mean $J_{sc}=3.789\text{mA/cm}^2$; thus a cell from such group of 6 that more, which J_{sc} is closest to this value can be used as the reference cell for comparison with the cells deposited on the fiber array.

a

b
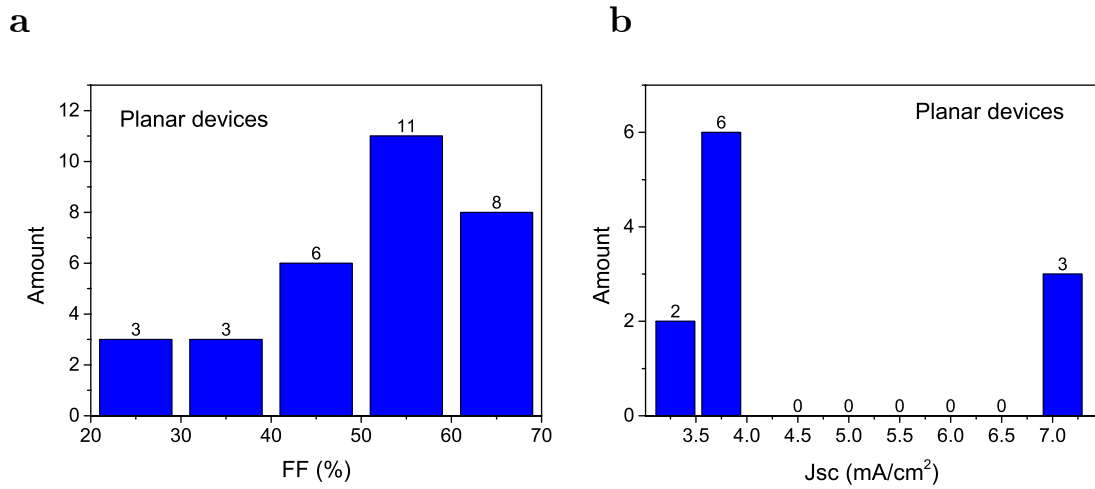
Figure 5.6. Statistical analysis of planar devices. a) Histogram of the FF measured on the planar cells, the most probable value for the FF is between 50 and 60%. b) Histogram of the short circuit current density of the cells that have the same fill factor shown in a), most of these OSC have a J_{sc} between 3.5 and 4 mA/cm^2.

As for planar OSC, devices fabricated on the backside of fiber arrays exhibited a similar variability. Hence, ten cells were fabricated and tested with the probes shown in Figure 5.7. To measure their performance such cells were positioned in a custom made holder with an aperture for illuminating the devices, as seen in Figure 5.7a. Two probes driven by micrometric positioners contacted the OSC from the backside to extract charges, as can be seen in Figure 5.7b.
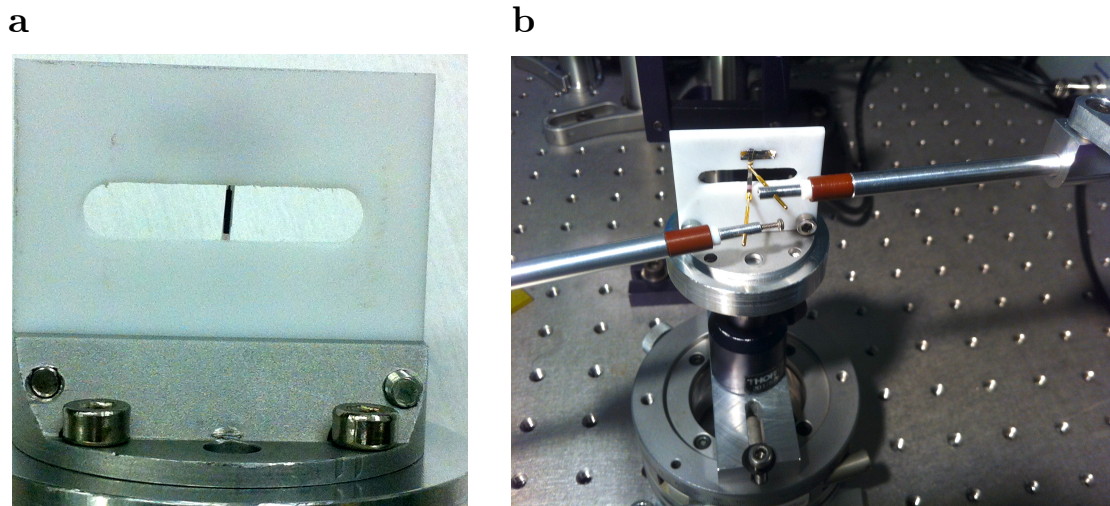
Figure 5.7. a) Aperture of the holder to illuminate fiber array devices from the light window shown in **Figure 5.4**d. b) Probes contacting the fiber array device to extract the charges from the electrodes.

Due to uncontrollable defects that appear in one out of four times in the fabrication of the fiber array, from the ten fabricated cells only seven worked. With these cells we applied the same statistics as for the planar ones. A histogram of their fill factor is shown in Figure 5.8a. From these five cells that have similar FF indicating similar electrical properties were selected and, another histogram of the short circuit current density was obtained as shown in Figure 5.8b. We dismissed the best and the worst and we averaged the J_{sc} of the rest, then we took the cell for comparison with the planar reference the one which had a J_{sc} that more resembled to the mean J_{sc}=4.196 mA/cm2.
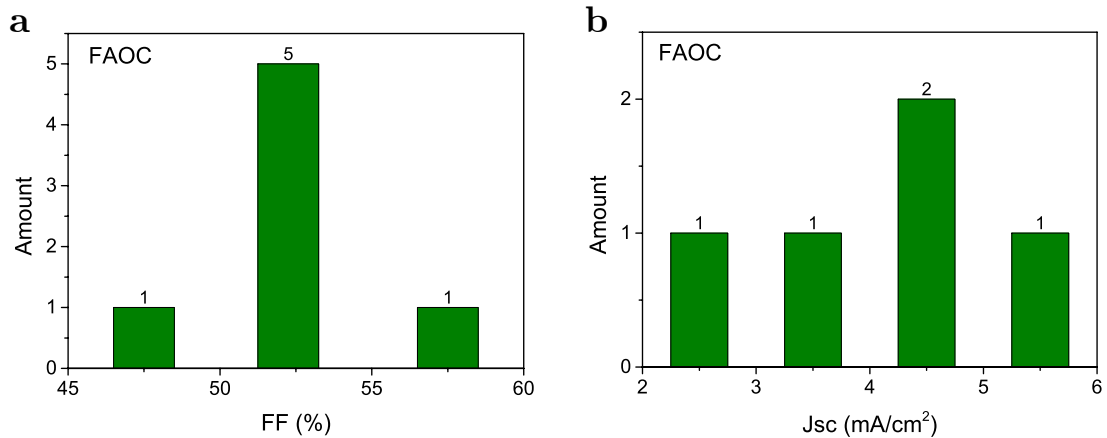
Figure 5.8. Statistical analysis for the fiber array cells. a) Histogram of the measured FF, b) Histogram of short circuit current of the five cells that had exhibited the most probable FF.

In Figure 5.9 the JV curves of such most probable devices fabricated on planar (red solid line) or fiber array (green solid line) substrates are compared. We observe that both devices cross the x-axis in almost the same point, which means that their V_{oc} is very similar. More interestingly is that the short circuit current density obtained with the fiber array cell lies below the one for the planar cell, indicating a larger capacity to collect charges.
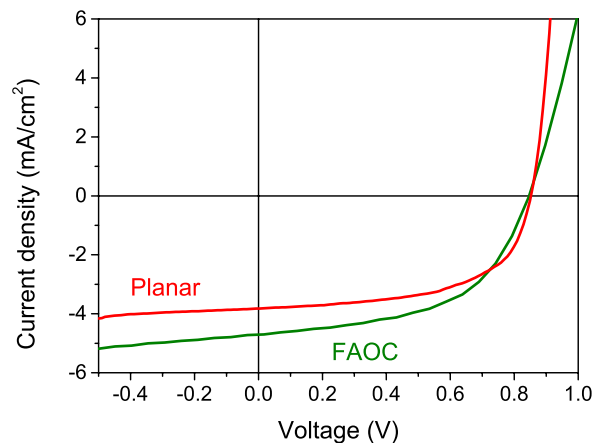
Figure 5.9. Current density vs. voltage curves of OSCs deposited in planar (red solid line) and fiber array substrates (green solid line).

The photovoltaic parameters of both cells are given in Table 5.1. Note the enhancement of the J_{sc} in the fiber array devices has a direct effect of an improved power conversion efficiency.

Table 5.1. Performance details of fabricated planar and fiber array solar cells.

Substrate	J_{sc} (mA/cm^2)	V_{oc} (mV)	FF (%)	PCE (%)
Planar	-3.821	852.134	58.14	1.89
FAOC	-4.711	846.250	53.51	2.13

The difference in light management and performance in between the planar reference and the fiber array cells can be made more apparent by measuring the EQE. Such EQE was obtained using the custom made setup shown in Figure 5.10. A source of light was coupled to a monochromator, while a chopper modulated the light signal that was incident on the device. Charges were collected using the same probes depicted in Figure 5.7 at each illumination wavelength with a lock-in amplifier to eliminate most of the background electrical noise. The monochromator and the lock-in were controlled with a computer using a custom-made LabView program that collected and stored the measured currents. Such system was calibrated before each experiment with a factory calibrated Hamamatsu photodiode
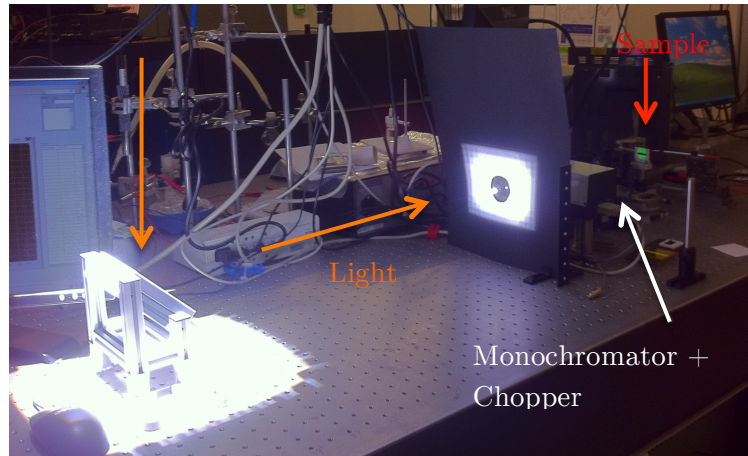
Figure 5.10. Experimental setup for EQE measurements. The light source is a solar simulator with AM1.5G that is reflected with a mirror and coupled into a monochromator with a lens. After the monochromator there is a chopper to modulate the light incident on the sample. Photogenerated charges are collected at each illumination angle with a lock-in to remove any electrical noise.

As seen in Eq 1.1 from Chapter 1, the EQE is a function of the absorption efficiency that depends on the incident wavelengths and other wavelength independent parameters directly linked to the charge collection capacity of the device once the photon has been absorbed. Using the calibrated photodiode we can extract the photon flux and the optical set-up transmission, which are independent of the device measured. In accordance, we can relate the current of the calibrated photodiode with its calibrated cell EQE and we may extract the EQE of our devices using the following expression:

$$EQE_{Meas} = \frac{I_{Meas}}{I_{Cal}} EQE_{Cal} \frac{A_{Cal}}{A_{Meas}} \tag{5.3}$$

The measured EQE from our planar OSC and fiber array cells are shown in Figure 5.11a. We observe that between 500nm and 650nm the

FAOC response lies above the planar OSC, which explains the enhancement in charge collection seen in Figure 5.9 and Table 5.1 when using fiber arrays as substrates. From these curves we can extract again the short circuit current integrating the response of the devices over all wavelengths and weight them with the AM1.5G photon flux . The extracted values were J_{sc}=3.368 mA/cm^2 for the planar and a J_{sc}=4.255 mA/cm^2, which corresponds to an enhancement of the photocurrent generated of 26.35%. This percentage improvement is similar to the one obtained when such percentage is determined directly from the JV curve.

a
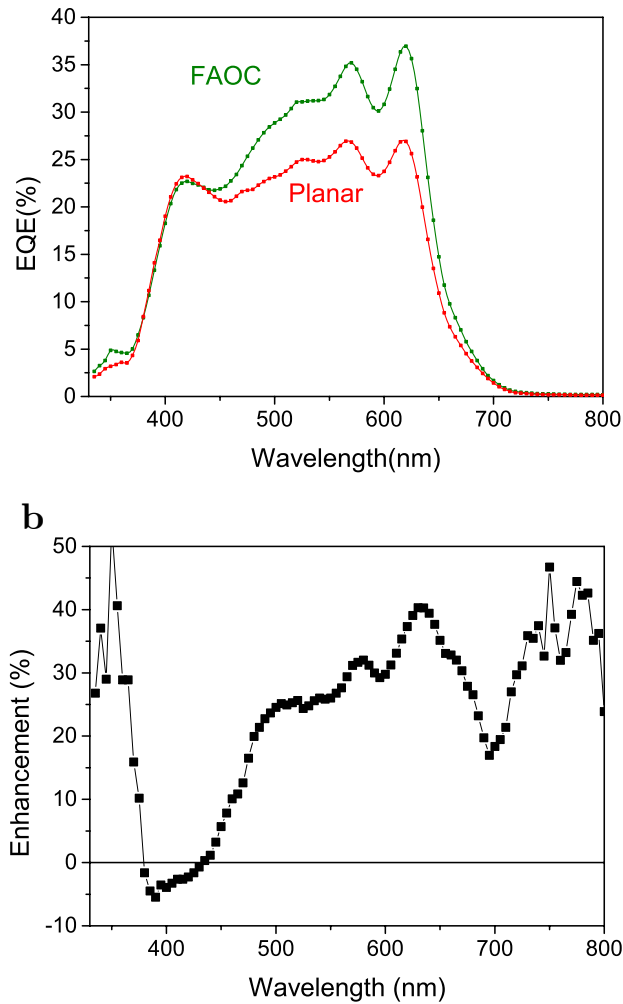
Figure 5.11. a) EQE from the most probable OSC in a planar substrate (red dotted squares) and the one from the fiber array substrate (green dotted squares). Lines are only a guide for the eye. b) Percentage EQE enhancement as a function of the wavelength..

In Figure 5.11b we computed the enhancement on the EQE obtained form the fiber array cell compared to the planar cell as a function of the wavelength using equation 5.2. As can be seen in this figure, such enhancement is strongly dependent on the wavelength. In the 500-650 nm range this enhancement is between 20 and 40%.

$$Enhancement(\lambda) = \frac{EQE^{Meas}(\lambda) - EQE^{Planar}(\lambda)}{EQE^{Planar}(\lambda)} \cdot 100 \qquad (5.2)$$

With the custom made setup shown in Figure 5.10, we also measured the EQE at different angles of incidence. Note that the window deposited on the front side of the fiber array (Figure 5.4c and 4d) prevented light entering the device form the edges. From the EQE measurements and using again Eq. 1.2 from Chapter 1, we computed the short circuit current density shown in Figure 5.12 as a function of the angle of incidence. We observe that at zero incidence we have the largest improvement that decreases as we increase the angle of incidence up to approximately 50 deg. From there the efficiency partially recovers the improvement up to 70 deg where we stopped the measurements provided the effective area beyond this angle is very small and the results obtained become unreliable.
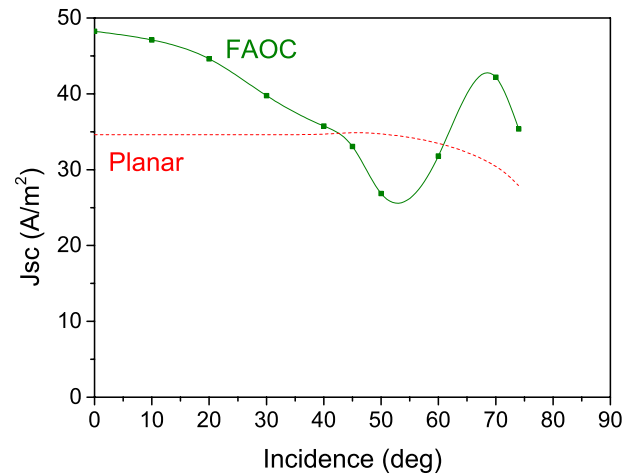
Figure 5.12. Short circuit current density extracted from the measured EQE at different illumination angles for the fiber array cells (square green dots, lines are only a guide for the eye). The planar response (red dashed line) was only measured at 0 deg and its dependence in angle its extracted from the theory developed in Chapter 2.

5.4 Discussion

From the analysis of the experimental results reported in the previous section we may conclude that the fiber array provides the capacity to manage light better and increase charge collection for extremely thin cells. This capacity is best when the light is incident at normal incidence. This would be in partial agreement with the results from Chapter 2 which indicated that as the diameter of the fiber is increased to tens of microns, photon absorption when photons are incident normally increases, too. However, from the same discussion in Chapter 2, we noted that light management achieved for large diameter fibers can not be explained by light coupling in the WGM. A careful look into Figure 2.9b indicates that the fiber array provides a larger capacity for light trapping inside the substrate, which is, then, more effectively absorbed by the active material. Note that the total amount of such material is larger for the fiber array cell relative to the planar cell when comparing same size devices.

The remarkable capacity of the fiber array substrate to improve light management is confirmed when comparing the EQE of any fiber device with the EQE of any planar cell. A strong wavelength dependence is seen which clearly indicates that any improvement in performance is dominated by an optical effect rather than an electrical effect linked to a different nano-morphology with better capacity for charge collection.

On the contrary, in the 500-650 nm wavelength range, almost no wavelength dependence is seen when we compare for instance different planar cells exhibiting a quite different overall PV performance. In Figure 5.13 we show the enhancement (or worsening) percentage of the best and the worst planar devices with the one that form the statistical analysis we concluded it exhibited the most probable performance. For the planar cases, in a large wavelength range, the percentage change exhibits an almost flat response. Larger changes are seen for all cells beyond 650 nm, but these are less significant given the low photon absorption capacity of the active material beyond this point.
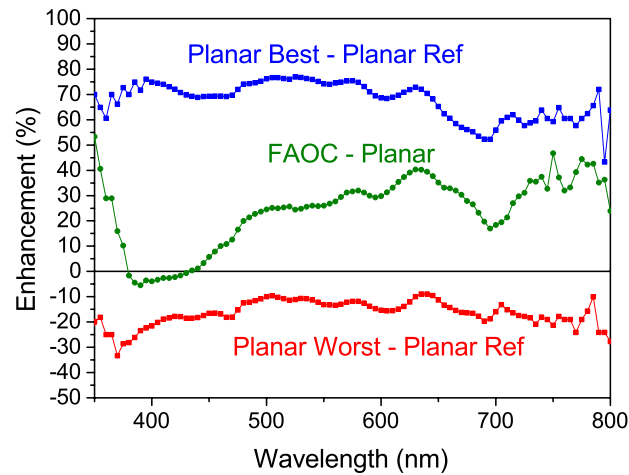
Figure 5.13. Percentage EQE enhancement obtained with the best planar cell (blue square dots), the fiber array cell (green circle dots) and the worst planar cell (red square dots). The cell used as reference in all three cases is the planar one that we determined from the statistical analysis as the one exhibiting the most probable performance.

The large dispersion seen in the performance of the planar devices (cf. Figure 5.6 and Figure 5.8) must be linked to some uncontrollable parameters during the fabrication process that have a strong effect on the final capacity for the device to collect charges.

5.5 Conclusions

In this chapter we demonstrated that fabrication of an organic solar cell on top of non-planar substrate formed by an array of fibers is feasible when the evaporation technique is used for the deposition of the active material. We have shown that the electrical performance of such cells is similar to their planar counterpart but the fiber array cells exhibit a significantly better capacity to manage light leading to an enhanced photon absorption in between 20 and 30 %. Such an enhancement provided by the fiber array configuration is very high when compared to other optical approaches which have been tested in the past to improve light harvesting capacity in thin film solar cells.

The improvement seen in charge collection is in agreement with the results from Chapter 2 when large diameter fibers are considered. However, further theoretical developments are needed to fully understand the nature of the light trapping and enhanced absorption provided by the fiber array. The experimental results obtained clearly demonstrate that light absorption is enhanced when a fiber array substrate is used but they are not sufficient in helping to design a fiber array configuration where the parameters are such

that light absorption becomes optimal. In other words, we believe that there is still room to improve the performance of such fiber array cells if relevant parameters in an optical PV control, such as index of refraction or dimensions, are further adjusted. This may, eventually, lead to a cell configuration were the amount of active material used is minimal. The use of small quantities of material may become rather relevant in applications such as, for instance, in semi-transparent solar modules or in electronic devices incorporating solar based power sources.

6 | Conclusions

In this thesis we examined the enhancements on light harvesting of an organic solar cell deposited on the backside of a fiber array. From the numerical study developed in Chapter 2, we concluded that light absorption depended on the size of the fibers. For small diameter fibers, a light coupling in the WGM explained the enhancements on the absorption. Whereas in large diameter fibers, light trapping in the fiber array may produce such enhancements. Such trapping promoted the absorption in the perimeter containing an OSC.

To experimentally implement an OSC on the backside of a fiber array, in Chapter 3 a technique for depositing solution-processed layers regardless of substrate form was explored. Such technique is the dip-coating procedure and both bilayer and bulk heterojunction were fabricated. As they performed similarly to the cells fabricated using the traditional spin coating, we demonstrated the viability of such technique for depositing active layers. In addition, we monitored the degradation of several substrates coated from the same solution and no decrease in the photovoltaic performance was observed. This opens a way to implement such technique for continuous mode fabrication.

The deposition of the layers on non-flat substrates was further examined in Chapter 4. We introduced some modifications in the sputtering

procedure to fabricate the ITO transparent electrode so as to achieve an optimal quality both optically and electrically. Combining the dip coating procedure explained in Chapter 3 with the transparent electrodes deposited in non-flat structures, we fabricated and tested two kinds of curved substrates to deposit OSC. Although dip coating technique can be applied to fabricate OSC in single fibers, when a micro-structuration was present it led to devices with not enough good electrical performance. As the aim was to combine the micro-structuration to enhance light harvesting with an optimal performance of OSC, the evaporation of the active layer was explored in Chapter 5.

Finally, in the last chapter we demonstrated that the OSC on the backside of a fiber array had an electrical performance similar to their planar counterpart. We fabricated the substrate using 80 μm optical fibers, and we observed that the OSC deposited in such fiber array exhibited an enhanced photon collection between 20% and 30%. In conclusion, the improvement in light harvesting with the proposed configuration is very high when compared to other optical approaches. In addition, the results are in accordance with the theoretical model studied.

A Appendix: nk coefficients

Indium Tin Oxide (ITO)

Figure A.1

ITO
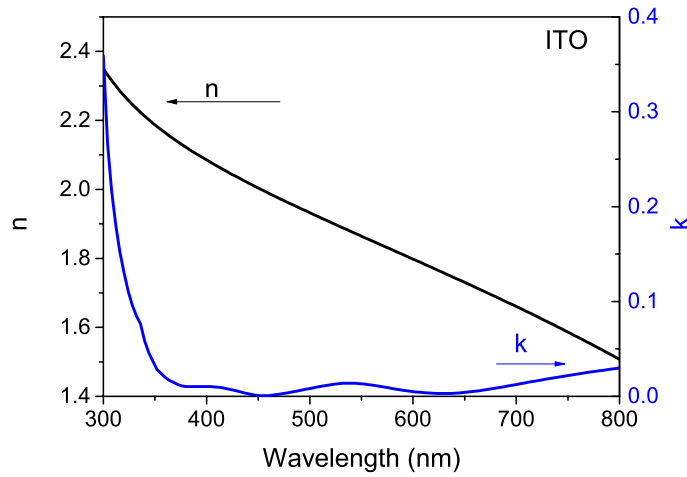
WL(nm)	n	k
300	2.3494	0.3591
304	2.3321	0.2662
308	2.3156	0.217
312	2.3002	0.1802
316	2.2856	0.1527
320	2.2718	0.1303
324	2.2587	0.1108
328	2.2462	0.0961
332	2.2345	0.0848
336	2.2232	0.0765
340	2.2123	0.0582
344	2.202	0.0456
348	2.192	0.0369
352	2.1823	0.0282
356	2.1729	0.024
360	2.164	0.0198
364	2.1552	0.0168
368	2.1466	0.0147
372	2.1383	0.0125
376	2.1302	0.0111
380	2.1223	0.0104

384	2.1146	0.0102	496	1.9378	0.0074
388	2.107	0.0102	500	1.9322	0.0083
392	2.0996	0.0102	504	1.9267	0.0091
396	2.0924	0.0102	508	1.9212	0.01
400	2.0852	0.0102	512	1.9157	0.0107
404	2.0782	0.0102	516	1.9102	0.0115
408	2.0712	0.0099	520	1.9048	0.0122
412	2.0644	0.0095	524	1.8994	0.0129
416	2.0577	0.0089	528	1.894	0.0134
420	2.0511	0.008	532	1.8885	0.0137
424	2.0446	0.007	536	1.8832	0.0139
428	2.0382	0.006	540	1.8779	0.0138
432	2.0318	0.0049	544	1.8724	0.0137
436	2.0256	0.0038	548	1.8671	0.0134
440	2.0194	0.0028	552	1.8618	0.013
444	2.0132	0.0019	556	1.8564	0.0125
448	2.0071	0.0012	560	1.8511	0.0119
452	2.0011	7.00E-04	564	1.8458	0.0113
456	1.9951	6.00E-04	568	1.8405	0.0106
460	1.9892	8.00E-04	572	1.8352	0.0098
464	1.9833	0.0013	576	1.8298	0.0091
468	1.9775	0.0019	580	1.8245	0.0083
472	1.9717	0.0025	584	1.8192	0.0076
476	1.966	0.0032	588	1.8139	0.0069
480	1.9602	0.004	592	1.8086	0.0062
484	1.9546	0.0048	596	1.8032	0.0056
488	1.949	0.0057	600	1.7979	0.005
492	1.9433	0.0065	604	1.7926	0.0045

608	1.7872	0.0041	720	1.6314	0.0164
612	1.7818	0.0037	724	1.6255	0.0172
616	1.7764	0.0034	728	1.6196	0.018
620	1.7711	0.0032	732	1.6136	0.0187
624	1.7657	0.003	736	1.6077	0.0195
628	1.7603	0.003	740	1.6017	0.0202
632	1.7549	0.003	744	1.5956	0.0209
636	1.7495	0.0031	748	1.5895	0.0216
640	1.744	0.0033	752	1.5834	0.0223
644	1.7386	0.0036	756	1.5773	0.023
648	1.7332	0.004	760	1.5711	0.0237
652	1.7277	0.0044	764	1.5648	0.0244
656	1.7222	0.0048	768	1.5586	0.025
660	1.7166	0.0054	772	1.5523	0.0257
664	1.7111	0.0059	776	1.546	0.0263
668	1.7056	0.0065	780	1.5397	0.0269
672	1.7	0.0072	784	1.5333	0.0275
676	1.6944	0.0079	788	1.5268	0.0281
680	1.6888	0.0086	792	1.5203	0.0287
684	1.6832	0.0094	796	1.5138	0.0293
688	1.6776	0.0101	800	1.5072	0.0299
692	1.6719	0.0109			
696	1.6662	0.0117			
700	1.6604	0.0125			
704	1.6547	0.0133			
708	1.6489	0.0141			
712	1.6431	0.0149			
716	1.6373	0.0157			

Poly(3-hexyltiophene): Indene-C60 bisadduct (P3HT:ICBA)
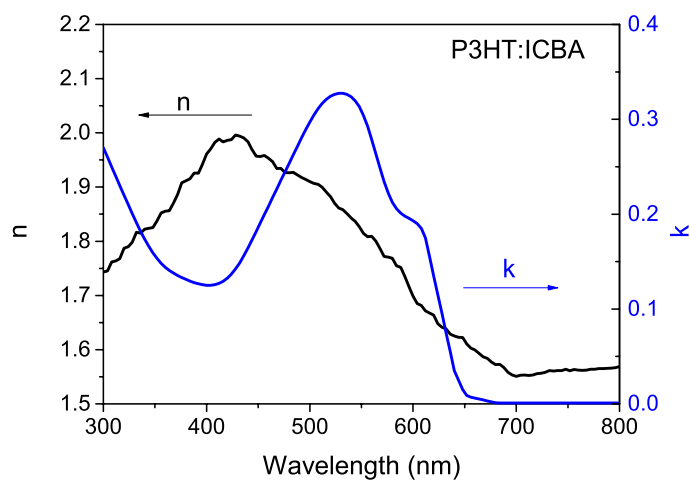
Figure A.2

WL(nm)	n	k		WL(nm)	n	k
	P3HT:ICBA			356	1.85245	0.1482
				360	1.85571	0.144
300	1.74314	0.27		364	1.85639	0.1406
304	1.74555	0.26		368	1.87059	0.1378
308	1.76163	0.25		372	1.88724	0.1353
312	1.76359	0.24		376	1.908	0.1332
316	1.76767	0.23		380	1.91151	0.1312
320	1.78698	0.2201		384	1.91535	0.1294
324	1.79004	0.2102		388	1.92614	0.1278
328	1.79816	0.2005		392	1.92559	0.1266
332	1.81673	0.1911		396	1.9419	0.1256
336	1.81506	0.1821		400	1.96106	0.1251
340	1.82241	0.1736		404	1.97024	0.1251
344	1.82396	0.1659		408	1.98239	0.1257
348	1.82508	0.1591		412	1.98857	0.127
352	1.83798	0.1532		416	1.98347	0.1291

420	1.98633	0.1324	532	1.85857	0.3274
424	1.98735	0.1368	536	1.85102	0.3263
428	1.99612	0.1422	540	1.84286	0.3238
432	1.99408	0.1487	544	1.83653	0.3196
436	1.99061	0.1561	548	1.82633	0.3131
440	1.98388	0.1642	552	1.81449	0.3041
444	1.96939	0.1727	556	1.80837	0.2925
448	1.95694	0.1816	560	1.80939	0.2787
452	1.95612	0.1906	564	1.8002	0.2636
456	1.95816	0.1996	568	1.78633	0.2483
460	1.95286	0.2086	572	1.77204	0.2342
464	1.94673	0.2176	576	1.77082	0.2221
468	1.93429	0.2266	580	1.76878	0.2126
472	1.93469	0.2356	584	1.75469	0.2057
476	1.92673	0.2446	588	1.75204	0.201
480	1.92653	0.2536	592	1.73551	0.1979
484	1.92714	0.2626	596	1.71612	0.1956
488	1.92224	0.2716	600	1.69912	0.1932
492	1.91796	0.2804	604	1.68512	0.19
496	1.91429	0.289	608	1.68135	0.185
500	1.91	0.2972	612	1.6718	0.175
504	1.90653	0.3046	616	1.66753	0.155
508	1.9051	0.3112	620	1.66365	0.135
512	1.8998	0.3167	624	1.64802	0.115
516	1.89061	0.3211	628	1.64114	0.095
520	1.88204	0.3243	632	1.63851	0.075
524	1.87041	0.3263	636	1.62857	0.055
528	1.86143	0.3274	640	1.62545	0.035

644	1.62282	0.025		756	1.56337	1.00E-03
648	1.62261	0.015		760	1.56218	1.00E-03
652	1.61057	0.009		764	1.56186	1.00E-03
656	1.60298	0.0071		768	1.56243	1.00E-03
660	1.59939	0.0061		772	1.56378	1.00E-03
664	1.59308	0.0051		776	1.56378	1.00E-03
668	1.58684	0.0041		780	1.56504	1.00E-03
672	1.58402	0.0031		784	1.56508	1.00E-03
676	1.5769	0.0021		788	1.56541	1.00E-03
680	1.57265	0.0011		792	1.56582	1.00E-03
684	1.57298	1.00E-03		796	1.56694	1.00E-03
688	1.56724	1.00E-03		800	1.56865	1.00E-03
692	1.55827	1.00E-03				
696	1.55341	1.00E-03				
700	1.55067	1.00E-03				
704	1.55284	1.00E-03				
708	1.55316	1.00E-03				
712	1.55259	1.00E-03				
716	1.55329	1.00E-03				
720	1.5559	1.00E-03				
724	1.55667	1.00E-03				
728	1.55814	1.00E-03				
732	1.56129	1.00E-03				
736	1.56063	1.00E-03				
740	1.56141	1.00E-03				
744	1.56133	1.00E-03				
748	1.56386	1.00E-03				
752	1.56116	1.00E-03				

Dibenzotetraphenylperiflanthene/C70 (DBP/C70)
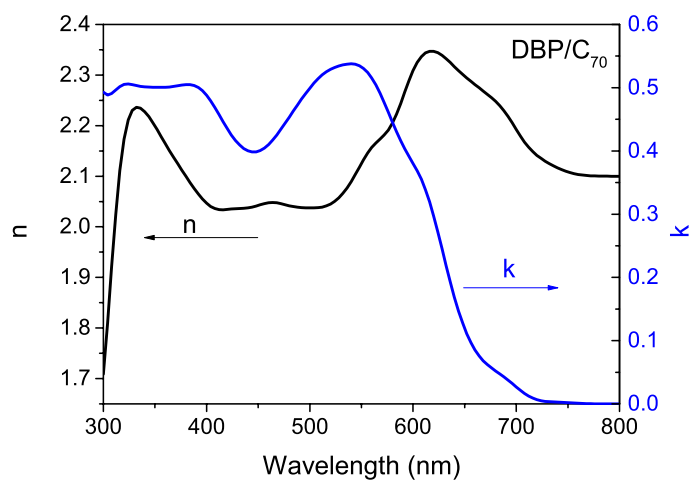
Figure A.3

WL(nm)	n	k		WL(nm)	n	k
	DBP/C70			356	2.17833	0.50055
				360	2.16427	0.50069
300	1.70884	0.49309		364	2.15065	0.50116
304	1.80936	0.48825		368	2.13751	0.50198
308	1.92087	0.4909		372	2.12471	0.50309
312	2.02534	0.4965		376	2.1122	0.50424
316	2.1113	0.50187		380	2.09985	0.50502
320	2.17327	0.50514		384	2.08765	0.50498
324	2.21124	0.5058		388	2.07585	0.50359
328	2.23017	0.50477		392	2.06481	0.50045
332	2.23641	0.50329		396	2.05488	0.4953
336	2.23455	0.50202		400	2.04654	0.48811
340	2.22769	0.50122		404	2.04024	0.47912
344	2.21776	0.50087		408	2.0361	0.46876
348	2.20577	0.50072		412	2.03402	0.4576
352	2.19239	0.5006		416	2.03361	0.44626

420	2.03424	0.43531	532	2.06602	0.53613
424	2.03515	0.42525	536	2.07659	0.53732
428	2.03591	0.41648	540	2.08912	0.53773
432	2.03639	0.40927	544	2.10321	0.53702
436	2.03682	0.4038	548	2.118	0.53478
440	2.03752	0.40017	552	2.13251	0.5306
444	2.03891	0.39845	556	2.14577	0.52414
448	2.04104	0.39864	560	2.15685	0.51535
452	2.04361	0.40071	564	2.16571	0.50433
456	2.04599	0.40458	568	2.17334	0.49133
460	2.04767	0.41011	572	2.18131	0.47681
464	2.04817	0.41708	576	2.19127	0.46139
468	2.04743	0.42521	580	2.20486	0.4457
472	2.04575	0.43418	584	2.22267	0.43042
476	2.04364	0.44366	588	2.24381	0.41619
480	2.04159	0.45338	592	2.26658	0.40329
484	2.03997	0.4631	596	2.289	0.39154
488	2.03887	0.47267	600	2.30893	0.38032
492	2.03816	0.48199	604	2.32488	0.36861
496	2.03768	0.49095	608	2.33643	0.35517
500	2.0374	0.49941	612	2.34372	0.33896
504	2.03736	0.50722	616	2.34703	0.3195
508	2.03776	0.51419	620	2.34698	0.29688
512	2.03901	0.52018	624	2.34423	0.27176
516	2.04143	0.52509	628	2.3392	0.24525
520	2.04513	0.52901	632	2.33244	0.21859
524	2.05033	0.53205	636	2.32476	0.1928
528	2.05728	0.53438	640	2.31677	0.16873

644	2.30889	0.14692	756	2.10512	0.00147
648	2.30143	0.12766	760	2.10353	0.00108
652	2.29445	0.11101	764	2.10234	7.31E-04
656	2.28774	0.09696	768	2.10148	4.57E-04
660	2.28118	0.08534	772	2.10089	2.59E-04
664	2.27474	0.07588	776	2.1005	1.33E-04
668	2.26837	0.06824	780	2.10026	6.04E-05
672	2.26195	0.06204	784	2.10012	2.36E-05
676	2.25529	0.0568	788	2.10005	7.65E-06
680	2.24798	0.05208	792	2.10002	2.14E-06
684	2.23955	0.0475	796	2.1	4.80E-07
688	2.22964	0.04273	800	2.1	6.40E-08
692	2.2182	0.03762			
696	2.20555	0.0322			
700	2.19237	0.02666			
704	2.17946	0.02128			
708	2.16756	0.01639			
712	2.15721	0.01225			
716	2.14851	0.00899			
720	2.14127	0.00661			
724	2.13517	0.00502			
728	2.12984	0.00403			
732	2.12501	0.00344			
736	2.12056	0.00309			
740	2.1165	0.00283			
744	2.11288	0.00256			
748	2.10976	0.00224			
752	2.10718	0.00187			

Aluminum (Al)

Figure A.4

Al
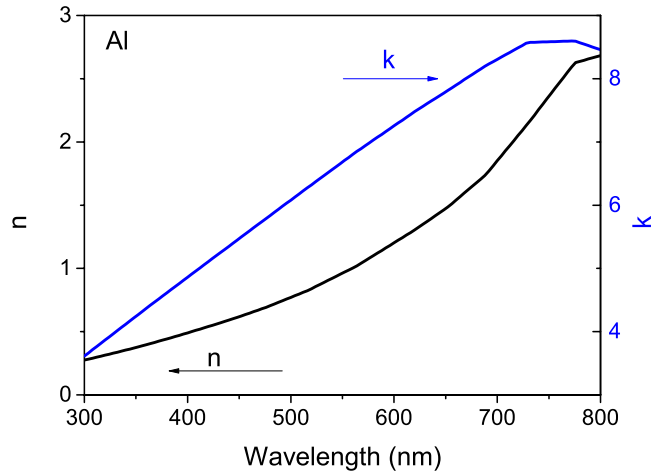
WL(nm)	n	k
300	0.27571	3.61265
304	0.28303	3.66359
308	0.29034	3.71453
312	0.29792	3.76525
316	0.30577	3.81575
320	0.31361	3.86626
324	0.32146	3.91676
328	0.32944	3.96718
332	0.3376	4.01749
336	0.34577	4.0678
340	0.35393	4.1181
344	0.36209	4.16841
348	0.37072	4.21822
352	0.37941	4.26797
356	0.38809	4.31772
360	0.39678	4.36747
364	0.40547	4.41722
368	0.41466	4.46675
372	0.42396	4.51624
376	0.43326	4.56573
380	0.44256	4.61521
384	0.45186	4.6647
388	0.46122	4.71412
392	0.47097	4.76305
396	0.48073	4.81197
400	0.49048	4.8609
404	0.50024	4.90983

408	0.50999	4.95876	520	0.83963	6.32295
412	0.51975	5.00769	524	0.85598	6.3709
416	0.52977	5.05661	528	0.87233	6.41885
420	0.53994	5.10552	532	0.88868	6.46679
424	0.5501	5.15443	536	0.90503	6.51474
428	0.56026	5.20334	540	0.92138	6.56268
432	0.57042	5.25225	544	0.93773	6.61063
436	0.58058	5.30115	548	0.95408	6.65858
440	0.59074	5.35006	552	0.97043	6.70652
444	0.60125	5.39892	556	0.98678	6.75447
448	0.61264	5.44765	560	1.00314	6.80241
452	0.62403	5.49638	564	1.01985	6.85008
456	0.63542	5.54511	568	1.04014	6.89501
460	0.64681	5.59384	572	1.06044	6.93993
464	0.6582	5.64257	576	1.08074	6.98485
468	0.66959	5.6913	580	1.10103	7.02977
472	0.68098	5.74003	584	1.12133	7.0747
476	0.69237	5.78875	588	1.14163	7.11962
480	0.70514	5.83739	592	1.16192	7.16454
484	0.71833	5.88601	596	1.18222	7.20946
488	0.73151	5.93462	600	1.20252	7.25439
492	0.7447	5.98323	604	1.22281	7.29931
496	0.75788	6.03184	608	1.24311	7.34423
500	0.77106	6.08045	612	1.26341	7.38915
504	0.78425	6.12906	616	1.2837	7.43408
508	0.79743	6.17767	620	1.304	7.479
512	0.81062	6.22629	624	1.32655	7.52092
516	0.8238	6.2749	628	1.34911	7.56285

632	1.37166	7.60477	744	2.29724	8.58068
636	1.39422	7.64669	748	2.33953	8.58279
640	1.41677	7.68861	752	2.38182	8.58489
644	1.43933	7.73054	756	2.42411	8.587
648	1.46188	7.77246	760	2.46641	8.5891
652	1.48444	7.81438	764	2.5087	8.59121
656	1.5115	7.85667	768	2.55099	8.59331
660	1.53942	7.89904	772	2.59328	8.59542
664	1.56733	7.9414	776	2.62732	8.59143
668	1.59524	7.98377	780	2.63661	8.56913
672	1.62315	8.02613	784	2.6459	8.54683
676	1.65106	8.06849	788	2.65519	8.52454
680	1.67897	8.11086	792	2.66448	8.50224
684	1.70689	8.15322	796	2.67377	8.47994
688	1.7348	8.19559	800	2.68306	8.45765
692	1.77186	8.23325			
696	1.81154	8.26958			
700	1.85123	8.3059			
704	1.89091	8.34223			
708	1.93059	8.37855			
712	1.97027	8.41488			
716	2.00995	8.4512			
720	2.04963	8.48753			
724	2.08931	8.52385			
728	2.12899	8.56018			
732	2.17037	8.57436			
736	2.21266	8.57647			
740	2.25495	8.57857			

References

1. Eurostat. *Smarter, greener, more inclusive? Indicators to support Europe 2020 strategy.* Publications Office of the European Union, 2013.

2. EEA. *Climate Change impacts and vulnerability in 2012.* Copenhagen 2013.

3. Food and Agriculture Organization of The United Nations. *Forest and Energy, Key issues.* Rome, 2008.

4. Renewable Energy Policy Network for the 21th Century. *Renewables 2013. Global Status Report.* Paris, 2013.

5. National Geographic, http://environment.nationalgeographic.com/environment/global-warming/wind-power-profile/

6. European Photovoltaic Industry Association & Greenpeace International, *Solar Generation 6, Solar photovoltaic electricity empowering the world.* Belgium, 2011.

7. NREL, http://www.nrel.gov/ncpv/

8. Forrest S. R. The path to ubiquitous and low cost organic electronic appliances on plastic. *Nature.* **428**, 911 (2004).

9. Espinosa N., Hösel M., Angmo D. & Krebs F. Solar cells with one-day energy payback for the factores of the future. *Energy Environ. Sci.* **5**, 5117 (2012).

10. Peumans P., Yakimov A. & Forrest S. R. Small molecular weight thin-film photodetectors and solar cells. *J. Appl. Phys.* **93**, 3693 (2003).

11. Brabec C.J. *et.al.* Tracing photoinduced electron transfer process in conjugated polymer/fullerene bulk heterojunctions in real time. *Chem. Phys. Lett.* **340**, 232 (2001).

12. Dibb G. F.A. *et.al.* Influence of doping on charge carrier collection in normal and inverted geometry polymer:fullerene solar cells. *Sci. Rep.* **3**, 3335 (2013)

13. Bisquert J. & Belmonte G.G. On voltage, photovoltage, and photocurrent in bulk heterojunction organic solar cells. *J. Phys. Chem. Lett.* **2**, 1950 (2011).

14. Brabec C., Dyakonov V. & Scherf U. *Organic Photovoltaics. Materials, device physics and manufacturing technologies.* Ed. Wiley-VCH, 2009

15. Xiao X. *et.al.* A hybrid planar-mixed tetraphenyldibenzoperiflanthene/C70 photovoltaic cell. *Appl. Phys. Lett.* **102**, 073302 (2013)

16. Wang Z. *et.al.* Highly efficient organic p-i-n photovoltaic cell based on tetraphenyldibenzoperflanthene and fullerene C70. *Energy Environ. Sci.* **6**, 249 (2013)

17. You J. *et.al.* A polymer tandem solar cell with 10.6% power conversion efficiency. *Nature Comm.* **4**, 1446 (2013).

18. Li W. *et.al.* Efficient tandem and triple-junction polymer solar cells. *J. Am. Chem. Soc.* **135**, 5529 (2013).

19. Chen C. *et.al.* An efficient triple-junction polymer solar cell having a power conversion efficiency exceeding 11%. *Adv. Mater.* 2014. DOI:10.1002/adma.201402072

20. Martinez-Otero. A. *et.al.* High-performance polymer solar cells using an optically enhanced architectures. *Adv. Opt. Mater.* **1**, 37 (2013).

21. Lunt R.L. & Bulovic V. Transparent, near-infrared organic photovoltaic solar cells for window and energy scavenging applications. *App. Phys. Lett.* **98**, 113305 (2011)

22. Yu W. *et.al.* Simultaneous improvement in efficiency and transmittance of low bandgap semitransparent polymer solar cells with one-dimensional photonic crystals. *Solar Energy Mater. Solar Cells* **117**, 198 (2013)

23. Betancur R. *et.al.* Transparent polymer solar cells employing a layered light-trapping architecture. *Nature Photon.* **7**, 995 (2013).

24. Chen K. *et.al.* Strong photocurrent enhancements in highly efficient flexible organic solar cell by adopting a microcavity. *Adv. Mater.* **26**, 3349 (2014)

25. Pastorelli F. *et.al.* Enhanced light harvesting in semitransparent organic solar cells using an optical metal cavity configuration. *Adv. Ener. Mater.* 2014, DOI:10.1002/aem.201400614.

26. Ko D. *et.al.* Photonic crystal geometry for organic solar cells. *Nano Lett.* **9**, 2742 (2013)

27. Liu Y. *et.al.* Effects on nano-patterned versus simple flat active layers in upright organic photovoltaic devices. *J. Phys. D: Appl. Phys.* **46**, 024008 (2013)

28. Hsiao Y. *et.al.* Facile Transfer Method for Fabricating Light-Harvesting Systems for Polymer Solar Cells. *J. Phys. Chem. C* **115**, 11864 (2011)

29. Zu F. *et.al.* Efficient optical absorption enhancement in organic solar cells by using a 2-dimensional light trapping structure. *Appl. Phys. Lett.* **104**, 243904 (2014)

30. Adachi M. *et. al.* Broadband solar absorption enhancement via periodic nanostructuring of electrodes. Sci. Rep. **3**, 2928 (2013)

31. Mihi A. *et.al.* Imprinted electrodes for enhanced light trapping in solution processed solar cells. *Adv. Mater.* **26**, 443 (2014)

32. Nalwa K. *et. al.* On realizing higher efficiency polymer solar cells using a textured substrate platform. *Adv. Mater.* **23**, 112 (2011)

33. Na S.I. *et.al.* Efficient Polymer Solar Cells with Surface Relief Gratings Fabricated by Simple Soft Lithography. *Adv. Funct. Mater.* **18**, 3956 (2008)

34. Yu X. *et.al.* Effective light trapping enhanced near-UV/blue light absorption in inverted polymer solar cells via sol-gel textured Al-doped ZnO buffer layer. *Solar Energy Mat. Solar Cells* **121**, 28 (2014)

35. Atwater H. & Polman A. Plasmonics for improved photovoltaic devices. Nature Mat. **9**, 205 (2010)

36. Wu J. *et.al.* Surface plasmonic effects of metallic nanoparticles on the performance of polymer bulk heterojunction solar cells. *ACS Nano* **5**, 959 (2011)

37. Lu L. *et.al.* Cooperative plasmonic effect of Ag and Au nanoparticles on enhancing performance of polymer solar cells. *Nano Lett.* **13**, 59 (2013)

38. Baek S. *et.al.* Au@Ag core-shell nanocubes for efficient plasmonic light scattering effect in low bandgap organic solar cells. ACS Nano **4**, 3302 (2014)

39. Pastorelli F. *et.al.* Self-Assembled plasmonic oligomers for organic photovoltaics. *Adv. Opt. Mater.* **2**, 171 (2014)

40. Wang C. *et.al.* Optical and electrical effects of gold nanoparticles in the active layer of polymer solar cells. *J. Mater. Chem.* **22**, 1206 (2011)

41. You J. *et.al.* Surface plasmon and scattering-enhanced low-bandgap polymer solar cells by a metal grating back electrode. *Adv. Energy Mater.* **2**, 1203 (2012)

42. Gan Q., Bartoli F. & Kafafi Z. Plasmonic-enhanced organic photovoltaics: breaking the 10% efficiency barrier. *Adv. Mater.* **25**, 2385 (2013).

43. Zhou Y. *et.al.* Multifolded polymer solar cells on flexible substrates. *Appl. Phys. Lett.* **93**, 033302 (2008)

44. Niggemann M. *et.al.* Functional microprism substrate for organic solar cells. *Thin Solid Films* **511**, 628 (2006)

45. Niggemann M., Riede M., Gombert A. & Leo K. Light trapping in organic solar cells. *Phys. Stat. Sol. (a)*. **205**, 2862 (2008).

46. Cao W. *et.al.* Enhancing light harvesting in organic solar cells with pyramidal rear reflectors. *Appl. Phys. Lett.* **99**, 023306 (2011)

47. Myers J. *et.al.* A universal optical approach to enhancing efficiency of organic-based photovoltaic devices. *Energy Environ. Sci.* **5**, 6900 (2012)

48. Grandidier J. *et.al.* Light absorption enhancement in thin-film solar cells using whispering gallery modes in dielectric nanospheres. Adv. Mater. **23**, 1272 (2011)

49. Grandidier J. *et.al.* Solar cell efficiency enhancement via light trapping in printable resonant dielectric nanosphere array. *Phys. Stat. Sol. (a)*. **210**, 255 (2013)

50. Yao Y. *et.al.* Broadband light management using low-Q whispering gallery modes in spherical nanoshells. *Nature Comm.* **3**, 664 (2012)

51. Kang G. *et.al.* Broadband light-trapping enhancement in an ultrathin film a-Si absorber using whispering gallery modes and guided wave modes with dielectric surface-textured structures. *Adv. Mater.* **25**, 2617 (2013)

52. Liu Z. *et.al.* Dual broadband near-infrared perfect absorber based on hybrid plasmonic-photonic microstructure. *Opt. Express* **21**, 3021 (2013)

53. Yin J. *et.al.* Self-assembled hollow nanosphere array used as low Q whispering gallery mode resonator on thin film solar cells for light trapping. *Phys. Chem. Chem. Phys.* **15**, 16874 (2013)

54. R. Betancur, *et. al.* Optical interference for the matching of the external and internal quantum efficiencies in organic photovoltaic cells. *Sol. Energ. Mat. Sol. C.* **104**, 87-91 (2012).

55. H. Mashaal, Al. Goldstein, D. Feuerman, J. M. Gordon, First direct measurement of the spatial coherence of sunlight, Opt. Lett. 37 (2012) 3516-3518.

56. Photovoltaic Geographical Information System (EU-JRC PVGIS, Date of access: 06/02/2014) http://re.jrc.ec.europa.eu/pvgis/apps4/pvest.php

57. Ayzner A.L., Tassone C.J., Tolbert S.H. & Schwartz B.J. Reappraising the Need for Bulk Heterojunctions in Polymer-Fullerene Photovoltaics: The Role of Carrier Transport in All-Solution-Processed P3HT/PCBM Bilayer Solar Cells. *J. Phys. Chem. C.* **113**, 20050 (2009).

58. Betancur R., Maymo M., Elias X., Vuong L. T. & Martorell J. Sputtered NiO as electron blocking layer in P3HT:PCBM solar cells fabricated in ambient air. *Sol. Energy Mater. Sol. Cells.* **95**, 735 (2011).

59. Leterrier Y. *et.al.* Mechanical integrity of transparent conductive oxide films for flexible polymer-based displays. *Thin Solid Films.* **460**, 156 (2004).

60. Kikuchi N. *et.al.* Electrical and mechanical properties of SnO2:Nb films for touch screens. *Vacuum.* **66**, 365 (2002).

61. Nakada T. *et.al.* Novel device structure for Cu(In,Ga)Se2 thin film solar cells using transparent conducting oxide back and front contacts. *Sol. Energy.* **77**, 739 (2004).

62. Tiwari A.N. *et.al.* CdTe solar cell in a novel configuration. *Prog. Photovoltaics.* **12**, 33 (2004).

63. May C. & Strümpel J. ITO coating by reactive magnetron sputtering-comparison of properites and MF processing. *Thin Solid Films.* **351**, 48 (1999).

64. Kurdesay F. *et.al.* Comparative Study of ITO layers deposited by DC and RF magnetron sputtering at room temperature. *J. Non-Cryst. Solids.* **352**, 1466 (2006).

65. Keum M.J. & Han J. G. Preparation of ITO thin film by using DC magnetron Sputtering. *J. Korean Phys. Soc.* **53**, 1580 (2008).

66. Tuna O. *et.al.* High quality ITO thin films grown by DC and RF sputtering without oxygen. *J.Phys. D: Appl. Phys.* **43**, 055402 (2010).

67. Wei L. & Shuying C. Photoelectric properties of ITO thin films deposited by DC magnetron sputtering. *J. Semicond.* **32**, 1 (2011).

68. Niggemann M. *et.al.* Functional microprism substrate for organic solar cells. *Thin Solid Films* **451-452**, 628 (2006).

69. Niggemann M., Riede M., Gombert A. & Leo K. Light trapping in organic solar cells. *Phis. Stat. Sol. (a)*. **205**, 2862 (2008).

70. Nalwa K., Park. J, Ho K. & Chaudhary S. On Realizing Higher Efficiency Polymer Solar Cells Using a Textured Substrate Platform. *Adv. Mater.* **23**, 112 (2011).

71. Lopez M. A., Sanchez J. C. & Estrada M. Characterization of PEDOT:PSS dilutions for inkjet printing applied to OLED fabrication.

Devices, circuits and Systems, 2008. ICCDCS. 7th International Caribean Conference on IEEE. 2008.

72. Guo X. *et.al.* High efficiency polymer solar cells based on poly(3-hexyiltiophene)/Indene-C60 Bisadduct with solvent additive. *Energy Environ. Sci.* **5**, 7943 (2012).

73. Park B., Ho Y. & Kim M. Surfactan additives for improved photovoltaic effect of polymer solar cells. *J. Mater. Chem.* **20,** 10868 (2010).

74. Huh Y. & Park B. Interface-engineering additive of poly(oxyethylene tridecyl ether) for low-band gap polymer PCDTBT:PCBM70 bulk-heterojunction layers. *Opt. Express.* **21**, A146 (2013).

75. Chang Y. *et.al.* Polymer solar cell by blade coating. *Org. Electron.* **10**, 741 (2009.)

76. Zhang B., Chae H. & Cho S. Sreen-Printed Polymer:Fullerene Bulk-Heterojunction Solar Cells. *Jpn. J. Appl. Phys.* **48**, 020208 (2009).

77. Dang M.T. *et. al.* Polymeric solar cells based on P3HT:PCBM: Role of the casting solvent. *Sol. Energ. Mat. Sol. C.* **95**, 3408 (2011).

78. Na S. I. *et.al.* Efficient Polymer Solar Cells with surface Relief Gratings Fabricated by Simple Soft Lithography. *Adv. Funct. Mater.* **18**, 3956 (2008).

79. Zhou Y. *et.al.* Multifolded polymer solar cells on flexible substrates. *Appl. Phys. Lett.* **93**, 033302 (2008).

80. Xiao X. *et.al.* A hybrid planar-mixed tetraphenyldibenzoperiflanthene/C70 photovoltaic cell. *Appl. Phys. Lett.* **102**, 073302 (2013).

81. Fujishima D. *et.al.* Organic thin-film solar cell employing a novel electron-donor material. *Sol. Energ. Mat. Sol. C.* **93**, 1029 (2009).

82. Wang Z. *et.al.* Highly efficient organic p-i-n photovoltaic cell based on tetraphenyldibenzoperiflanthene and fullerene C70. *Energy Environ. Sci.* **6**, 249 (2013).

83. Zhou Y. *et.al.* Controlled growth of dibenzotetraphelperiflanthene thin films by varying substrate temperature for photovoltaic applications. *Sol. Energ. Mat. Sol. C.* **95**, 2861 (2011).